University of California
Santa Barbara

Valence modulates the phase behavior and viscoelasticity of transient DNA nanostar networks

A dissertation submitted in partial satisfaction
of the requirements for the degree

Doctor of Philosophy
in
Physics

by

Nathaniel C. Conrad

Committee in charge:

Professor Deborah K. Fygenson, Co-chair
Professor Omar A. Saleh, Co-chair
Professor M. Cristina Marchetti

June 2023

The Dissertation of Nathaniel C. Conrad is approved.

Professor M. Cristina Marchetti

Professor Omar A. Saleh, Committee Co-Chair

Professor Deborah K. Fygenson, Committee Co-Chair

June 2023

Valence modulates the phase behavior and viscoelasticity of transient DNA nanostar networks

by

Nathaniel C. Conrad

Abstract

Valence modulates the phase behavior and viscoelasticity of transient DNA nanostar networks

by

Nathaniel C. Conrad

A gel is a soft material that is made when a three-dimensional polymer or colloidal network is hydrated in water or suspended in some other solvent. Gels can be found in nature (e.g., inside cells, lining the stomach, etc.) and are synthesized for many different consumer and medical applications. Their versatility and utility stem from a large array of accessible phase behaviors (e.g., sol-gel, liquid-liquid, etc.) and viscoelastic properties, both of which can be controlled at the polymer/colloidal level. Recent theoretical works predict that the phase behavior and viscoelasticity of a colloidal/molecular gel network is strongly modulated by the connectivity of the colloid in solution (e.g., valence). However, in practice, engineering particles of well-defined valence is difficult, making experimental insight hard to come by. Here, I take advantage of DNA programmability to self-assemble, via base-pairing, transiently bonded DNA particles of designed valence, called DNA nanostars (NSs). I measure NS phase diagrams and network viscoelasticity as a function of NS valence, z. My measurements show that increasing z results in a larger coexistence regime for phase separation and a stiffer, more brittle NS network. In particular, I find that: (i) the valence effect on phase behavior is largely in line with theoretical expectations and (ii) NS viscoelasticity is controlled by an interplay between entropic elasticity of network chains and NS valence imposing junction constraints (e.g., approaching an isostatic threshold). I also make a NS with two types of bonds on it, where one bond is short-lived and the other is much longer-lived. I find that such NSs

make networks with reproducible power-law stress-relaxation between the two bond lifetimes and the power-law exponent depends on the valence of the stronger-bond. I further show that the power-law exponent during stress-relaxation is explained by a model that considers how the strong-bonded network relaxes in an effective medium with a viscosity defined by the weak-bonds. Overall, the work here provides insight into how valence modulates the phase behavior and viscoelasticity of transient gel networks.

Curriculum Vitæ

Nathaniel C. Conrad

Education

2023 (Expected)	Ph.D. in Physics, University of California, Santa Barbara.
2019	M.A. in Physics, University of California, Santa Barbara.
2016	B.Sc. in Physics, University of California, Santa Barbara.
2016	B.Sc. in Mathematical Sciences, University of California, Santa Barbara.

Fellowships and Awards

2020-21	UCSB Graduate Research Mentorship Program Fellowship
2019	UCSB Worster Summer Research Mentorship Program Fellowship
2016	UCSB Physics Undergraduate Distinction in the Major
2016	UCSB Physics Undergraduate Highest Academic Honors
2014	UCSB MRL RISE Summer Fellowship

Publications

1) N. Conrad, G. Chang, D.K. Fygenson, and O.A. Saleh, "Emulsion imaging of a DNA nanostar condensate phase diagram reveals valence and electrostatic effects", *J. Chem. Phys.* 157:234203, (2022), `https://doi.org/10.1063/5.0130808`

2) N. Conrad, T. Kennedy, D.K. Fygenson, and O.A. Saleh, "Increasing valence pushes DNA nanostar networks to the isostatic point", *PNAS* 116:7238–7243, (2019), `https://doi.org/10.1073/pnas.1819683116`

3) B.J. Jeon, D.T. Nguyen, G.R. Abraham, N. Conrad, D.K. Fygenson, and O.A. Saleh, "Salt-dependent properties of coacervate-like, self-assembled DNA liquid", *Soft Matter* 14:7009–7015, (2018), `https://doi.org/10.1039/c8sm01085d`

Manuscripts in preparation

1) N. Conrad, O.A. Saleh, and D.K. Fygenson "Power-law rheology in heterogeneously bonded DNA nanostar networks"

2) N. Conrad, O.A. Saleh, and D.K. Fygenson "Rheology of heterogeneously bonded DNA nanostar equilibrium gels"

Professional Appointments

2016-18, 2020-23	Graduate Student researcher, Department of Physics, University of California, Santa Barbara

2018-20	Teaching Assistant, Department of Physics, University of California, Santa Barbara
2014-16	Undergraduate researcher, Department of Physics, University of California, Santa Barbara

Acknowledgements

This dissertation research was simply not possible without the help of others, either directly or indirectly.

First and foremost, I thank my advisors and principal investigators, Deborah and Omar. My (very long) time training under you two is something I will forever cherish. You two have expertly guided me to become the scientist I am now and given me the confidence I needed to start my journey as an independent scientist. I am extremely grateful for you two getting me to this point in my career. I hope we continue staying in touch in the future.

I also thank my fiancé, Aileen Cruz. Your boundless love and support was the anchor I needed while completing this thesis. I knew I could rely on you to keep me grounded and in touch with reality. I love you!

Lastly, there are many other people in the soft matter physics community that were integral to my research and time here at UCSB. To name a few:

1. Past and current Fygenson and Saleh lab members - Amber Cai, Grace Chang, Tynan Kennedy, Alex Bevier, Gabi Abraham, Anna Nguyen, Frank Truong, Sam Wilken, Ian Morgan, and Sarah Innes-Gold - it was always a pleasure talking about science with you all;

2. Two past lab members, not listed above, that I would like to especially thank are Lourdes Velazquez and Chang-Young Park for training me in the lab when I was an undergraduate (and when I had very long, grungy hair);

3. Matthew Helgeson and Rachel Behrens, both here at UCSB, for their help with the rheometers used in my experiments;

4. Crisina Marchetti for keeping me on track and helpful career advice during my thesis committee meetings;

5. Emanuelle Locatelli and Lorenzo Rovigatti for providing simulated NS data and helpful discussions about how to model NS phase separation;

6. Chase Broedersz and Fred MacKintosh for insightful theoretical discussions regarding how to model NS network viscoelasticity.

Contents

Chapter 1

Introduction

When many chemically or physically interacting particles (polymers or colloids) are suspended in a liquid, they will often associate to form a three-dimensional network. Depending on particle concentration, the networks will either span the entire solution volume (e.g., form a gel) or make phase separated condensates/clusters. The mechanical and dynamic properties of the gel or condensate result from the underlying particle properties and interactions [1–3]. Changing the particle properties and interactions thus allow for a wide array of both phase behaviors and gel viscoelasticities that are attractive for modeling biologically relevant systems [4, 5] and for applications in industry [6–8] and medicine [9–12].

A property of a network that strongly modulates its resulting phase behavior [2,13,14] and bulk mechanical properties [15–18] is the connectivity of the network or the average number of network filaments emanating from a shared junction. Accordingly, the network connectivity is largely controlled by the number of connections made between colloidal particles (in a colloidal network) or the number of chains meeting at a junction (in a polymer network), which we define here as the particle/junction valence, z. In practice, however, z is hard to control [19–24], making it difficult to gain insights capable of refining theory and simulation. For instance, in most polymer networks, z is limited to between 2 and 4 [21–24]. This is because z in polymer networks is determined by entanglements

between polymers ($z = 4$) or the architecture of cross-links bridging polymers (short, linear cross-links are typical [25, 26] and lead to $z = 3$), and any loops that form will reduce z. The valence can change in polymer networks through changing the polymer and cross-linker concentration, but both the polymers and cross-links must be monodisperse to achieve precise control of valence between 2 and 4 [21]. In colloidal networks, the connectivity of the network approaches the designed valence of the colloid, which can be anywhere $2 < z \leq 12$. Some control has been demonstrated at the particle level using "patchy" colloids (e.g., distinct "sticky patches" decorated on colloid surface) [2, 19, 20], although the distribution of "patchy" colloid valence is still broad [19, 20].[1] Thus, there is a need for model systems with precise valence control in order to better understand how z affects the bulk solution phase behavior and viscoelasticity.

Here, we take advantage of the programmability of DNA base-pairing to reproducibly make solutions of cross-linking DNA particles with well-defined valence and binding interactions, called DNA nanostars (NSs) [13, 27]. In particular, a z-armed NS consists of z freely-hinged double stranded DNA (dsDNA) arms emanating from a common junction. Each arm terminates at its distal end in a short palindromic/self-complementary ssDNA sequence (e.g., a sticky-end). The palindromic sticky-end allows NSs to transiently bind to each other and the flexibility of the NS arm at the NS junction permits easy arm rearrangement in the network state when the bond dissociates and reforms. The combination of transient, flexible bonds and limited NS valence ($2 < z < 12$) gives the resulting NS network enough entropy to stabilize a disordered-liquid state over a crystalline one [2, 28, 29]. This property ensures NS networks are not kinetically arrested, making for hysteresis-free structure formation. NSs are thus model particles to explore the effects of network valence on phase behavior and viscoelasticity [13, 27, 29–37].

This brings us to the layout of the thesis. In chapter 2, an emulsion-based imag-

[1] Colloids that do not have sticky patches have their valence controlled by their surface roughness [18].

ing technique is established to measure the temperature-concentration phase diagram of macromolecules undergoing liquid-liquid phase separation (LLPS). The imaging technique is then used to investigate the effect of NS valence and added salt on the resulting phase diagram. In chapter 3, the viscoelasticity of dense NS solutions are probed using oscillatory shear rheology in a parallel plate setup. The rheology data reveals that the effect of NS valence on solution viscoelasticity is consistent with approaching an isostatic threshold between $z = 5$ and $z = 6$. In chapter 4, a valence-six NS is designed to have two types of bonds, a short-lived and a long-lived one. We find such "heterotypic" NSs make networks with reproducible power-law stress-relaxation and with the power-law controlled by the valence of the longer-lived bonds on the NS. We also develop a model that derives an expression for the power-law exponent and show it is both consistent with our observations and observations in simulated systems. In chapter 5, we measure the viscoelastic spectra of many different types of heterotypic NSs and discuss the viscoelastic behavior over all frequencies, not just over the frequencies pertaining to power-law stress-relaxation.

Funding

1. The project in Chapter 2 was supported by the National Science Foundation, NSF Award No. CMMI 1935400.

2. The project in Chapter 3 was supported by the National Science Foundation, NSF Award No. CMMI 1363135.

3. The project in Chapter 4 and 5 was supported by the National Science Foundation, NSF Award No. CMMI 1935400. The research reported also made use of shared facilities of the UCSB MRSEC (NSF DMR 1720256).

Chapter 2

Emulsion Imaging of a DNA condensate phase diagram reveals valence and electrostatic effect

2.1 Preamble

The content of chapter 2 and appendix A is the result of a collaboration with Grace Chang, Deborah K. Fygenson, and Omar A. Saleh. This work is reprinted with permission from J. Chem. Phys. 157, 234203 (2022), Copyright 2022 American Chemical Society.

2.2 Introduction

LLPS of aqueous solutions of macromolecules involves the equilibrium segregation of a fluid into regions dense in macromolecule, and regions dilute in macromolecule. The process has long been studied in mixtures of oppositely charged polymers, where it is termed complex coacervation [38]. Investigating the variables which control macromolecular LLPS is critical to further both our understanding of its role in biological systems [39–44] and development of tunable materials for pharmaceutical or food-science

applications [45–49].

The LLPS process is generally controlled by temperature, the concentration of the macromolecule and of other solutes (e.g. salt), and the nature of the interactions in the system, including with the solvent [50, 51]. Fundamental to the characterization of LLPS, and its sensitivity to such parameters, is the equilibrium phase diagram, in which binodal lines separate the conditions in which an equilibrated solution will form a single, homogeneous fluid, from those in which the solution will spontaneously separate into coexisting dense and dilute phases. Experimental measurements of binodal lines are made challenging by the need to handle and assay each phase. The most common method involves separating the dilute and dense phases by centrifugation [13, 50, 51], which typically requires large volumes of solution ($\gtrsim$ 100 μL) that may be inaccessible and/or prohibitively expensive [52] for some systems. Further, dense macromolecular phases are typically highly viscous, and prone to adhere to solid surfaces, making handling difficult.

The difficulties in working with phase-separating systems can be ameliorated by encapsulating them within the aqueous droplets of water-in-oil emulsions. Indeed, as demonstrated in prior works [53–55], the emulsion approach has advantages, including (i) not involving centrifugation or direct handling of the phase-separated solution, (ii) requiring small amounts of the solution of interest, and (iii) being agnostic to the macromolecule under investigation. Here, we exploit these advantages to develop an emulsion-based fluorescent imaging method for measuring the binodal lines of macromolecular LLPS systems in the temperature-concentration plane. We confine the system of interest in micron-scale, water-in-oil emulsion droplets, and then image the droplets using a temperature-controlled, wide-field fluorescence microscope equipped with a low numerical aperture, low magnification lens. The images capture the full fluorescent profile of an emulsion droplet, which we can fit to the expected profile, resulting in precise

quantification of the volume fraction of the dense phase. We then use the measured concentration-dependence of the volume fraction, and the lever rule of binary, equilibrium phase separation [50, 56], to estimate the binodal concentrations of the respective phases. Independently, we measure the melting temperature by visualizing the appearance of condensate within the emulsion droplet while scanning temperature. Together, the measured melting temperatures and binodal concentrations allow us to construct the full phase diagram.

We use this method to investigate the phase behavior of multi-valent DNA nanostars (NSs) that exhibit LLPS [13, 30]. In particular, we use emulsion imaging to explore how NS phase diagrams change as z increases from 3 to 6, and we test how $z = 3$ and 4 NS phase diagrams are affected by added monovalent salt. We interpret our results with respect to structures and physical mechanisms that are expected to affect NS density, and also carry out a quantitative comparison of our data to theoretical models of NS phase separation [36], notably validating valence-sensitive predictions for the critical temperature.

Generally, the work presented in this chapter presents a method for quantifying LLPS phase diagrams that avoids issues in prior approaches, and is thus of potentially broad utility. Further, our application of the method to the NS system gives insight into the principles guiding phase separation of multi-valent particles.

2.3 Methods

2.3.1 Preparation of NSs and emulsions

A full description of all methods can be found in the Appendices. Briefly, we prepared z-armed NSs by mixing together equimolar amounts of z single-stranded DNA oligomers

designed to self-assemble into a NS upon annealing (Fig. 2.1A; DNA sequences given in Appendix,, Table A.1). A fraction of the oligos were tagged with a fluorescent molecule for later visualization (see Appendix A.1). We also separately annealed a non-interacting, fluorescently-tagged DNA hairpin and added it to the NS solution at 5 μM (Fig. 2.1A).

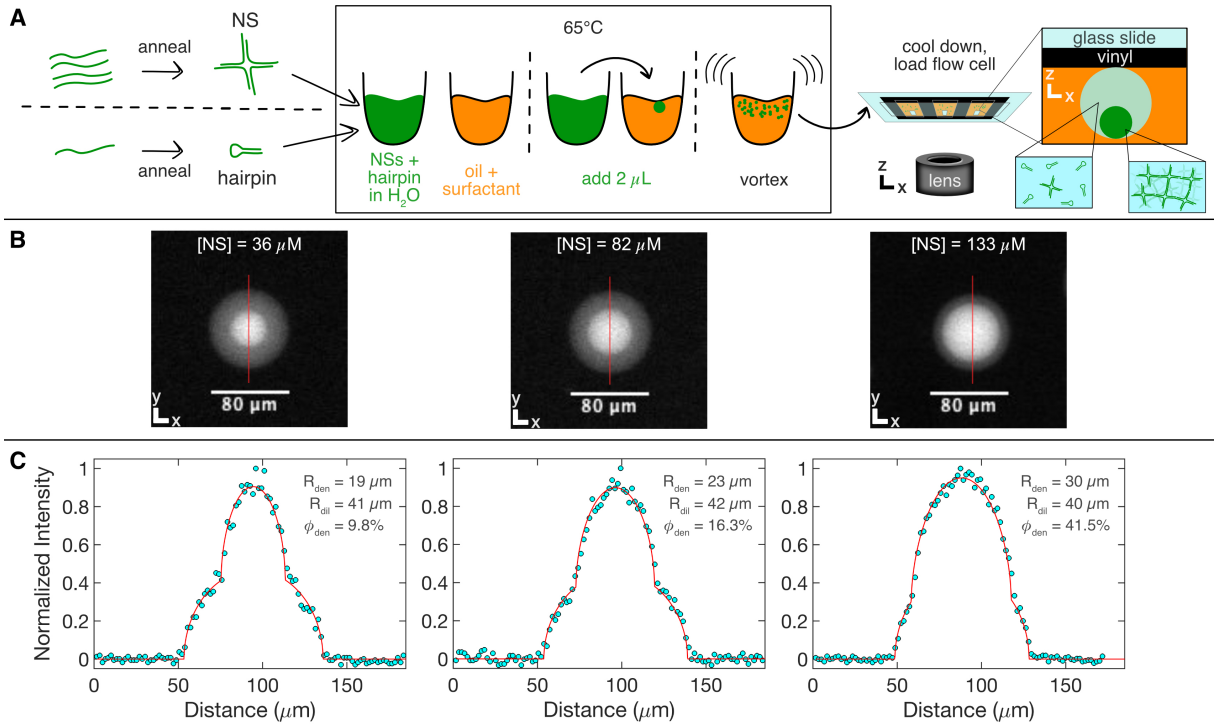

Figure 2.1: **(A)** Schematic depicting the preparation of samples for emulsion-imaging of NS phase diagrams; see also Appendix A.1. NSs and non-interacting hairpins are annealed separately and mixed together. Then, 2-3 μL of aqueous NS+hairpin solution is added to ≈ 40 μL of an oil/surfactant mixture and briefly vortexed to create water-in-oil emulsion droplets. The sample is loaded into a flow cell, and cooled, allowing the NSs to phase separate, forming a dense, spherical DNA liquid drop within the spherical emulsion droplets. **(B)** Representative images of emulsion droplets containing phase-separated 4 arm NS solutions (150 mM NaCl, $T = 33.1 \pm 0.5°C$), at different total NS concentrations, [NS], as labeled. The red lines depict the positions of the 1-d intensity profiles shown in panel C. Each image shown was cropped from a larger field of view; in practice, we typically analyzed 5-10 droplets per field of view (Appendix A.2; see also Appendix, Fig. A.2). **(C)** Profile of image intensity along the pixels indicated in panel B (cyan), along with the best-fit line (red) for the double-sphere function (Appendix,, Section A.1). Labels indicate the best-fit radii, which have a fit uncertainty of ≈ 0.01-0.02 μm.

The hairpin was added to brighten the dilute phase so that it could be visualized alongside the dense phase, which is typically ≈100-1000x more concentrated. NS phase separation was unaffected by moderate amounts of hairpin (see Appendix, Fig. A.3). The concentrations of both NS and hairpin were measured using UV absorbance.

We made water-in-oil emulsions by adding 2-3 μL of the NS+hairpin solution to 40 μL of an oil and surfactant mixture, which was kept warm ($T \approx 65°$C) to prevent NS phase separation, then vortexing for 2-3 seconds (see Appendix A.1). The resulting emulsion droplets had diameters of $\approx 25 - 120$ μm, as appropriate for our microscopic approach.

We placed emulsified NS solutions, each prepared with a different concentration of nanostars, [NS], into separate channels of a custom-built multi-channel flow cell (see Appendix A.2). The flow cell was then placed on a temperature-controlled microscopic stage, and allowed to equilibrate. NS phase separation occurred within the emulsion droplets as they cooled (Fig. 2.1B). The dense NS phase equilibrated into a sphere inside the aqueous emulsion droplet, as expected given its liquid-like nature [27] and consistent with previous experiments on NSs undergoing LLPS [30]. The water droplet, being less dense than the oil, rose (creamed) to the top of the flow cell, while the NS condensate, being heavier than water [30], settled to the bottom of its water droplet container (Fig. 2.1A).

2.3.2 Measurement of condensate melting temperature

To estimate the melting temperature, T_m, of the dense phase at a given [NS], we recorded a video of emulsion droplets while slowly raising and lowering the temperature of the stage (typically 0.5°C/min; see Appendix, Fig. A.6). Because it was difficult to identify a single frame at which the condensate appeared or disappeared, we estimated T_m as the average T over the range of frames – from the first/last frame in which a phase

boundary was clearly present to the last/first frame in which it was clearly absent – and used the range of T to estimate the uncertainty in T_m. This procedure was also used in the few cases in which there was significant hysteresis (typically of 2-6°C).

2.3.3 Measurement of condensate volume fraction

At a given T and [NS], we measured the volume fraction of the dense phase, ϕ_{den}, by imaging the emulsion droplets using a low numerical aperture (0.1 or 0.13 NA), low magnification (4x) objective. Typical images and intensity profiles are shown in Fig. 2.1 and Appendix, Fig. A.2. The use of low NA optics imparted on the imaging system a large depth-of-field, so a single image (properly focused) captured all fluorescent intensity within a water droplet. The act of imaging thus projected, into the 2-d image, a 3-d fluorescent "double-sphere" corresponding to the smaller, bright sphere of dense NS liquid, and the larger, dimmer dilute NS solution contained in the spherical emulsion. Correspondingly, we found that the emulsion droplets' 2-d intensity profiles, $I(x, y)$, were consistently well fit ($R^2 \geq 0.99$) by a geometric function for the two-dimensional projection of two spheres, of differing sizes and intensities (Fig. 2.1C; also see Appendix,, Section A.2 and Fig. A.1). The fitting parameters were the radii R of the emulsion droplet and NS condensate; their central positions in (x, y); and the fluorescence intensity of each phase. We then found the volume fraction through $\phi_{\text{den}} = (R_{\text{den}}/R_{\text{dil}})^3$, where the subscripts denote the dense and dilute phases.

The use of low-NA optics degrades the lateral resolution of the microscope, increasing diffractive blur in the image; this blur is not described by the double-sphere fitting function. However, we found that blurring only caused very slight deviations between the data and the fit (see Appendix, Fig. A.1B), likely because the diffraction limit of the system, ≈ 3 μm, is much smaller than the size of the condensate and emulsion droplet

(> 10 μm). This indicates the fit values are robust against such blurring.

To test the sensitivity of the fitting procedure to the microscope focus, we acquired and analyzed images at a variety of focal positions. We found the best-fit radii were insensitive to focal position over a broad range (120-150 μm; see Appendix, Fig. A.4), meaning that precise focus was not needed. Further, while our emulsions contained a range of droplet sizes that accordingly were located at different heights in the flow cell, the insensitivity to focal position meant that we were able to accurately analyze emulsion droplets of different diameters from a single image. Particularly, the fitted radii from a single image of multiple emulsion droplets that ranged from $\approx$ 25 μm to 120 μm in diameter, each containing the same NS concentration, all resulted in the same value of ϕ_{den} (Appendix, Fig. A.4).

2.4 Results

2.4.1 The lever rule and measuring binodal concentrations

We measured ϕ_{den} vs. [NS] across a range of temperatures, $10°\text{C} \leq T \leq 43°\text{C}$, for a variety of NS systems with different z and/or in different concentrations of monovalent salt, [NaCl] (Fig. 2.2, see also Appendix, Fig. A.5). In all cases, we observed that ϕ_{den} scales linearly with [NS]. This is characteristic of a binary system undergoing equilibrium phase separation [50, 56], as expressed by the lever rule:

$$\phi_{den} = \frac{[\text{NS}] - [\text{NS}]_{\text{dil}}}{[\text{NS}]_{\text{den}} - [\text{NS}]_{\text{dil}}} \tag{2.1}$$

In Eq. 2.1, [NS] is a known quantity, while $[\text{NS}]_{\text{den}}$ and $[\text{NS}]_{\text{dil}}$ correspond to the initially-unknown binodal concentrations of the two phases. Thus, Eq. 2.1 indicates $[\text{NS}]_{\text{den/dil}}$ can be measured by finding the x-intercept and slope of the ϕ_{den} vs. [NS] line, with the

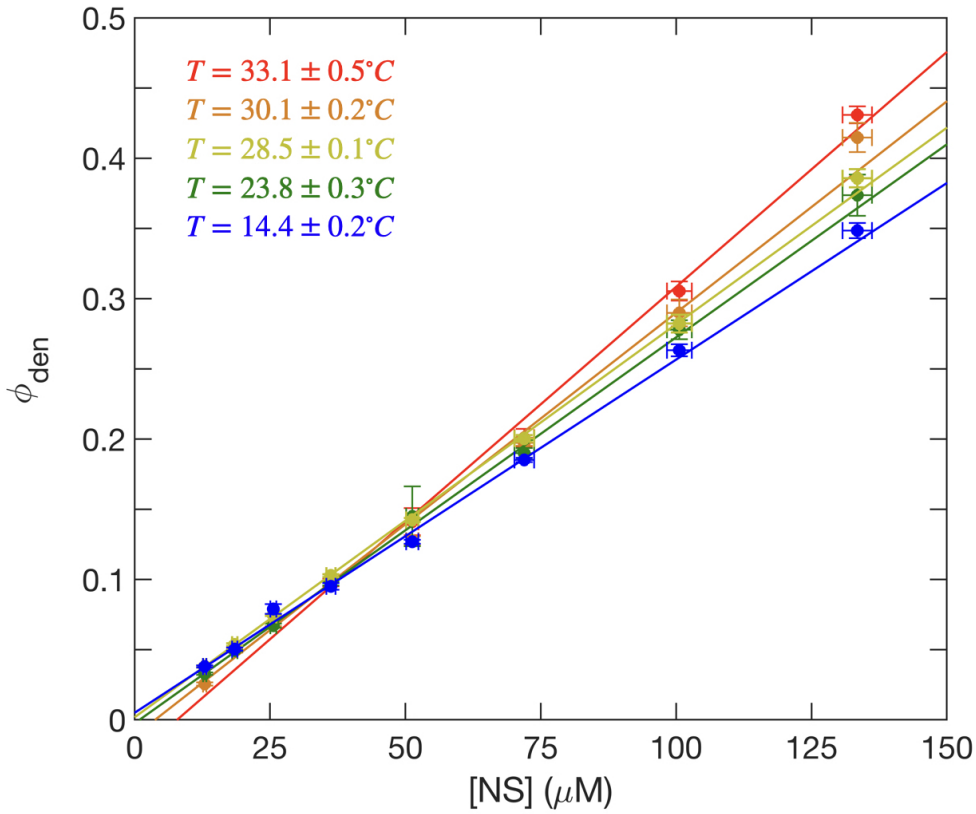

Figure 2.2: The volume fraction of the dense phase, ϕ_{den}, of $z = 4$ NSs at 150 mM NaCl as a function of the total NS concentration, [NS], at various temperatures. The solid line denotes the (weighted) least squares fit of the lever rule (Eq. 2.1) to each data set. Lever rule plots for other salts and arm numbers are shown in the Appendix, (Fig. A.5). Each plotted point corresponds to, typically, 10-30 measured droplets, with some points having as few as 2 droplets, and some as many as 50. For each temperature, at least 100 droplets are measured across all concentrations. Vertical error bars correspond to the standard error of the mean (SEM) of the fits to various droplets, while horizontal error bars correspond to the SEM of UV absorbance measurements of the NS stock concentration.

x-intercept giving $[\text{NS}]_{\text{dil}}$ and the slope being equal to the inverse of the difference in binodal concentrations, $[\text{NS}]_{\text{den}} - [\text{NS}]_{\text{dil}}$.

Under all conditions, the x-intercept and slope changed most at temperatures within $\approx 10°\text{C}$ of the onset of phase separation, with further decreases in T leading to no further significant changes. It is possible that, at low temperatures, the system did not fully reach equilibrium due to the NS bond relaxation time growing exponentially as the solution is

cooled, which could potentially freeze the dense NS droplet at a certain size, and cause the constant behavior of slope and intercept at low temperatures. However, previous rheology [27] and light scattering [13, 29, 34, 57] experiments show NS networks achieve equilibrium states down to 10°C using cooling rates similar to the ones performed here ($\approx$ 0.1 - 1°C/min), suggesting that this behavior is indicative of the equilibrium state of the system.

2.4.2 NS phase diagrams

We combined the binodal concentrations measured from lever rule analysis with the melting-temperature measurements to generate temperature-concentration coexistence curves for NSs as a function of arm number, z, and, for $z = 3, 4$ NSs, at various monovalent salt (NaCl) concentrations (Fig. 2.3). Qualitatively, the diagrams all have a similar shape, demonstrating an upper critical solution temperature, T_c, below which a coexistence regime appears. For $(T_c - T) \lesssim 10$°C, the coexistence regime increases in width as T decreases, but at lower T the width stabilizes. These features qualitatively match those seen in previous estimates of NS phase diagrams [13].

We sought to quantify T_c so as to facilitate comparison with predictive models. We observed the maximal melting temperature typically occurred at a NS concentration roughly midway between the binodals (Fig. 2.3). For each NS condition, we took this greatest T_m to be an estimate of T_c, and investigated its variation with other experimental parameters. At constant salt, T_c increased by nearly 10°C from $z = 3$ to $z = 4$, then continued to increase between $z = 4$ and 6, but by only ~ 2°C (Fig. 2.4). For 4-arm NSs, and for [NaCl] from 50 mM to 300 mM, T_c increases with salt roughly as $T_c \sim \log$[NaCl] (Fig. 2.5).

The dense-phase binodal concentration, $[\mathrm{NS}]_{\mathrm{den}}$, generally increases with z and [NaCl].

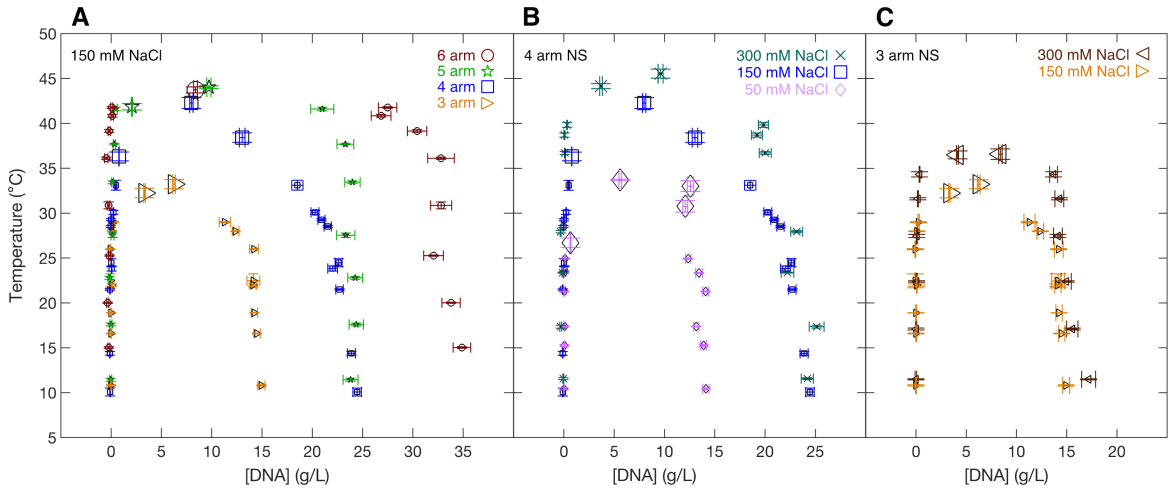

Figure 2.3: Temperature-concentration phase diagram of **(A)** NSs of various z, all at [NaCl] = 150 mM, and **(B)** 4-arm and **(C)** 3-arm NS at different [NaCl]. Smaller symbols indicate data found from lever-rule fits (as in Fig. 2.2), while larger symbols indicate data found from direct melting temperature estimate.

However, there are a few expections where certain pairs of conditions had very similar low-T values of $[\mathrm{NS}]_{\mathrm{den}}$: (i) $z = 4$ vs. $z = 5$ at 150 mM NaCl (Fig. 2.3A); (ii) $z = 4$ at 150 mM vs. 300 mM NaCl (Fig. 2.3B); and (iii) $z = 3$ at 150 mM vs. 300 mM NaCl (Fig. 2.3C). These are further discussed below.

We found the dilute-phase binodal concentration, $[\mathrm{NS}]_{\mathrm{dil}}$, at lower temperatures to have extremely low values of typically ≤ 0.1 g/L (this is not visible in Fig. 2.3, but can be seen on a semi-log plot; see Appendix, Fig. A.7). Away from T_c, the binodal roughly traces a $T_m \sim \log([\mathrm{NS}]_{\mathrm{dil}})$ dependence, as also seen in certain models [58]. However, the very low concentration of the dilute NS phase, along with experimental uncertainties (discussed below), means this is not perfectly resolved. Indeed, at the lowest T, these factors sometimes caused a negative x-intercept for the line fitted to lever-rule data (as in Fig. 2.2), corresponding to a physically-impossible negative value of $[\mathrm{NS}]_{\mathrm{dil}}$.

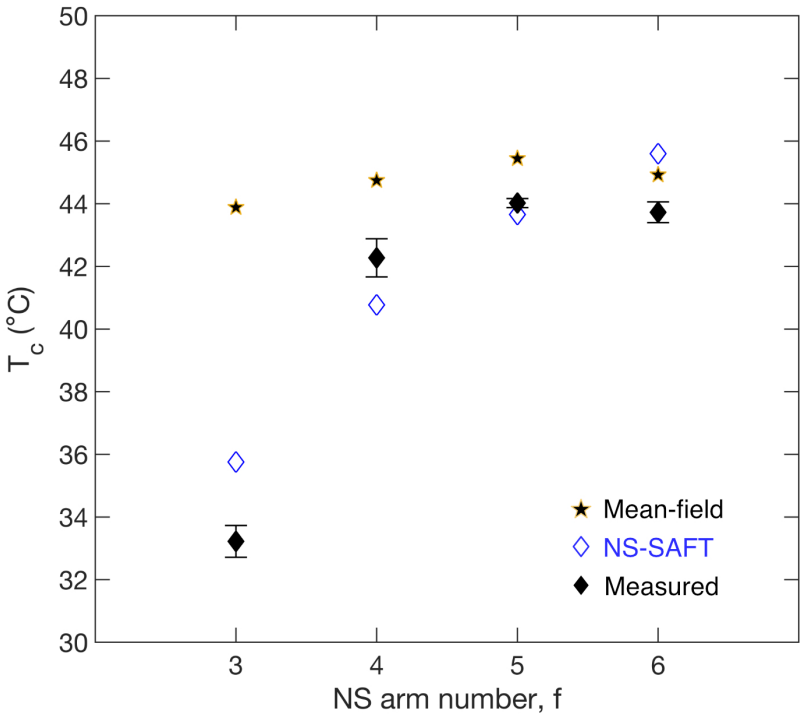

Figure 2.4: Critical temperature, T_c, versus NS valence, z, at [NaCl] = 150 mM, as estimated from the experiments (filled black diamonds), the mean-field model (stars), and the NS-SAFT model (empty blue diamonds).

2.4.3 Modeling of phase behavior

We compared the experimental results for T_c to predictions to gain insight into NS LLPS behavior, first through a simple mean-field model. In this picture, we ignored the geometry of the NS, and compared our measurements of T_c to the predicted melting temperatures, T_m, of a solution of *unconnected* (free) oligomers at concentrations corresponding to those of the NS sticky ends, [oligomer] = $f \cdot$ [NS]). We estimated T_m using the DNA thermodynamics approach of Santa Lucia [59], based on the specific sequence, salt, and oligomer concentration utilized. Particularly, we used the oligomer sequence 5'-ACGATCG-3', which consists of the sticky-end sequence plus a single unpaired base that is also present in the NS structure. We accounted for the effect of the free base using

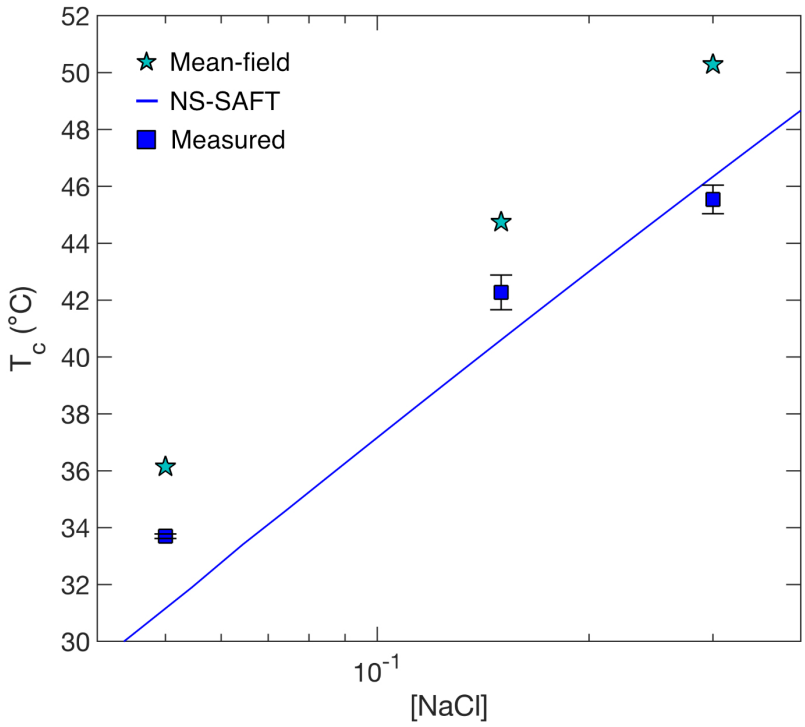

Figure 2.5: Semi-log plot of critical temperature, T_c, versus [NaCl] for $z = 4$ NSs, as estimated from the experiments (blue squares), the mean-field model (stars), and the NS-SAFT model (lines).

the standard SantaLucia dangle correction [59] and added an empirical "tail" correction to capture the effect of the flanking NS arms on the sticky-end strength [36, 60]. The results of this mean-field calculation are plotted in Figs. 2.4 and 2.5, which shows the model is in the vicinity of the experimental values, and captures the trend with salt, but fails to account for the large measured variation of T_c with z.

This failure suggests the z-fold connectivity of sticky ends that is enforced by the NS structure plays an important role in determining the LLPS behavior. To capture this, we followed the work of Rovigatti and collaborators [36, 58, 61], who developed a method for predicting NS phase diagrams using the Statistical Associating Fluid Theory (SAFT) created by Wertheim [62–64] and further developed by Chapman *et. al.* [65–67]. In SAFT, a first-order perturbation calculation is used to construct the free energy of a

solution of particles from the free energy of an ideal fluid, with corrections for repulsive (excluded-volume) interactions, and for z-valent inter-particle binding. Rovigatti *et al.* extended this model to NSs by estimating the excluded volume parameter (*i.e.*, the 2nd virial coefficient), B_2, from coarse-grained molecular dynamics simulations of NSs [58] and by using a temperature-dependent bonding term based on the Santa Lucia model with a tail correction, as noted above [36,61]. The resulting equations can then be solved numerically to directly estimate T_c through the stability constraint that, at the critical point, both the first and second derivatives of the pressure with respect to density are zero.

We used the NS-SAFT approach (Appendix A.5), adjusted for the specific sticky-end sequence used here, and, for 3- and 4-armed NSs, using B_2 values from Ref. [58]. This prior work did not investigate B_2 values for 5- or 6-armed NSs; since the underlying simulations are quite involved, we opted to estimate their B_2 values by extrapolation from the numerically simulated values for 4 arm NSs. In particular, we posited that the excluded volume should scale with the number of NS arms, i.e. $B_2 \sim z$. Indeed, from the simulated B_2 for 3 and 4 arm NSs [58], we found $B_2(4\text{ arm})/B_2(3\text{ arm}) \approx 1.43\text{-}1.48$, which is not too different from 4/3. We accordingly estimated the second virial coefficients for 5 and 6 arm NSs from $B_2(5\text{ arm}) = (5/4)\cdot B_2(4\text{ arm})$ and $B_2(6\text{ arm}) = (6/4)\cdot B_2(4\text{ arm})$.

Using these B_2 values, we found the NS-SAFT model provides a good description of the variation of T_c with both salt and z (Figs. 2.4 and 2.5). Notably, the model is quite close to experiment at at large z, and (unlike the mean-field picture) captures the large decrease in T_c as z decreases to 3.

2.5 Discussion

2.5.1 Benefits and drawbacks of phase diagram measurement through imaging emulsified phase-separated solutions

We have presented an emulsion-imaging method for quantifying the temperature-concentration phase diagram of LLPS macromolecular solutions. Our results validate the method both in that the measured NS phase diagrams are consistent with prior measurements and predictions [13, 30, 58], and through our direct confirmation of the applicability of the lever rule (Fig. 2.2), which is expected to hold based on fundamental thermodynamic and mass-action considerations.

As with other emulsion-based approaches [53–55], the method developed here offers a variety of benefits: First, centrifugation and/or direct handling are not required to assay the dense phase. Apart from adding processing time, direct handling can be technically difficult for biomolecular liquids, which are high-viscosity, condensed phases that tend to non-specifically adhere to surfaces (*e.g.*, pipette tips, tubes). A further benefit of the method is that it achieves very low sample use by portioning the sample into micron-scale water-in-oil droplets. Also, the ability to simultaneously image multiple emulsion droplets improves measurement precision, since each droplet represents an independent sample, their proximity ensures consistency of temperature, and their small size allows for rapid equilibration. Further, we showed that multiplexing is readily achieved by loading different samples in different channels on a single microscope slide, allowing assay of different solution conditions with a single temperature sweep.

The method is particularly good for resolving the concentration of the dense phase, $[\mathrm{NS}]_{\mathrm{den}}$, based on measuring slope of the lever-rule data (Fig. 2.2); notably, this is the phase whose properties are traditionally more difficult to assay. In contrast, a drawback

was the difficulty in accurate quantification of the dilute binodal. This arose specifically because of the extraordinarily low dilute-phase density of the NS system. Particularly, our measurements of total NS concentration, [NS], carried an uncertainty of, at best ≈ 1 μM, which is ≈ 0.06 g/L for $z = 4$, leading to a similar magnitude of the uncertainty in the best-fit values of the x-intercept in the lever-rule data. However, the values of $[\mathrm{NS}]_{\mathrm{dil}}$ at low T were typically $\lesssim 0.1$ g/L, and thus could not be precisely resolved. A previous article using UV absorbance reported higher values, $[\mathrm{NS}]_{\mathrm{dil}} \approx 0.5$ g/L for $z = 4$, but interpreted those values as being an overestimate due to the presence of malformed NSs [13]. The low values found here for $[\mathrm{NS}]_{\mathrm{dil}}$ are consistent with a recent numerical calculation of the NS phase diagram that found $[\mathrm{NS}]_{\mathrm{dil}} \lesssim 0.1$ g/L under similar conditions [36]. Generally, since the issues in quantifying $[\mathrm{NS}]_{\mathrm{dil}}$ arose from limitations in our measurements of the total NS concentration, rather than a systematic issue with the imaging, the technique should be able to quantify the dilute-solution binodal in systems where it falls at higher concentrations.

We rely on fluorescent labeling to quantify condensate volume fraction, which is then used to estimate the phase diagram. This differs from other fluorescent phase-measurement approaches, in which the absolute fluorescent intensity of each phase is used to estimate concentration [37,68,69]. Using fluorescent intensity requires a separate calibration to relate intensities to concentrations; further, intensity measurements can be complicated by photophysical phenomena, such as quenching interactions amongst dyes, or between dyes and the macromolecule, that affect intensity [70–72]. In contrast, our ϕ-oriented approach is insensitive to absolute intensity, so long as the two phases are bright enough to visualize and to be distinguished. Generally, fluorescent approaches have the drawback that labelling can be difficult, and can potentially perturb the system's behavior. Accordingly, label-free approaches have been developed to measure phase behavior [70, 73], including a recent work that used bright-field images to measure ϕ_{den}

of condensates within emulsion droplets [55]. In comparison to that work, a benefit of our approach is the relative simplicity of fluorescent imaging, which allows us to use a mechanistic, quantitative model of the intensity distribution (i.e. the double-sphere function). Further, in fitting that model to the data, we utilize all pixels in the droplet image, including both pixels near the sphere boundaries, and those away from boundaries that carry information on the curvature (and thus radius) of each sphere (see Fig. 2.1B); this contrasts with the bright-field method that used an edge-detection approach focused on boundaries [55]. Because of this combination of a well-defined intensity profile, and efficient use of all available information, we achieve very low uncertainty (typically $< 1\%$) in our estimate of R, and thus extremely precise estimates of ϕ_{den}. Overall, then, there are benefits and drawbacks to the various methods; we expect the best approach will generally depend on the nature of the system in question.

2.5.2 Interpreting NS critical temperatures

Apart from development of the emulsion-imaging method, a second salient output of this work is the phase diagrams themselves, which yield insight into the mechanisms controlling the valence-limited NS system. As noted above, the phase diagrams uniformly show an upper critical solution temperature, consistent with the temperature-destabilized nature of the DNA hybridization bond, and a coexistence regime whose T_c and $[\text{NS}]_{\text{den}}$ increased with monovalent salt and nanostar valence, z.

The salt-dependence of T_c (Fig. 2.5) can be understood through the electrostatics of DNA hybridization: repulsion between negatively-charged DNA strands is reduced by the screening effect of added salt, causing hybridization strength (and thus T_c) to increase with [salt]. More quantitatively, we note that the differing charge densities of double-stranded and single-stranded DNA means that there is a change in the number

of salt ions localized near the DNA when it hybridizes [74], leading to a free energy cost of hybridization related to the chemical potential of the salt, $\mu_{\text{salt}} \sim T \log[\text{salt}]$. This ultimately gives rise to the log[salt] dependence of the measured T_c (Fig. 2.5). Both the mean-field and NS-SAFT models capture this log[salt] dependence because it is present in the Santa Lucia estimates of DNA thermodynamics [59], whose predictions inform both models.

The mechanisms underlying the dependence of T_c on z are more involved. Our experimental results show a strong decrease in T_c when z decreases to 3. Simple mean-field pictures fail to account for this behavior, but it is captured by the NS-SAFT model. Interestingly, the mean-field predictions are not very far off for higher valences, which indicates the dominant role in such systems is played by the thermal stability of the DNA bond itself. Yet the mean-field model, in all conditions, predicts transitions at higher temperatures than experimentally observed. This is likely because it overestimates the translational freedom of the bound state (i.e. the model implicitly assumes the bound state is a freely-translating dimer, rather than a condensed DNA network). The failure of the mean-field model emphasizes that bond connectivity (rather than just bond strength) is crucial to the behavior of low-valence NS networks.

In contrast, the NS-SAFT model (adapted here from Rovigatti *et al.* [36, 58, 61]) includes connectivity, and indeed is generally successful in predicting T_c vs. z, including the large decrease at $z = 3$. However, the NS-SAFT predictions are not perfectly aligned with experiment. At higher valences, it is possible that this is due to the approximation used for the excluded-volume parameter ($B_2 \sim z$), meaning the prediction might be improved by carrying out direct simulations to find $B_2(z = 6)$. But it is also possible that the experiments carry systematic errors that are not accounted for. For example, the method for estimating T_c from melting temperatures is somewhat inexact. Further, it is also possible that sample quality was imperfect: misassembled NSs can result from

issues with stoichiometry of the constituent strands, or from errors in the DNA synthesis process, and their presence could affect the measured phase behavior, as noted previously [13].

2.5.3 Low-T behavior of condensate density

Our phase diagram measurements indicate that, in a given condition, the coexistence concentration of the dense phase, $[\mathrm{NS}]_{\mathrm{den}}$, tends to rapidly stabilize as T decreases below T_c. This feature was also observed by others [13, 36], and has been attributed to the strong (exponential) increase in DNA hybridization strength as temperature decreases– essentially, as T decreases below T_c, the binding energy quickly becomes strong enough to ensure that the number of bonds in the system is maximized; thus further temperature decrease does not lead to more bonds, causing the network density to stabilize. Interestingly, we observed two conditions ($z = 4$ and $z = 3$ at 150 mM NaCl) in which there is a slow variation of $[\mathrm{NS}]_{\mathrm{den}}$ below T_c. Because the exponential dependence of hybridization strength on temperature should still hold, this feature is likely instead due to conformational behaviors and/or structural transitions of the NSs in these conditions.

To gain further insight into the values of $\mathrm{NS}_{\mathrm{den}}$ at low T, it is useful to establish a metric for comparison. Analogous to Biffi *et al.* [13], we posit that, for the 4- and 6-armed NSs, relevant metrics are the density when arranged into, respectively, diamond and simple-cubic lattices, representing a potential structure for particles with, respectively, 4 and 6 nearest neighbors. We estimate the NS-NS center-to-center distance to be 18.4 nm, if the DNA arms are fully stretched (see Appendix,, Section A.7). Then, the density of an $z = 4$ NS diamond lattice is 10.4 g/L, and that of an $z = 6$ simple cubic lattice is 23.2 g/L. The measured low-T values of $\mathrm{NS}_{\mathrm{den}}$, for $z = 4$ and $z = 6$, exceed these values. This occurs partially because the entropic elasticity of the DNA arms pulls the

particles closer together, and, for $z = 4$, likely due to a tendency for the NSs to adopt planar structures [61]. Generally, dense states are electrostatically unfavorable, as they bring the negatively-charged phosphates along the DNA backbones into close proximity; accordingly, our data show adding salt favors a denser DNA liquid for both $z = 3$ and $z = 4$ NSs, as has been previously observed [30]. That said, we note that the $z = 4$ density at the lowest salt approaches the diamond lattice value, perhaps indicating the high inter-arm electrostatic repulsion in those conditions favors that structure; direct structural analysis would of course be needed to confirm this.

For both $z = 3$ and 4, we found little increase in low-T $[\mathrm{NS}]_{\mathrm{den}}$ when switching from [NaCl] = 150 mM to 300 mM. This differs from a previous result on $z = 4$ NSs that used a centrifugation assay, and observed a strict monotonic increase in density with salt, though over a slightly different range (250 mM to 1000 mM NaCl) [30]. The discrepancy could be attributed to the differences in the sequence design between the two experiments. Alternatively, we speculate that more complex mechanisms might be relevant, such as the differing effects of electrostatic screening on inter-NS interactions versus intra-NS interactions, e.g at the junction.

The increase in low-T values of $[\mathrm{NS}]_{\mathrm{den}}$ with valence is expected, since higher-z NSs have both more DNA per particle (e.g. an $z = 6$ particle contains twice as much DNA as an $z = 3$ particle), and because NSs with larger z will tend to have more bound neighbors. Indeed, the $z = 6$ NSs have more than twice the low-T density of the $z = 3$ NSs, which underlines the role of the bound neighbors. However, the near-equivalence of the low-T condensate density between 4 and 5 armed NSs is not consistent with this picture. Intriguingly, a recent rheology experiment observed a similar trend with valence of elasticity [27] as observed here for density: namely, the modulus of the rubber plateau of NS condensates clearly increased when moving from $z = 3$ to 4 to 6, but the modulus for $z = 5$ was similar to $z = 4$. We speculate that both results are due to the $z = 5$ NS

adopting a unique structure in the condensate, relative to the 4- and 6-armed particles, but more work is needed to clarify this.

2.6 Conclusion

We have established a simple method for obtaining the temperature-concentration phase diagram of a liquid-liquid phase separating macromolecular system in which water-in-oil emulsion droplets, at controlled temperature, are imaged with a low-magnification, low-NA fluorescence microscope. The method offers various advantages, including no direct handling of the dense state, low sample-volume use, and precise extraction of condensate volume fraction. The method is readily applied to other macromolecular systems that can be fluorescently labeled. Here, we applied it to the study of LLPS exhibited by multivalent DNA NSs, finding strong effects of particle valence and salt concentration on the phase diagram. The results confirm predictions of the NS-SAFT numerical model, and generally give insight into limited-valence phase separation.

Chapter 3

Increasing valence pushes DNA nanostar networks to the isostatic point

3.1 Preamble

The content of chapter 3 and appendix B is the result of a collaboration with Tynan Kennedy, Deborah K. Fygenson, and Omar A. Saleh. The work here is reprinted with permission from PNAS 116, no. 15, 7238 (2019), Copyright 2019 National Academy of Sciences.

3.2 Introduction

Transient hydrogels are water-laden, transiently cross-linked polymer or colloidal networks that occur naturally in cells and tissues and have been synthesized and developed for a wide range of applications from hygienic and food products to diagnostic and therapeutic technologies. Much of the utility of transient hydrogels derives from their viscoelastic nature, which combines the stress-bearing abilities of a solid with the permeability and flow characteristics of a liquid [75, 76]. Understanding the microscopic origins of

these mechanical properties is an important goal for both directing transient hydrogel engineering and deciphering their biological designs.

In general, transient hydrogel mechanics derive from the elastic properties of their constituent polymer/colloidal chains, the stability of cross-links, and the connectivity of the network [1]. Network connectivity can be defined in terms of junction multiplicity or valence, z, *i.e.* the average number of network chains that meet at a node. While connectivity is a potent effector of mechanics in principle [15,16,77], it is relatively difficult to determine and control in practice [21–24]. This is because cross-links are traditionally made, either by entanglement, by weak bonds (hydrogen bonds, van der Waals forces, hydrophobic or electrostatic interactions), or by chemically reactive side-groups, with junctions whose valence is uncontrolled or relatively small (typically $3 \leq z \leq 4$), and not revealed by either scattering or imaging techniques.

The programmability and thermal reversibility of Watson-Crick base-pairing makes DNA intriguing as a model material in which to study the effect of network connectivity on hydrogel mechanics. Multi-armed "immobile junctions" were among the first DNA nanostructures to be rationally designed and self-assembled [78]. Pioneering work by Luo et al. demonstrated the feasibility of producing macroscopic quantities of fully-synthetic DNA hydrogels based on 3- and 4-armed junctions [79] that bind via complementary "sticky-ends", and explored their potential for various biotechnological applications [80].

More recently, Sciortino and co-workers engineered greater flexibility into the immobile junction design by incorporating unpaired bases at the vertex and sticky-ends to create "DNA nanostars" (DNAns) (Fig. 3.1A) [13, 31, 34, 35, 61, 81]. They found that tetra-valent DNAns transition from a fluid to an equilibrium gel upon cooling [31,61,81], with network dynamics controlled by the sticky-end interaction strength [13,30,34]. Equilibrium gel formation requires both limited valence ($z < 12$) [2, 13, 14, 34, 82] and significant flexibility [81, 83], as conferred by the unpaired bases in the DNAns design (Fig.

3.1A).

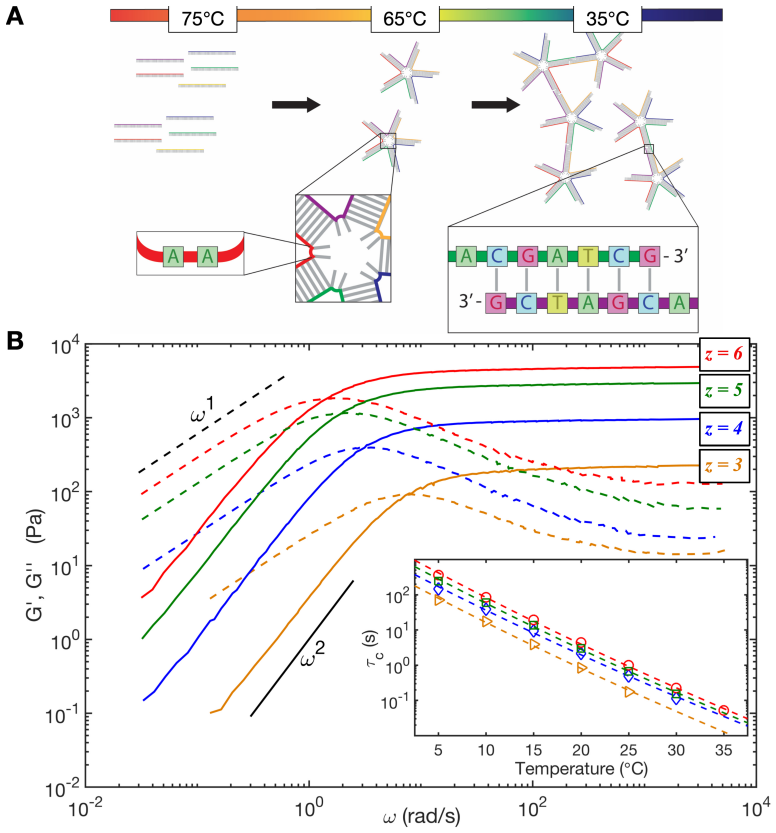

Figure 3.1: **(A)**: 2D cartoon depicting the formation of a five-arm DNAns network as a function of temperature. Every DNAns has unpaired adenines at the base of each arm to enhance vertex flexibility. Each arm is a 21 bp double-helix, $\approx$ 8.5 nm long, that ends in a single-stranded overhang, consisting of an unpaired adenine and a six-nucleotide palindromic sequence, called the sticky-end (boxed at right). **(B)** Frequency-dependent mechanical response of DNAns networks at $\gamma = 5\%$ and $T_{\text{ref}} = 20°\text{C}$. The storage modulus, G' (solid), and loss modulus, G'' (dashed), cross at a frequency, ω_c, that is the inverse of the relaxation time, τ_c. **Inset**: Arrhenius fits to $\tau_c(T)$ have a common slope corresponding to the activation energy for network rearrangement. Orange triangles, blue diamonds, green squares, and red circles correspond to $z = 3, 4, 5$, and 6 at DNAns concentrations of (500 ± 10) μM, (490 ± 10) μM, (490 ± 20) μM, and (450 ± 30) μM, respectively.

Here, we apply bulk oscillatory rheology to solutions of $z = 3$, 4, 5 and 6-armed DNAns equilibrium gels over accessible [DNAns] and temperatures to probe the effect of valence on network mechanics and structure. The equilibrium and liquid-like nature of DNAns networks ensures that material handling is easy and that the network's mechanical and

structural properties are history-independent. We find that the trends with valence of network stiffness (plateau modulus) and strain-hardening are consistent with a network whose mechanics are controlled by a combination of entropic elasticity of network chains and an isostatic critical-point occurring at a DNAns valence of $5 < z_c \leq 6$.

3.3 Methods

A brief explanation of the rheological methods are listed here. A more detailed description of the materials and methods are in Appendix B.

We used oscillatory rheology to measure the frequency-dependent storage, G', and loss, G'', moduli of solutions of DNAns with different arm numbers at various concentrations and temperatures. Then, for each solution, we used time-temperature superposition (TTS) to shift curves in both frequency and modulus, thus generating master rheological curves that spanned six decades of frequency, ω, at a reference temperature of 20°C (Fig. 3.1B; Appendix, section S2a). At this temperature, a thermodynamic model of sticky-end hybridization predicts $> 98\%$ binding [84] (Appendix, section S1b).

Frequency sweeps were performed at a constant strain, $\gamma = 5\%$, well below the onset of non-linearity (Fig. 3.3). For all z, repeated measurements of G' and G'' were independent of rates of cooling and heating for ≤ 15°C/min (Appendix, Fig. B.4), confirming that DNAns form thermoreversible, equilibrium networks [13].

We also assessed the various networks' linear and nonlinear elasticity by performing oscillatory stress-strain measurements at a temperature (20°C) and frequency ($\omega \geq 63$ rad/s) corresponding to the elastic-plateau regime of all valences.

3.4 Results

DNAns solutions of every arm number behaved like Maxwellian viscoelastic fluids, with low-frequency liquid behavior ($G'' > G'$, with $G' \sim \omega^2$ and $G'' \sim \omega$) separated by a crossover frequency ω_c from high frequency solid-like behavior ($G' > G''$, with a plateau modulus G'_p; Fig. 3.1B) [1, 31]. While it is possible for such a crossover to result from solvent drag effects [17, 85, 86], we estimate that a drag-induced crossover would occur at MHz frequencies, well above our measured values of ω_c (Appendix, section S2c). Instead, we note that the characteristic time for network reconfiguration shows an Arrhenius dependence, $\tau_c = 2\pi/\omega_c \propto e^{-E_a/RT}$ (Fig. 3.1B, inset) with an activation energy E_a that is the same for all z and approximately equal to the enthalpy of hybridization of a single nanostar overhang sequence (Appendix, Fig. B.7, consistent with previous dynamic measurements [13, 30, 34]. We thus interpret τ_c as corresponding to bond-breaking events, meaning that the high-frequency plateau modulus reflects the stiffness of an instantaneously bonded network.

To test how DNAns valence, z, affects network stiffness and structure, we measured the plateau modulus, G'_p, as a function of DNAns concentrations, [DNAns], for $z = \{3, 4, 5, 6\}$. G'_p increased with z more than might be expected based on density alone (Fig. 3.2). That is, an $(f+1)$-armed network was always stiffer than an z-armed network with the same volume fraction, ϕ, of DNAns arms (Fig. 3.2, inset). Further, G'_p increased with [DNAns] as a power-law, $G'_p \sim [\text{DNAns}]^t$, with a best-fit exponent that decreases from $t = 1.8 \pm 0.1$ for $z = 3$ to $t = 1.0 \pm 0.2$ for $z = 6$.

To gain insight on how valence affects the various networks' strain behavior, we performed oscillatory stress-strain measurements during their elastic-response regime (e.g., $T = 20°\text{C}$ and $\omega \geq 63$ rad/s). For $\gamma \leq 10\%$, all networks exhibited linear elasticity (constant G') (Fig. 3.3). At higher γ, most networks showed signs of strain-hardening, as

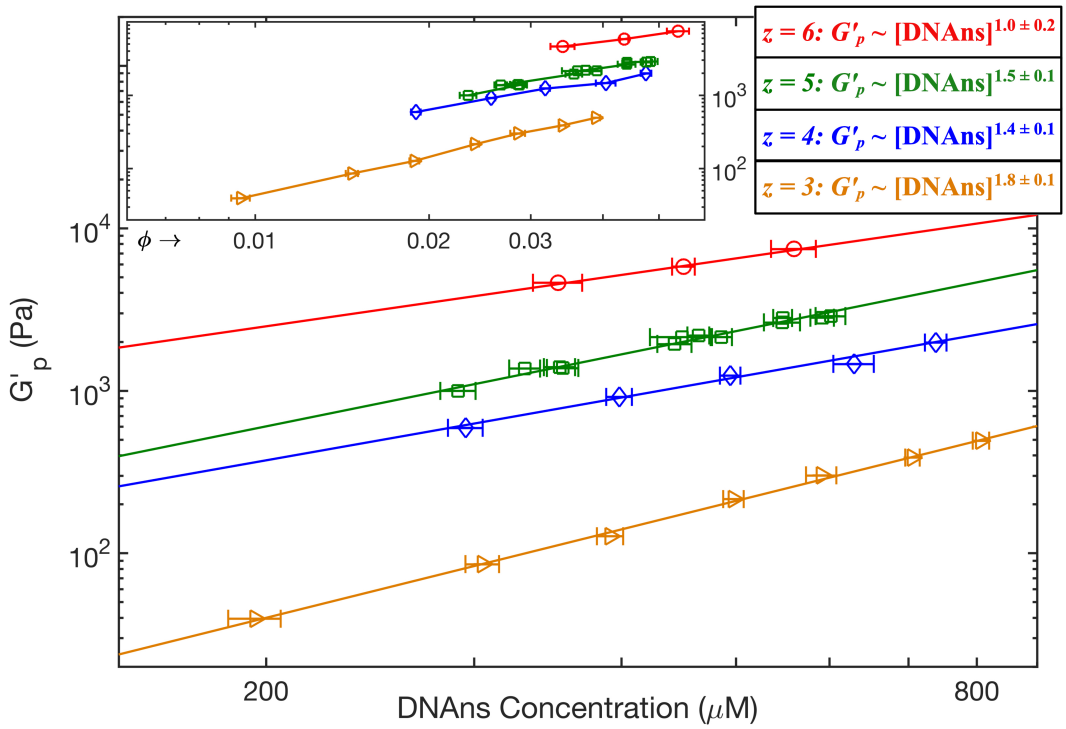

Figure 3.2: Log-log plot of the plateau modulus, G'_p, as a function of DNAns concentration at $T = 20°C$ and $\gamma = 5\%$ for $z = 3$ (orange triangles), 4 (blue diamonds), 5 (green squares), and 6 (red circles). Solid lines show fitted power laws, $G'_p \sim [\text{DNAns}]^t$; labels give best-fit exponents with standard fitting-error estimates. **Inset**: Log-log plot of G'_p as a function of DNAns arm volume fraction, $\phi = z \cdot v \cdot [\text{DNAns}]$, where $v = 26.7$ nm^3 is the solid cylinder volume equivalent of a DNAns arm. Solid lines connecting the data points are guides for the eye. **Need to update plot to have "$z = 3$", etc.**

discussed below. Finally, in all cases, the $G'(\gamma)$ curve terminated with a sudden decrease, or yielding of the network, typically associated with bond breaking [1, 87, 88].

We define the yield strain γ_m as that which resulted in the largest measured G'. The $z = 3$ and $z = 4$ networks were extensible, showing relatively large yield strains of $\gamma_m \approx 1.3$ and 0.5, respectively. Accordingly, in those networks the strain-hardening regime was broad and amenable to analysis: for $\gamma < \gamma_m$, the regime was well-fit by a relation proposed by Seitz *et al.* [89–91], $G'(\gamma)/G'(\gamma \to 0) \sim \exp\left((\gamma/\gamma^*)^2\right)$, with best-fit values of $\gamma^* \approx 1.8$ and 1.2 for $z = 3$ and $z = 4$, respectively. γ_m and γ^* did not vary significantly with [DNAns] (Appendix, Fig. B.10A and B).

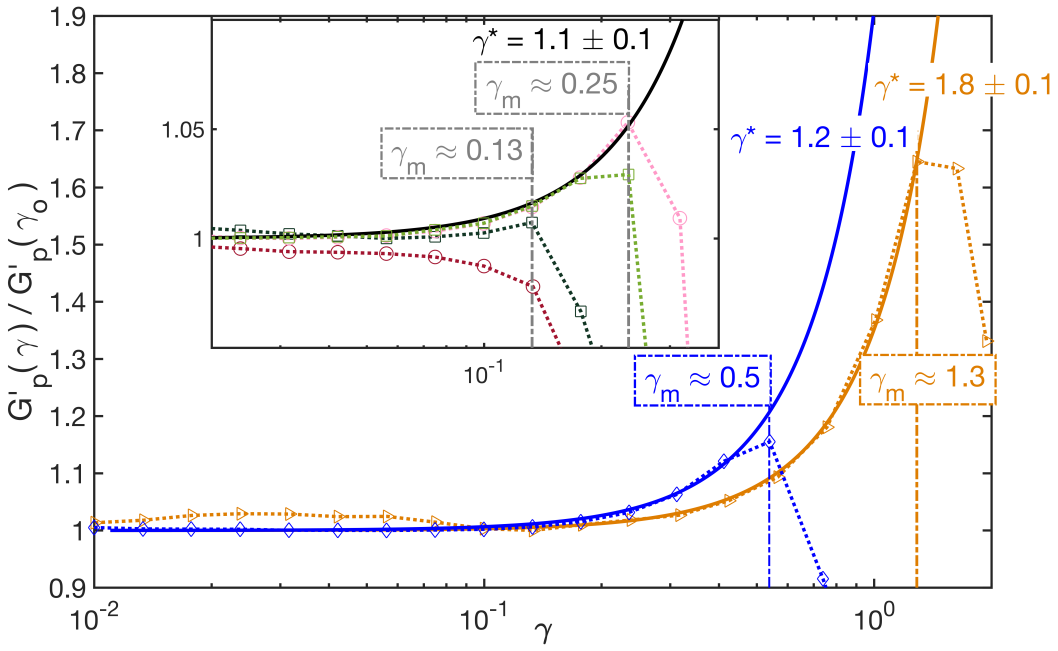

Figure 3.3: Normalized plateau modulus, $G'_p(\gamma)/G'_p(\gamma_o)$, of DNAns networks as a function of strain, γ, in the elastic-plateau regime ($\omega = 63$ rad/s, $T = 20°$C) for $z = 3$ (orange triangles) and 4 (blue diamonds) at [DNAns] of (500 ± 10) μM and (490 ± 10) μM, respectively. Solid lines are fits of $\exp[(\gamma/\gamma^*)^2]$ for $(\gamma \leq \gamma_m)$, where γ_m (vertical dash-dot line) is the strain that maximizes G'_p and γ^* is the characteristic strain scale for stiffening. **Inset**: Same plots for $z = 5$ at [DNAns] of (300 ± 10) μM (light green) and (550 ± 30) μM (dark green) and for $z = 6$ at [DNAns] of (350 ± 20) μM (pink) and (550 ± 30) μM (dark red). The solid black line denotes $\exp((\gamma/1.1)^2)$, which captures the non-linear elasticity of the two lower concentration $z = 5$ and $z = 6$ networks.

For $z = 5$ and $z = 6$, relatively small yield strains ($\gamma_m \approx 0.2$) curtailed the strain-hardening regime, yet all $z = 5$ curves showed a resolvable strain hardening, as did the $z = 6$ curve at the lowest [DNAns] (Fig. 3.3 inset). These strain-hardening behaviors, while modest, could also be fit to the Seitz expression, with $\gamma^* \approx 1.1$ for the least concentrated $z = 5$ and $z = 6$ curve (Appendix, Fig. B.10A).

3.5 Discussion

An isostatic picture explains plateau modulus behavior of DNAns networks

The trend of DNAns network stiffness, G'_p, with DNAns valence, z, is qualitatively consistent with the expectation that junctions of greater valence augment network modulus by creating a greater density of stress-bearing chains. The 'Phantom-network' elastic model [1, 21] quantifies this relation by extending classic rubber elasticity models to account for valence-dependent fixation of the junctions connecting network chains. Specifically, it predicts $G' \propto \phi \cdot (z-2)/z$. Our data are not consistent with this picture. G'_p increases non-linearly with ϕ for $z = 3, 4$ and 5 (Fig. 3.2). More strikingly, at constant ϕ, G'_p increases roughly 10-fold from $z = 3$ to $z = 6$, far exceeding the phantom-network model's prediction of two-fold stiffening for those valences (Fig. 3.2: inset; Appendix, Fig. B.11).

We instead posit that the variation of DNAns network elasticity with valence is explained by the presence of a Maxwell isostatic point [15,92] at a critical valence value, z_c. The utility of the isostatic point in explaining biomolecular gel mechanics has recently been explored [16, 77, 93–98]. The isostatic point occurs when the translational freedom of a junction is exactly constrained by the connections (network chains) emanating from that junction [15,16,77,92–96]. If each network chain supplies only central forces between the two junctions it connects (*i.e.*, it acts only by resisting stretching), then $z_c = 6$ [15,16]. In practice, real network chains also supply tangential forces, due to a combination of non-zero bending stiffness and rotational constraints imposed at the point of fixation to the junction. The effect of non-zero bend stiffness is to decrease z_c below 6 by an amount dependent on the relative magnitudes of bend and stretch stiffness [16, 96].

Regardless of the precise value of z_c, the presence of an isostatic point alters network modulus in a manner consistent with our observations. Networks with $z < z_c$ have underconstrained junctions whose positions are easily perturbed without significant stretching of network chains [16, 92–94, 96]. These networks are thus intrinsically floppy, with a low modulus dictated by chain bend behavior. In contrast, $z > z_c$ networks have fixed junctions that can only be moved by stretching network chains [16, 92–94, 96], and are accordingly relatively high-modulus materials. The isostatic model thus predicts a steep increase in modulus as z increases through z_c [16], in qualitative agreement with our data (Fig. 3.2; Appendix, Fig. B.11).

Other features of our data also agree with isostatic model predictions: Stretch-dominated, super-isostatic ($z > f_c$) networks are expected to have a linear scaling of G'_p with ϕ [91, 99–103], as seen at $z = 6$, but not at smaller valences (Fig. 3.2). This implies that the critical valence of our DNAns network is between $5 < z_c \leq 6$, consistent with the prediction of $z_c = 6$ for network chains that have vanishing bending stiffness and little rotational constraint at the junction [16, 93, 96]. In the DNAs, we posit these features are a consequence of the unpaired bases flanking the double helical arms at the overhang and at the junction, consistent with flexibility seen in simulations of DNAns [61].

It is intriguing that network stiffness is not perfectly monotonic with valence. The $z = 3$ and $z = 6$ networks show strongly divergent behaviors, demarcating clear endpoints in the exponent t. The $z = 4$ and 5 networks both lie unambiguously between those endpoints; however, their trend is not monotonic: t is larger for $z = 5$ than $z = 4$. This disagrees with the monotonicity in valence expected from a purely isostatic explanation. We speculate this is due to a fundamental asymmetry in the $z = 5$ nanostars. Electrostatics favor ground states in which the negatively-charged DNA arms are equally distant from their nearest neighbors. For $z = 4$ and 6, there are well-defined ground-state

configurations in which the arms point to the vertices of corresponding platonic solids. However, there is no such configuration available for $z = 5$. The resulting frustration could explain the more under-constrained behavior of $z = 5$, i.e. with t values closer to $z = 3$ than $z = 6$.

Valence-dependence of strain-hardening is also consistent with an isostatic picture

As seen in Fig. 3.3, the $z = 3$ and 4 networks exhibit marked strain-hardening behaviors, with modulus increasing by $\sim 60\%$ and $\sim 15\%$, respectively, before the material yields. Strain hardening of polymeric materials generally occurs when network chains, initially in an unstretched, thermally-fluctuating configuration, rigidify under strain as they are straightened to lengths approaching their contour length [1,89–91,93,94]. Thus, the strain-hardening of the $z = 3$ and 4 networks indicates that stress-bearing chains have significant configurational freedom and, so, are under-constrained and sub-isostatic [93], consistent with the interpretation from the G'_p vs. [DNAns] behavior [96, 102].

This interpretation is also supported by the observation that, as with many polymeric and fibrous materials [89–91], DNAns networks strain harden according to $G' \sim \exp(\gamma/\gamma^*)^2$ (Fig. 3.3). As described by Seitz *et al.* [89], the fitting parameter γ^* can be related to the network chain's maximum uniaxial extension ratio, $\lambda_{\max}$, which measures the ratio of chain contour length to initial (unstretched) extension (Appendix, section S2c, Fig. B.12). Fits to our data give $\lambda_{\max} \approx 2.3 \pm 0.1$ and 1.7 ± 0.1 for $z = 3$ and 4, respectively, indicating the stress-bearing chains in an $z = 3$ network are initially less stretched than those in an $z = 4$ network, presumably due to being more floppy.

The non-linear elastic response of the $z = 5$ and $z = 6$ networks is more subtle, but still consistent with the isostatic viewpoint [93]. For $z = 5$, at all concentrations

measured, the material hardens before yielding, but only by $\sim 2\%$. The curves are again well-fit by the Seitz equation [89–91] with $\lambda_{\max} = 1.9 \pm 0.2$, indicating the network chains are initially more stretched than $z = 3$. This is consistent with the $z = 5$ network being sub-isostatic, but closer to the critical point than $z = 3$.

For $z = 6$, a similarly small ($\sim 2\%$) strain hardening is seen at the lowest concentration, but at the other two concentrations strain hardening is not evident. We interpret the lack of strain hardening as an indication that junctions in those networks lack configurational freedom and, consequently, the networks are isostatic [93, 94].

Analysis of yield behavior measures cluster size, confirms entropic origin of elasticity

More insight into network structure is enabled by analysis of yield behavior. Yielding occurs at a stress $\sigma_y \sim F_c/\xi^2$, where F_c is the characteristic bond-breaking force and ξ is the characteristic distance between the first bonds that break [102]. Single-molecule manipulation experiments have directly quantified F_c for DNA overhangs loaded in shear, typically finding $F_c \approx 50$ pN for overhangs of 20 to 30 bp [104]. Thus, for the shorter 6 bp overhang used here, $F_c \approx 10$ pN is a reasonable estimate for a scaling calculation.

Using this estimate, and our measured σ_y, we find ξ decreases from $\xi \approx 200 - 300$ nm at the lowest [DNAns] to $\xi \approx 100$ nm at the highest [DNAns], for $z = 3, 4, 5$ (Fig. 3.4A). For $z = 6$, on the other hand, ξ is smaller, $\approx 90 \pm 30$ nm, and independent of [DNAns] (Fig. 3.4A). In all cases, ξ is much larger than the nanostar size (≈ 15 nm). It is thus an emergent length scale of the system of roughly 5 to 20 DNA nanostars in width. We interpret ξ as a measure of cluster size: the characteristic distance between bonds that carry large forces upon strain. Within a cluster (*i.e.*, between those vulnerable bonds), the force is dispersed across many DNAns in parallel.

This interpretation is consistent with simulations that report cluster-like inhomogeneities in equilibrium gels [105]. We emphasize that these clusters are different than those found in (non-equilibrium) colloidal gels [106]. In DNAns gels, the clusters are transient, enduring only for timescales less than τ_c. On longer time scales, the network restructures and behaves as a liquid, with an effectively homogeneous density.

Given ξ, we can interpret network modulus in terms of the spring constant per cluster, K_ξ, which provides a clue to the fundamental origin of elasticity in the system. From $K_\xi \approx G_p' \cdot \xi$ we find that K_ξ increases with valence and concentration (Fig. 3.4B) [102]. To interpret these values, we compare them to the spring constant, K_{FJC}, of the fundamental entropic-elastic unit in the system: a bonded pair of DNAns arms that connects two junctions. Considering the pair of arms as a two-segment, freely-jointed chain with segment (Kuhn) length b equal to the DNAns arm length, the expected spring constant is $K_{\mathrm{FJC}} = 3k_BT/2b^2 \approx 85$ μN/m at $T = 20°$C, which lies in the middle of the estimated K_ξ values. This similarity indicates that entropic elasticity arising from DNAns arm configurational freedom controls network modulus. For $z = 3$, $K_\xi < K_{\mathrm{FJC}}$, as would occur for DNAns loaded in series; this is consistent with the $z = 3$ cluster containing a single, dominant stress-bearing chain of DNAns. For the higher-valence networks, $K_\xi > K_{\mathrm{FJC}}$, likely due to clusters containing more parallelized and interconnected stress-bearing chains.

The entropic origin of network elasticity explains why G_p' increases only about ten-fold as z goes from 3 to 6 (Appendix, Fig. B.11). Simulations of networks of non-entropic (athermal) springs predict enormous, multi-decade increases in modulus as z increases through the isostatic point [16]. The comparatively modest increase we observe can be attributed to entropic rigidification, which is predicted to mask the modulus increment across the isostatic transition [97, 98].

Origin of elastic exponents in sub-isostatic networks

A potential explanation for the non-linear power-law behaviors of the sub-isostatic networks can be found by comparing our measured exponents with the results of percolation theory. We focus on the $z = 3$ system for which we have the broadest range of [DNAns], and thus the best estimates. The exponent of ξ vs. DNAns concentration, -0.8 ± 0.1, is consistent with the prediction from percolation theory in three dimensions for the scaling of correlation length with bond concentration, $\nu \approx -0.88$ [1]. Further, the $z = 3$ exponent of G'_p vs. [DNAns], $t = 1.8 \pm 0.1$, which was measured independently of ξ, is also consistent with 3D percolation theory predictions of $t \approx 1.9$ [107]. Experimentally, similar values of t were measured in gels formed from trivalent gelatin, and attributed to percolation behavior [108–110].

Within percolation models, the value of t ultimately derives from fractal exponents describing network structure within clusters. For example, theory predicts that the shortest path through a 3D percolated cluster has a fractal dimension $d_{min} = 1.25$ [111]. If that shortest path dominates cluster elasticity (consistent with the single-chain interpretation of K_ξ for $z = 3$), and taking the path to consist of N DNAns in series, we expect $K_\xi \sim 1/N \sim \xi^{-d_{min}}$. This is indeed close to the measured scaling of $K_\xi \sim \xi^{-1.2 \pm 0.1}$ (Fig. 3.4B inset). Since $G'_p \sim K_\xi/\xi$, we see that the measured estimates of $d_{min} \approx 1.2$ and of $\nu \approx -0.8$ gives rise to the value $t = -\nu(d_{min} + 1) \approx 1.8$.

Although the correspondence of our concentration-dependent scalings with percolation exponents is intriguing, some caution is warranted. First, our measurements show power-law behaviors of G'_p and ξ with non-normalized concentration, while theory [1,111] and prior experiment [108] observe such behavior only after correcting for a critical concentration; the reason for this discrepancy is unclear. Second, scattering studies can measure the cluster size, ξ, directly and such direct structural evidence is needed to give

a percolation interpretation firm support.

3.6 Conclusion

Our work highlights the key role of valence in controlling the elasticity of a hydrogel. Notably, for the same density of DNAns arms, a 10-fold gain in stiffness results from using $z = 6$ rather than $z = 3$ DNAns. At the same time, increasing valence dramatically diminishes network extensibility because junctions become more constrained as network connectivity increases. Our results are consistent with an isostatic interpretation: there exists a critical connectivity threshold beyond which stress-bearing elements become fully constrained and the network loses configurational freedom, leading to dramatically increased stiffness, reduced yield strain, and a loss of strain-hardening.

In this interpretation, the $z = 3, 4, 5$ networks are sub-isostatic, with enough configurational freedom at the particle level to exhibit strain-stiffening behavior and a non-linear dependence of plateau modulus on particle concentration. The rigidity of these floppy networks is attributed to the entropic elasticity of network chains, with a further role potentially played by a percolation-like network structure. In contrast, the $z = 6$ network is at or above the isostatic threshold, with highly constrained junctions and minimal freedom in the stress-bearing chains. The lack of contortions results in little to no extensibility or strain stiffening. The location of the critical threshold at $z = 6$ behavior is consistent with expectations for a network with flexible junctions [16,97,98], here insured by the unpaired bases present in the center of the DNAns.

We suggest that the insights gained here, regarding the interplay of valence, entropic elasticity, and network structure, can be extended to other DNAns-like particles to open new avenues for tuning material elasticity.

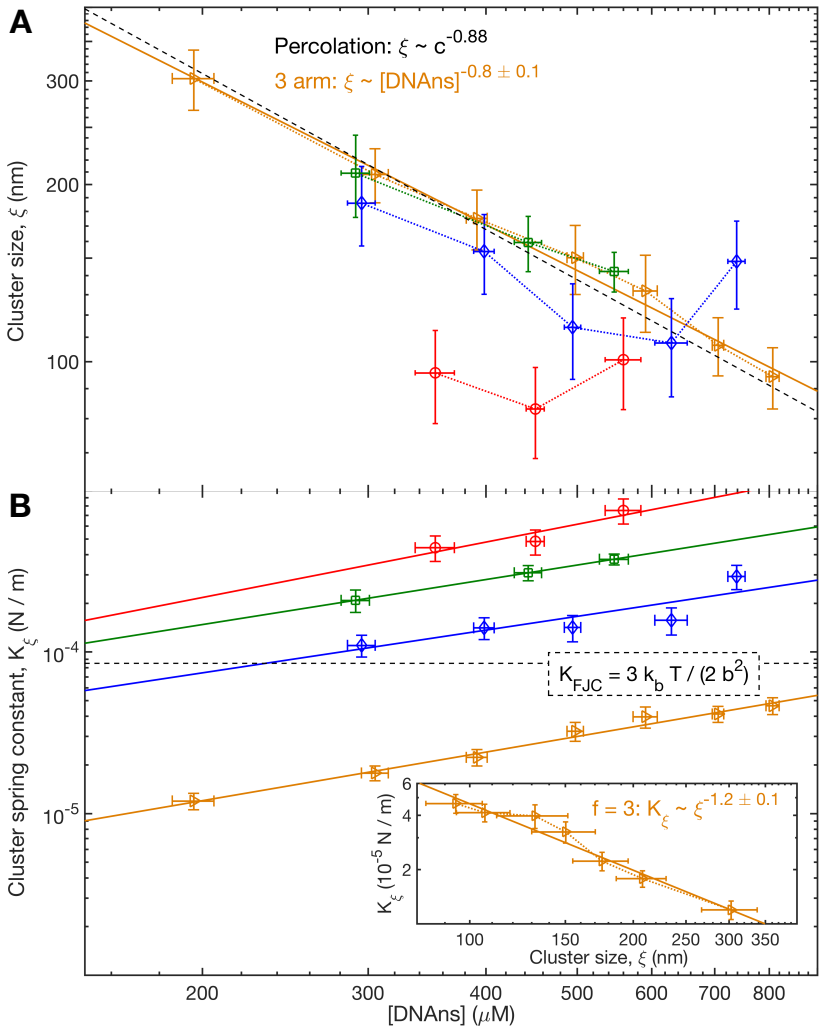

Figure 3.4: Log-log plots of **(A)** cluster size, ξ, and **(B)** cluster spring constant, K_ξ, as a function of [DNAns] for $z = 3$ (orange triangles), 4 (blue diamonds), 5 (green squares), and 6 (red circles) at a temperature of $T = 20°\text{C}$. In **(A)**, the dashed line denotes the predicted scaling relation for 3D percolated clusters with c, the particle concentration from References [1] and [107]. In **(B)**, the dashed line denotes the spring constant, K_{FJC}, of an entropic spring composed of two freely-jointed (Kuhn) segments of length $b = 8.5$ nm (*i.e.*, with length of a DNAns arm) and the solid lines denote the measured power law relation for $K_\xi \sim [\text{DNAns}]^r$. **Inset:** Log-log plot of K_ξ as function of ξ for $z = 3$ at $T = 20°\text{C}$. The solid line denotes the relation $K_\xi \sim \xi^{-1.2\pm0.1}$, with standard error estimated from fitting.

Chapter 4

Power-law rheology in heterogeneously bonded DNA nanostar

4.1 Preamble

The content of chapter 4 and appendix C is the result of a collaboration with Omar A. Saleh and Deborah K. Fygenson. The study here is a manuscript in preparation for submission to PRL.

4.2 Introduction

In the last chapter we demonstrated that equilibrium NS gels are model materials to investigate the effects of connectivity in viscoelastic liquids. Recall, equilibrium gels are non-hysteretic viscoelastic networks in which junctions are connected by a limited number ($2 < z < 12$) of transient, flexible bonds [9, 10, 27, 28, 31, 32, 76]. Such bonds give the network enough entropy to stabilize a disordered-liquid state over a crystalline one [28] and make for a material with interesting behaviors, such as self-healing, that are attractive for industrial and biomedical applications [9–11, 27, 76].

To date, what is known about transient/equilibrium gel rheology comes from "homotypic" networks, in which all junction-to-junction bonds are of a single type/strength. Below the percolation threshold and under low strain, homotypic equilibrium gels exhibit Maxwell-like viscoelasticity: they flow like simple liquids on long time-scales, and deform elastically on short time-scales. Studies have shown that the characteristic time-scale, τ_c, that separates these behaviors is controlled by a combination of bond strength [9,27,76], junction separation [76], and particle valence (shown in the last chapter).

By contrast, near percolation, near isostaticity, or whenever hydrodynamic interactions become important, non-Maxwell power-law rheology emerges in the frequency-dependent storage and loss moduli, G' and G'' [17, 97, 112]. Non-Maxwell scaling laws for G' and G'' have been observed [31,113,114], simulated [17,97], and computed [17] in such networks. Many connections between network structure and the observed power-law exponents have been made [115,116], but are largely for colloidal networks which do not have transient bonds. An intuitive framework that can explain the scaling exponents in transient networks in terms of their network structure is lacking.

Here, we build such a framework by studying the rheology of transient "heterotypic" equilibrium gels, where the underlying colloids have differing bonds whose distinct strengths lead to dynamic percolation between two valences. Our gels are made of DNA nanostars (NS), star-like macromolecules whose designability allows for independent alteration of bond lifetime and junction valence. We made heterotypic equilibrium gels of a single NS by designing it to make both long-lived ($\sim$ 500 s), "strong", and short-lived ($\sim$ 0.1 s), "weak", NS-NS bonds (Fig. 4.1).

We observed non-Maxwell power-law rheology over time-scales that lie between the two bond life-times in two different heterotypic NS solutions. The distinct scaling laws of the two solutions were both consistent with a mean-field model that treats the weak-bond network as a viscous solvent through which fluctuations of the strong-bond network

diffuse to relieve stress. This same model accurately predicts the power-laws observed by others for both critically-percolated and critically-isostatic networks, both experimentally and in simulation. Thus, by relating the accessible relaxation modes to the elastic correlation length, ξ, our mean-field model provides a framework for understanding non-Maxwell scaling laws in equilibrium gels. In particular, it predicts a direct relationship between the power-law exponent of G' and the fractal dimension, $d_{\min}$, of the shortest stress-bearing chain within ξ-sized clusters of an equilibrium gel network.

4.3 Materials and Methods

To change valence and interaction strength with minimal structural perturbation, all NS used in this study had the same, six-armed structure (Fig. 4.1A). Each arm had either a weak, six-base-long 5′ overhang (α), a strong, eight-base-long 5′ overhang (γ), or no overhanging bases at all (x, *i.e.*, a blunt end; see Fig. C.2 for strand sequences). We refer to a NS that has m α-overhangs and n γ-overhangs or n absent overhangs as $\alpha_m\gamma_n$ or $\alpha_m x_n$, respectively. Any given NS was made by mixing its corresponding six HPLC-purified ssDNA oligomers to equal concentrations in pure water, then dehydrating the mixture and rehydrating it to a final NS concentration between 400 μM and 470 μM in Tris-buffered saline solution (300 mM NaCl, 40 mM Tris, pH 8.3), and, finally, annealing from 90°C to room temperature over $\sim$ 5 h. Once annealed, such concentrated NS solutions were too viscous to pipette, so a slant-cut pipette tip was used to scoop and place $\sim$ 100 μL on the stationary plate of a strain- and temperature-controlled rheometer (TA Instruments, Ares-G2). Oscillatory rheology measurements were performed in the linear viscoelastic regime ($\sim$ 1% strain) over a range of frequencies (0.1-10 Hz) and temperatures (5°C $\leq T \leq$ 50°C). All G' and G'' master curves were constructed using time-temperature superposition (TTS) at the reference temperature listed, as detailed

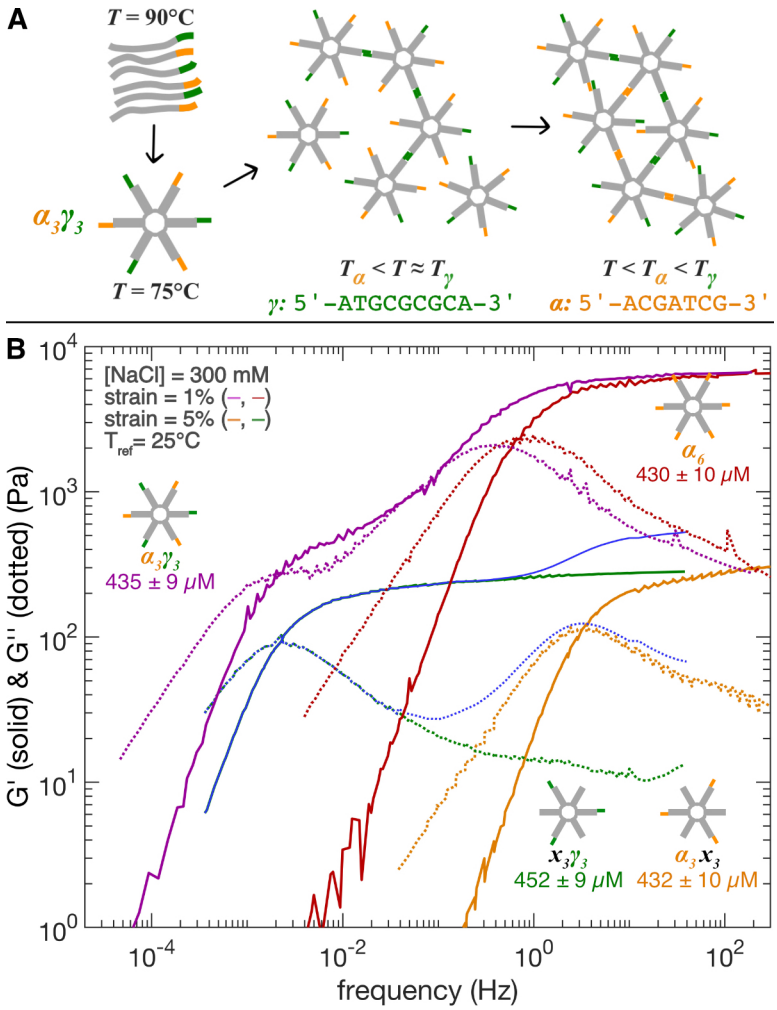

Figure 4.1: **(A)** Schematic of NS formation and network assembly as temperature, T, is lowered. T_α and T_γ denote the melting temperature of α and γ overhangs, respectively. **(B)** Frequency dependence of the bulk storage (G') and loss (G'') moduli of concentrated $\alpha_3 x_3$ (orange), $x_3\gamma_3$ (green), α_6 (red) and $\alpha_3\gamma_3$ (purple) NS solutions. The blue line is the sum of the moduli of $\alpha_3 x_3$ and $x_3\gamma_3$.

in [27]. Similarly, oscillatory strain sweep measurements of G' and G'' were performed over a range of strains $(1 - 300\%)$ at temperatures and frequencies spanning the non-Newtonian regime of the solution under investigation; TTS shift factors from the $G'(f)$ and $G''(f)$ master curves were used to shift the frequencies to $T_{\text{ref}} = 25°\text{C}$.

4.4 Results

Consistent with past work [27], solutions of homotypic NS (*i.e.*, those with only one type of NS-NS bond) were Maxwell-like, acting like simple fluids at low shear rates ($G' < G''$ for $f < f_c$) and elastic solids at high shear rates ($G' \approx G'_p > G''$ for $f > f_c$), with a single, characteristic relaxation time, $\tau_c \equiv 1/f_c$ [1]. This was true even if some arms lacked overhangs. Increasing valence from three ($\alpha_3 x_3$) to six (α_6) resulted in a 5-fold increase in τ_c and a 20-fold increase in G'_p (Fig. 4.1B, orange and red curves). Similar increases were previously observed for homotypic NS of different arm numbers (albeit at half the salt concentration) [27], suggesting that the blunt arms are rheologically inert.

In contrast, solutions of 6 arm heterotypic NSs were generally not Maxwell-like (Fig. 4.2), with the drastic change in viscoelastic spectra coming solely from a small sequence change to the NS design. In particular, the weak sticky-end sequence on some of the α_6 NS arms were slightly altered to make stronger sticky-ends (γ-sticky-ends). Designing the NS to have some γ-sticky-ends induced reproducible non-Maxwell power-law rheology at frequencies over which the α-bonds dissociate. In particular, rheology of $\alpha_4\gamma_2$ had a characteristic time scale, slightly longer than $f_c^{-1}(\alpha_6)$, beyond which the moduli scaled as $G' \sim f^1, G'' \sim f^{3/4}$. Rheology of $\alpha_3\gamma_3$ had two characteristic time scales, one slightly longer than $f_c^{-1}(\alpha_6)$ and another near $f_c^{-1}(x_3\gamma_3)$, between which both moduli scaled as $G' \sim G'' \sim f^{2/3}$. We want to emphasize here again that a significant alteration to the power-law stress-relaxation between the two heterotypic NSs was also achieved through changing DNA sequences to make two NSs that differ in valence of strong- and weak-sticky-ends.

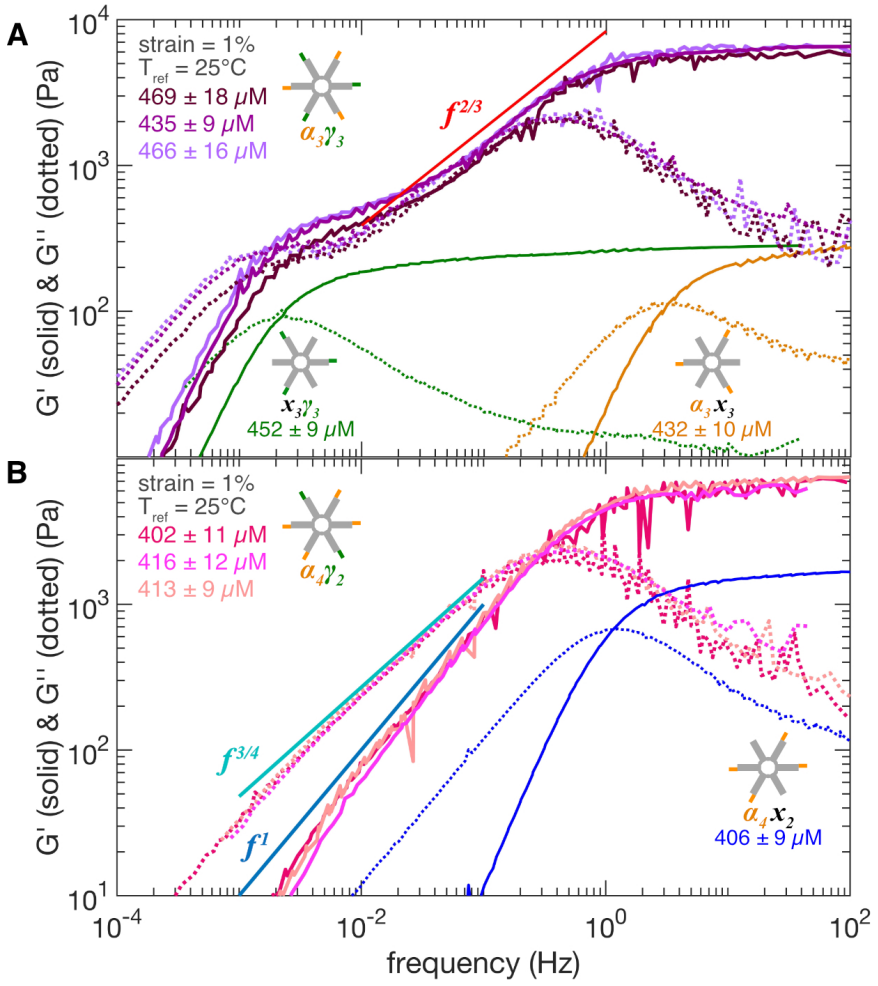

Figure 4.2: Plot of G' and G'' versus frequency of concentrated solutions of **(A)** $\alpha_3\gamma_3$ (purple hues) and **(B)** $\alpha_4\gamma_2$ (pink hues) NSs measured at 1% strain, added salt of 300 mM NaCl, and at a reference temperature of 25°C.

4.5 Discussion

Interestingly, G' and G'' of the $\alpha_3\gamma_3$ NS solution are everywhere significantly larger than the sum of the $x_3\gamma_3$ and α_3x_3 NS (Fig. 4.1A), even in the simple fluid regime $f < f_c(x_3\gamma_3)$ where α_3x_3 has minimal viscosity. This suggests that, by inextricably linking α and γ networks, the NS design enables the γ-bonded network to catalyze α-bond formation. If this cooperative behavior between the weak- and strong-bonded networks did not exist, then the sum of the two underlying network moduli would recover

the resulting viscoelastic response.

Another clue to the origin of the power-law scaling exponents is that for both heterotypic NS solutions the storage modulus plateaus to a value similar to that of the α_6 NS network (Fig. 4.1B), $G' \to G'_p \approx 6500$ Pa. This suggests that the power-law rheology of $\alpha_3\gamma_3$ and $\alpha_4\gamma_2$ NS solutions at intermediate frequencies reflects a changing network connectivity between the two sticky-end lifetimes: as frequency rises, stress-bearing chains of strong-bonds are constrained by an increasing number of weak-bonds, altering the moduli. We thus hypothesize that the increasing constraints, arising from increased junction valence, reduces the size of the elastic correlation length, $\xi(t)$, of the strong-bond network.

To build these insights into a model for G', we first propose that the weakly-bonded α-network can be modeled as a pervasive, uniform (*i.e.*, mean-field) background viscosity, η_{α_m}, that hinders collective relaxations of the strongly-bonded γ-network. We further propose that, in this Zimm-like scenario, relaxation can be modeled as a diffusion-limited process: fluctuating segments of the strong-bond network relieve stress by diffusing through the weak-bond network. A segment of size ξ will have an effective diffusion coefficient $D_\xi \propto k_\mathrm{B}T/(\eta_{\alpha_m}\xi)$, where k_B is the Boltzmann constant and T is the absolute temperature [1, 117], and, therefore, a characteristic diffusion time $t = \xi^2/D_\xi$. Solving for ξ yields

$$\xi \sim \left(\frac{k_\mathrm{B}T}{\eta_{\alpha_m}}t\right)^{1/3} \sim f^{-1/3}\,. \tag{4.1}$$

In other words, the time scale over which stress is dissipated determines the associated elastic correlation length of the strong-bond network (Fig. 4.3A). We note recent theoretical work on non-transiently bonded colloidal networks derived a similar relation for $\xi(f)$ as the one shown in 4.1; equation 8 in [115].

We sought evidence for this frequency-dependence of ξ from strain sweeps (Fig. 4.3B,

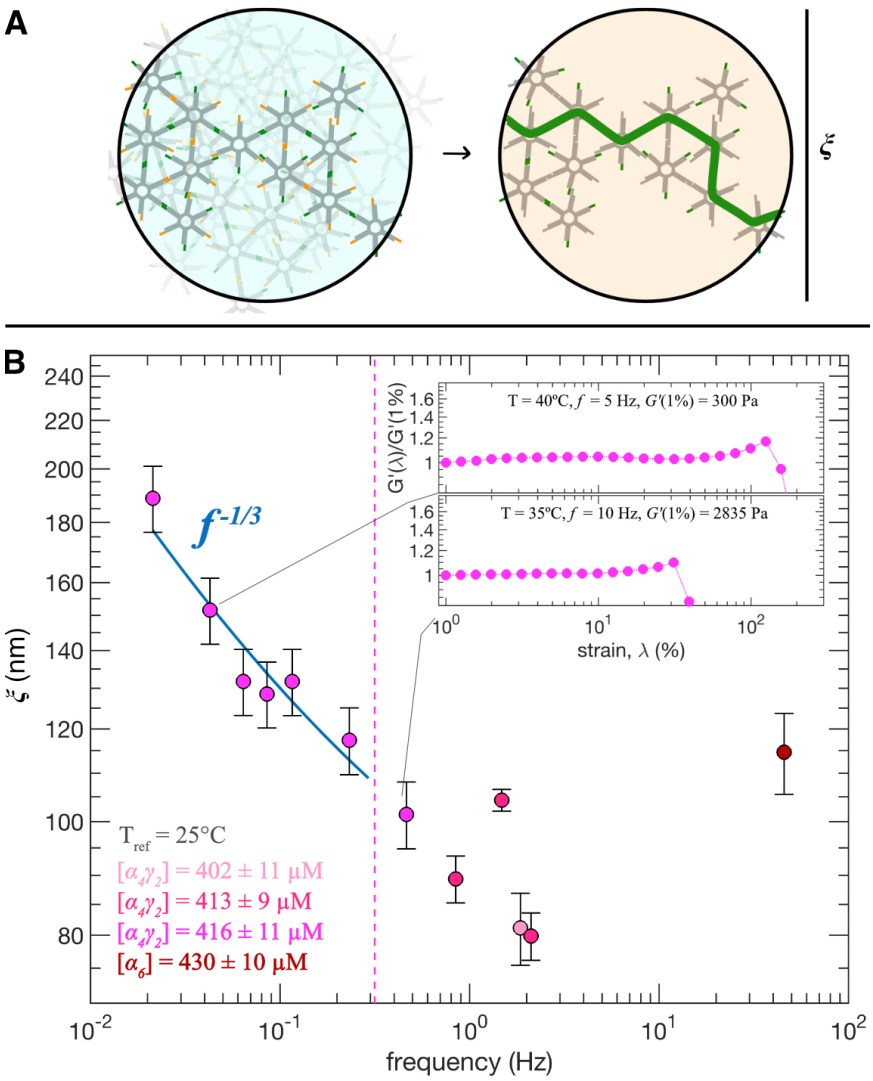

Figure 4.3: (**A**) Cartoon depiction of the mean-field model. Weak bonds (orange) are treated as a viscous solvent that determine the relaxation modes of the shortest/dominant stress-bearing chain (bold green path) in the strong-bond network within ξ. (**B**) Plot of ξ measured via strain sweep experiments versus (shifted) frequency at a reference temperature of $T_{\text{ref}} = 25°\text{C}$ for several $\alpha_4\gamma_2$ NSs and an α_6 NS. The vertical dashed lines denote the power-law regime for G' of the $\alpha_4\gamma_2$ NSs. The solid blue line is a non-linear least squares fit of $bf^{-1/3} + \xi_o$ between the vertical dashed lines. The reported frequencies are those of the raw strain sweeps multiplied by the corresponding temperature-dependent shift factors used to generate the master curves at $T_{\text{ref}} = 25°\text{C}$. (**B**, *inset*) Example yielding curves from which the yield stress were estimated. The legends in each inset plot contain the original Temperature and frequency at which the strain sweep was acquired. The legends also contain the value of the storage modulus at 1% strain.

inset & C.4). Specifically, we measured the yield strain, λ_y, and yield storage modulus, G'_y, to find the yield stress, $\sigma_y = G'_y\lambda_y$. We expect $\sigma_y \approx F_c/\xi^2$ [102], where F_c is the force required to break the strong NS-NS bond (estimated to be ≈ 10 pN based on the length of the γ-overhang sequence [104]). This implies

$$\sigma_y \approx F_c/\xi^2 \implies \xi(f) \approx \sqrt{\frac{F_c}{G'_y(f)\lambda_y(f)}}, \tag{4.2}$$

thus allowing direct estimate of ξ from the measurements of yielding. We note that F_c is expected to have a $\log(f)$-dependence. However, a strong $\log(f)$-dependence results in an increase in ξ, which is not consistent with the observed data (Fig. 4.3B and Fig. C.8). Thus, the $\log(f)$-dependence here is weak and can be ignored.

In $\alpha_3\gamma_3$ NS solutions, interestingly, we found ξ to be constant with frequency (Fig. C.8). We presume the effective frequency range of power-law rheology was too narrow (70 - 350 mHz) and the measurement precision too low ($\sim 20\%$) to meaningfully constrain the scaling of $\xi(f)$. In $\alpha_4\gamma_2$ NS solutions, however, the power-law rheology extended over a decade of frequency and $\xi(f)$ was in good agreement with Eq. 4.1 (Fig. 4.3B), validating the assumption that modes of relaxation accessible to the strong-bond network are Zimm-like.

The agreement of $\xi(f)$ with Eq. 4.1 also suggests that it is reasonable to treat the weak-bonded network as a pervasive, viscous solvent which resists the fluctuations of and, thus, affects the relaxation modes of the strong-bond network. We note a similar assumption was utilized in a recent theoretical and experimental work on transiently cross-linked metallo-supramolecular networks (e.g., unentangled polymer chains transiently bridged together by a small, linear linker) [26]. In particular, Ref. [26] derived a friction coefficient, ζ, for a polymer reptating in the presence of transient x-links, using a dynamic effective medium approach, and found it was dependent on both the concentration of

cross-links, c, and rate of cross-links dissociating off the polymer, k_d. The derived ζ was then used to correct their (separately derived) model predictions for the relaxation rate when the polymer is cross-linked only at its terminal ends, k_{eff}, and found that the correction to k_{eff} was in great agreement with experimental measurements as c increased from low to high. Thus, their agreement and ours here demonstrate the validity in assigning a constant viscosity to the weakly-interacting cross-links in solution when approximating how they affect the relaxation modes of the stress-bearing network.

To derive an expression for $G'(f)$ that reflects both how clusters smaller than ξ relax and how clusters larger than ξ deform, recall that the storage modulus of a $3d$ (percolated) network goes as $G' \sim K_\xi/\xi$, where K_ξ is the spring constant of the shortest stress-bearing chain within ξ [102, 106, 116]. For NS networks, it is expected [111] that $K_\xi \sim \xi^{-d_{\min}}$, where $d_{\min}$ is the fractal dimension of that shortest elastic chain within ξ. Combining this relationship with Eq. 4.1, yields

$$G' \sim \xi^{-(1+d_{\min})} \sim f^{(1+d_{\min})/3} \tag{4.3}$$

for $f_c(x_3\gamma_3) \ll f \ll f_c(\alpha_6)$.

The observed power-laws are indeed consistent with equation 4.3 based on what is known of the fractal dimension of stress-bearing chains in their respective strong-bond networks. In particular, the fractal dimension of a freely-jointed chain structure, the expected structure of the "valence-two" γ-network of $\alpha_4\gamma_2$, is $d_{\min} = 2$. Our model thus predicts $G' \sim f^1$, which is in great agreement with the observed $G'_{\alpha_4\gamma_2} \sim f^1$. Similarly, prior work on homotypic 3-armed NS networks indicate $d_{\min} = 1.2 \pm 0.1$, which would lead to a rheological exponent of $G' \sim f^{0.73\pm0.03}$. This is consistent with $G' \sim f^{2/3}$ found in $\alpha_3\gamma_3$ NSs, particularly within two standard errors of $G' \sim f^{0.73\pm0.03}$.[1] We emphasize

[1]Note, the exponent 2/3 predicts $d_{\min} = 1$, also within two standard errors of $d_{\min} = 1.2 \pm 0.1$

here once more that a large change to the power-law exponent and, hence, $d_{\min}$ between $\alpha_3\gamma_3$ and $\alpha_4\gamma_2$ was induced through only a slight change to the heterotypic NS design.[2]

To test the generality of our model, we consider a recent micro-rheological study of a critically-percolated equilibrium gel that measured $G' \sim G'' \sim f^{0.5}$ over two decades in frequency [31]. In this equilibrium gel of homotypic 4-armed NS, the viscosity opposing relaxations comes entirely from the pervading salt solution, but the value of $d_{\min} = 0.5 < 1$ inferred from Eq. 4.3 is physically unreasonable, suggesting that hydrodynamic interactions are fully screened. In the limit of no hydrodynamic interactions (*i.e.*, the Rouse limit or a freely draining network), stress-relaxation requires *all* connected NS in a ξ-sized cluster to move through the solvent. The effective diffusion coefficient in the mean field model then becomes $D_\xi \propto k_B T/\eta_{sol}\xi^{d_{\rm fr}}$, where $d_{\rm fr}$ is the mass fractal dimension of all connected NS in ξ and changes the denominator of the scaling exponents to:

$$\xi \sim f^{1/(2+d_{\rm fr})} \tag{4.4}$$

and

$$G' \sim f^{1+d_{\min}/(2+d_{\rm fr})}\,. \tag{4.5}$$

Estimates for $d_{\rm fr}$ in a critically percolated 4-arm NS network can be drawn from other studies. In particular, our own rheological study on a similar homotypic 4-arm NS network [27] found the *concentration* dependence of ξ is consistent with $3d$ percolation, which implies $d_{\rm fr} = 2.5$ [1]. Using this estimate $d_{\rm fr} = 2.5$, equation 4.5 says $G' \sim G'' \sim f^{0.5}$ implies $d_{\min} = 1.25$ for a percolated 4-arm NS network. We note independent numerical simulation of critically-percolated clusters of homotypic 4-arm NS found the average valence of NS in the cluster to be three [61], suggesting that $d_{\min}$ for 4-arm NS clusters may

[2]Recall that a structural change in a NS is achieved through a small change to the strand sequences self-assembling a NS.

indeed be similar to that of a 3-arm NS network $d_{\min} = 1.2$ [27]. However, independent and direct measurements of $d_{\min}$ are needed to confirm our prediction.

To further test the generality of our model on systems with known $d_{\rm fr}$ and $d_{\min}$, we adapt it to $2d$ and compare the predicted exponents to those measured in simulations of $2d$, critically isostatic networks [17, 97]. We first briefly discuss the model derivation in $2d$. The scaling of ξ with frequency in the Zimm (Eq. 4.1) and Rouse limits (Eq. 4.4) are the same in $2d$ as in $3d$. However, the storage modulus of a two-dimensional network is $G' \sim K_\xi$. Because each stress-bearing chain consists of $N_\xi \sim \xi^{d_{\min}}$ elastic elements in series, the spring constant $K_\xi \sim 1/N_\xi \sim \xi^{-d_{\min}}$. Therefore, in $2d$:

$$G'_{2d,Z} \sim \xi^{-d_{\min}} \sim f^{d_{\min}/3} \tag{4.6}$$

in the limit of full hydrodynamic coupling (*i.e.*, the Zimm limit) and

$$G'_{2d,R} \sim f^{d_{\min}/(2+d_{\rm fr})} \tag{4.7}$$

in the limit of full hydrodynamic screening (*i.e.*, the Rouse limit).

One set of simulations of a $2d$ triangular lattice at the isostatic threshold [118] found $d_{\min} = 1.80 \pm 0.03$ and $d_{\rm fr} = 1.86 \pm 0.02$. Plugging these values into Eqns. 4.6 and 4.7, yields $G' \sim f^{0.60\pm0.02}$ and $G' \sim f^{0.47\pm0.01}$ in the Zimm- and Rouse-limits, respectively. These values are in excellent agreement with other simulations on the same lattice, which measured $G' \sim f^{0.61}$ in the Zimm limit and $G' \sim f^{0.41}$ in the Rouse limit [17, 97].

More sophisticated theories, that invoke a dynamic effective medium [17] or perform a Lagrangian density of states analysis [86], predict these exponents with similar accuracy. Those theories, and simulations that test them [97], further provide the key insight that $G' \sim f^{F/\phi}$, where F is the critical rigidity exponent and ϕ is the critical relaxation

exponent of the isostatic transition. Therefore, based on our mean-field model, we can relate the ratio of those critical exponents to the structure of the isostatic network: $F/\phi = d_{\min}/3$ in the Zimm-limit and $F/\phi = d_{\min}/(2 + d_{\text{fr}})$ in the Rouse-limit.

4.6 Conclusion

In summary, we have leveraged the designability of DNA nanostars to study non-Maxwell power-law rheology in equilibrium gels. We demonstrated that small changes to the sticky-end sequences on a NS can lead to reproducible and large changes to the power-law exponents. We also presented a simple, mean-field model that predicts the observed scaling exponents and identifies two parameters that control the observed exponents: the fractal dimension of the dominant stress-bearing chain within an elastic correlation length, ξ, and the effective viscosity of non-stress-bearing interactions permeating the network. The model is further validated by strong agreement with observed power-law rheology in $(2d)$ isostatic networks of well-defined fractal dimensions, d_{fr} and $d_{\min}$. We therefore posit that the model here generally applies to all types of equilibrium gels when hydrodynamic interactions are important.

Chapter 5

Rheology of transient, heterotypic DNA nanostar networks

5.1 Preamble

The content of chapter 5 and appendix C is the result of a collaboration with Omar A. Saleh and Deborah K. Fygenson. The study here is a manuscript in preparation for submission to PRE.

5.2 Introduction

In the last chapter, we performed oscillatory rheology on NS networks that have both strong, long-lived NS-NS bonds and weak, short-lived ones (Fig. 4.1A). The resulting networks exhibited reproducible power-law rheology between the two sticky-end life-times (Fig. 4.1B). To explain the power-law exponents observed, a corresponding mean-field model was derived. The model relates the viscosity of the weak-bonded network to Zimm-like relaxation modes of the dominant strong-bonded stress-bearing path in the network. By relating the two, we found the following power-law relationships for the

elastic correlation length

$$\xi \sim \left(\frac{k_{\mathrm{B}}T}{\eta_{\alpha_m}}t\right)^{1/3} \sim f^{-1/3}. \tag{5.1}$$

and the storage modulus

$$G' \sim \xi^{-(1+d_{\min})} \sim f^{(1+d_{\min})/3} \tag{5.2}$$

where $d_{\min}$ is the fractal dimension of the dominant, strong-bonded stress-bearing path.

To expand on the work described in chapter 4, we now investigate the microscopic parameters controlling power-law rheology in heterotypic NS solutions. In particular, in this chapter, we explore how salt affects the viscoelastic spectra of $\alpha_3\gamma_3$ NSs and we will investigate the rheology of several other types of heterotypic NSs (Fig. 5.1B). The other heterotypic NS designs will test how power-law rheology is affected by: (*i*) slightly decreasing the binding strength of the strong sticky-end (e.g., $\alpha_3\beta_3$ NSs) (*ii*) using a NS that has 2 weak sticky-ends and 4 strong ones (e.g., $\alpha_2\gamma_4$ NSs), and (*iii*) changing the overall valence of the NS from six to five, with a weak to strong sticky-end ratio of 3 to 2 (e.g., $\alpha_3\gamma_2$ NSs). All NS-types, except $\alpha_2\gamma_4$ NSs, make networks with reproducible power-law rheology between the two sticky-end lifetimes. We use the mean-field model derived in Chapter 4 to explain the observed power-law exponents and we will also show that a two-mode Maxwell model reproduces the viscoelastic spectra of $\alpha_2\gamma_4$ NSs. In addition to discussion of how power-law rheology changes in the various heterotypic NS solutions, we relate the viscoelastic properties observed in both their terminal fluid and elastic regimes to the underlying NS sticky-end lifetimes and connectivity. We will generally show here that the sticky-end lifetime and valence are important dials in tuning the overall viscoelastic spectra of equilibrium gels.

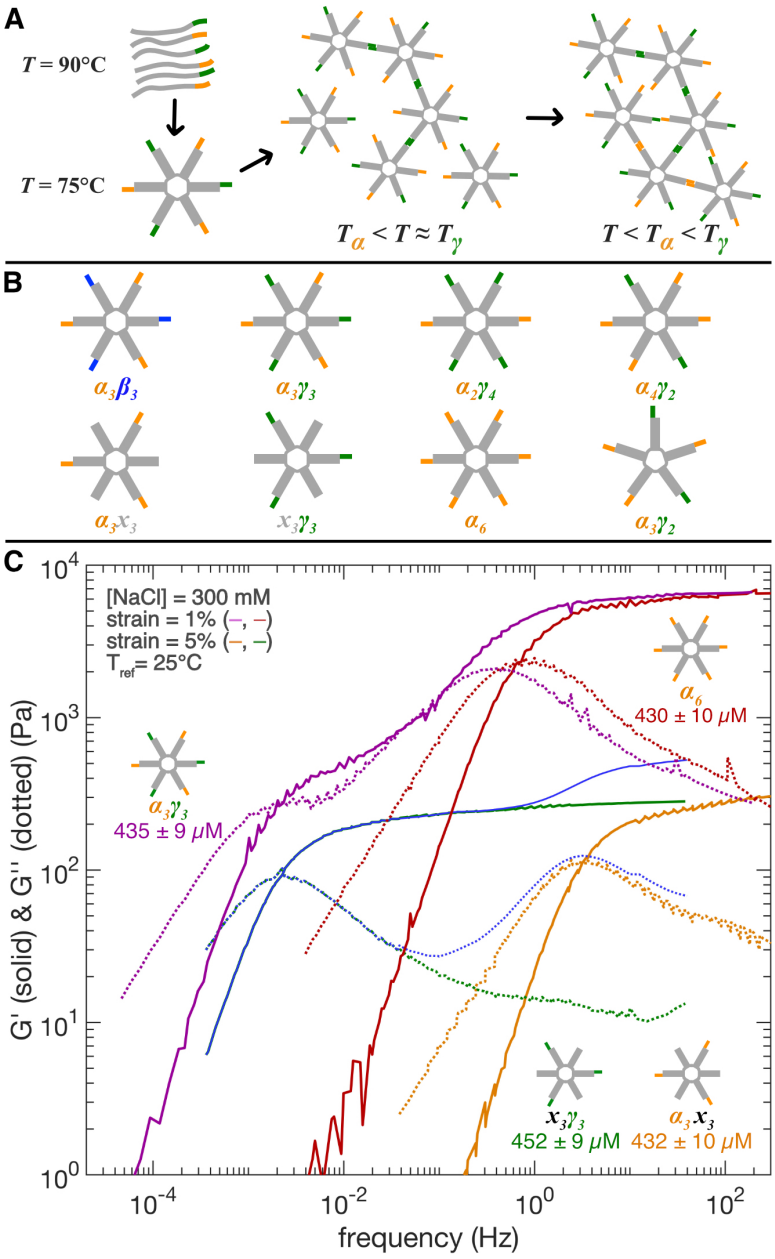

Figure 5.1: **(A)** Schematic of NS formation and network assembly as temperature, T, is lowered. T_α and T_γ denote the melting temperature of the α and γ sticky-ends, respectively. **(B)** Different NS types used in this study (see Table S1 for sequences). The binding strength hierarchy is the following: $T_\alpha < T_\beta < T_\gamma$, where T_i is the melting temperature of sticky-end i. **(C)** Plot of G' and G'' versus frequency of concentrated solutions of α_3x_3 (orange), $x_3\gamma_3$ (green), α_6 (red) and $\alpha_3\gamma_3$ (purple) NSs at an added salt of 300 mM NaCl. The sum of the storage and loss moduli of α_3x_3 and $x_3\gamma_3$ networks are shown in blue.

5.3 NS preparation and rheology protocol

A brief description of the materials and methods is listed here. A more detailed description of each material and method is found in the appendix of this thesis (Appendix C).

To make the heterotypic NS with $z = n+m$ arms, e.g., "$a_n b_m$" NS, we designed z self-complementary ssDNA oligos where n and m of the oligos have a- or b-type sticky-ends, respectively (see Appendix C1). The same sequences for the z-armed $a_n b_m$ heterotypic NS were used for the z-arm homotypic NSs $x_n b_m$ and $a_n x_m$, with some slight design changes. In particular, the n or m oligos on the $x_n b_m$ or $a_n x_m$ NS have their respective a- or b-type sticky-end removed.

Solutions of either homotypic or heterotypic z-arm NSs were prepared by mixing together the corresponding z complementary ssDNA oligos in stoichiometric amounts (Fig. 5.1A). For all NS types, the newly mixed solution of oligos required dehydration and subsequent rehydration in 100 μL of a Tris buffer (40 mM Tris, 11.5 mM HCl, 1 mM EDTA) at various salt concentrations. The re-suspended NS solution was then slowly annealed from $T = 90°C$ to $T \approx 20°C$ over ≈5 hours to ensure proper NS formation. The concentration of the annealed NS solution was estimated from UV-Vis absorbance measurements at a 260 nm wavelength on 100-fold diluted aliquots of solution. The resulting concentrations of NSs made were between 400 and 470 μM.

After concentration measurements, annealed NS solutions were carefully shoveled out of their tubes using a slant cut pipette tip onto a strain- and temperature-controlled bulk rheometer for viscoelasticity measurements. We first performed oscillatory rheology measurements in the linear viscoelastic regime of the solution ($\approx 1\%$ strain) to measure the storage G' and loss G'' moduli over a range of frequencies at many different temperatures. All $G'(f)$ and $G''(f)$ data shown are master curves constructed using time-temperature

superposition, as detailed in Appendix B.6.2, at the reference temperatures listed in the respective plots. We then measured G' and G'' over a range over strains, $1\% \leq \lambda \leq 300\%$ at many different temperatures and applied frequencies to investigate yielding behavior.

5.4 Results

5.4.1 Frequency sweeps

The linear frequency-dependent storage, G', and loss, G'', moduli of concentrated solutions of all homotypic NSs exhibited a Maxwell-like response (Fig. 5.1B). Namely, these solutions flowed like a viscous fluid at low shearing frequencies until a characteristic frequency $f_c \equiv 1/\tau_c$ occurring at $G' = G''$; e.g., $G'(f) \sim f^2 < G''(f) \sim f^1$ for $f < f_c$. They then transitioned to a high-frequency elastic solid at $f > f_c$ with $G'(f) \approx G'_p > G''(f)$. We note that for $\alpha_3 x_3$ and $x_3\gamma_3$ NSs, we measured $\tau_c(x_3\gamma_3) \approx 10^3 \tau_c(\alpha_3 x_3)$ and $G'_p(x_3\gamma_3) \approx G'_p(\alpha_3 x_3)$ across all added salt concentrations.

When increasing the valence of alpha bonds from 3 to 6 on the homotypic NSs here, we found $\tau_c(\alpha_6) \approx 5\tau_c(\alpha_3 x_3)$ and observed a 20-fold increase in the elastic plateau modulus, G'_p. Similar differences were observed in chapter 3 between a 6 arm NS and a purely 3 arm NS. This indicates the blunted arms on the homotypic NSs here are rheologically inert.

For all homotypic NSs, we observed the temperature dependence of τ_c to be Arrhenius-like (Fig. 5.7). In the $\alpha_3 x_3$ and α_6 NS solutions, we find the fitted Arrhenius activation energy, E_a, to be $\approx 90\%$ the estimated enthalpy, ΔH, of the α sticky-end sequence (Table C.1). Similarly, in the $x_3\gamma_3$ NS solutions, we find $E_a \approx 0.8\Delta H$ (Table C.1). Lastly, across all salt concentrations used in the $\alpha_3 x_3$ and $x_3\gamma_3$ NS solutions, the Arrhenius temperature-dependence of the relaxation time persisted (Fig. C.3) and E_a remained approximately

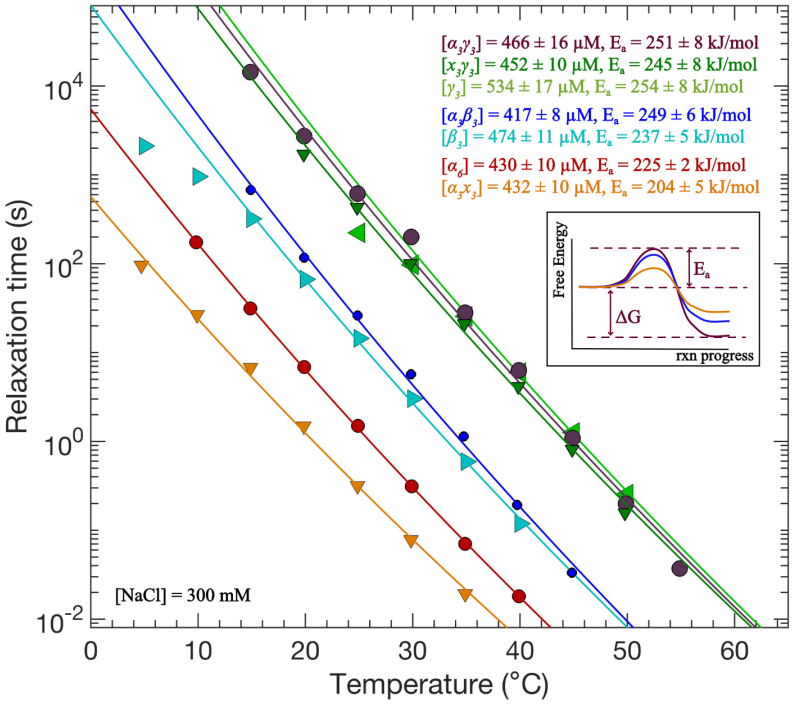

Figure 5.2: Terminal liquid relaxation time vs temperature for $\alpha_3 x_3$ (orange $\bigtriangledown$), α_6 (dark red $\bigcirc$), β_3 (aqua $\triangleright$), $\alpha_3\beta_3$ (blue $\bigcirc$), γ_3 (light green $\triangleleft$), $x_3\gamma_3$ (dark green $\bigtriangledown$), and $\alpha_3\gamma_3$ (dark purple $\bigcirc$). The NS concentration and activation energy measured from Arrhenius fitting, E_a, are listed in the legend of the plot. **Inset**, Qualitative sketch of the free energy vs reaction progress for NS network relaxation. E_a is the activation energy required to get to the transition state (e.g., fluid flow). ΔG is the free energy of the sticky-end interaction.

the same (Table C.1).

Next, we measured the linear $G'(f)$ and $G''(f)$ of concentrated $\alpha_3\gamma_3$ NS solutions at added salt concentrations of 50, 150, and 300 mM NaCl (Fig. 5.3). The $\alpha_3\gamma_3$ NS solution exhibited the same viscoelastic response across all salt concentrations, which can be seen after normalizing $G'(f)$ and $G''(f)$ curves (Fig. 5.3B). The generic shape of the viscoelastic spectra was as follows: (i) simple fluid flow at $f < f_{liq}(\alpha_3\gamma_3) \equiv 1/\tau_{liq}(\alpha_3\gamma_3)$, with roughly $G' \sim f^2$ and $G'' \sim f^1$ (ii) between $f_{liq}(\alpha_3\gamma_3) < f < f_c(\alpha_6)$, solutions had a small period of elastic plateau near $f_{liq}(\alpha_3\gamma_3)$ and then a larger period of $G' \approx G'' \sim f^{2/3}$ until $f_c(\alpha_6)$ (iii) at $f > f_c(\alpha_6)$, there was an elastic-like response with $G' \to G'_p \approx$ 6000-7000 Pa and $G'' \sim f^{-3/5}$. Increasing salt only shifted the spectra to lower frequencies

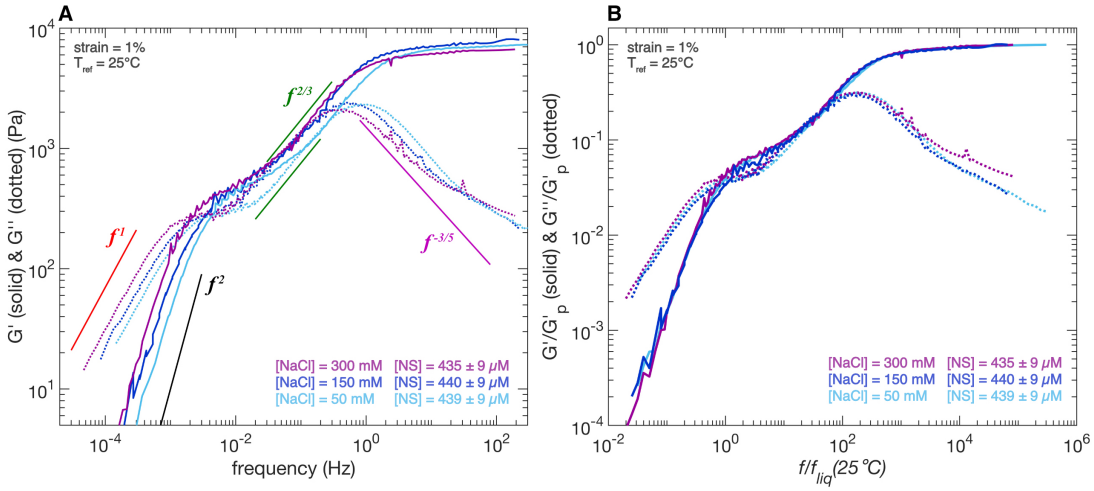

Figure 5.3: **(A)** Plot of the linear storage, G', and loss, G'', moduli versus frequency of $\alpha_3\gamma_3$ NS solutions at an added salt of 50, 150 and 300 mM NaCl and reference temperature of 25°C. **(B)** Normalized plots of G' and G'' vs frequency, where the moduli are normalized by the plateau modulus, G'_p, and the frequency is normalized by the liquid-like crossover frequency at 25°C, $f_{liq}(25°C)$.

(Fig. 5.3A).

We note we define $\tau_{liq}(\alpha_3\gamma_3)$ as the "liquid-like" time-scale in the $\alpha_3\gamma_3$ NS solutions, which demarcates the frequency below which the material flows like a simple liquid and occurs at the first instance of $G' = G''$ in the spectra. For all salt conditions, we found $\tau_{liq}(\alpha_3\gamma_3)$ to be Arrhenius-like with temperature (Fig. C.3) and found the fitted E_a to be roughly equal to the $x_3\gamma_3$ NS solution (Table C.1).

Next, we tested the effect of changing the strong sticky-end lifetime on heterotypic NS rheology (e.g., γ to β, Fig. 5.4). At low frequencies, $\alpha_3\beta_3$ solutions flow like a viscous liquid, with roughly $G' \sim f^2$ and $G'' \sim f^1$ until approximately $\tau_c(\beta_3)$ (Fig. 5.2). Then, for $f_c(\beta_3) < f < f_c(\alpha_6)$, power-law rheology occurred immediately with $G' \sim f^{3/4}$ and $G'' \sim f^{2/3}$ (Fig. 5.4). At $f > f_c(\alpha_6)$, the $\alpha_3\beta_3$ NS solution behaved elastically, with $G'' \sim f^{-3/5}$ and $G'(f) \to G'_p$ nearly equal to the α_6 solutions.

We also investigated how the rheology of a 6 arm NS solution is affected by changing the valence ratio between strong and weak bonds; e.g., $\alpha_4\gamma_2$ and $\alpha_2\gamma_4$ NSs (Fig. 5.5).

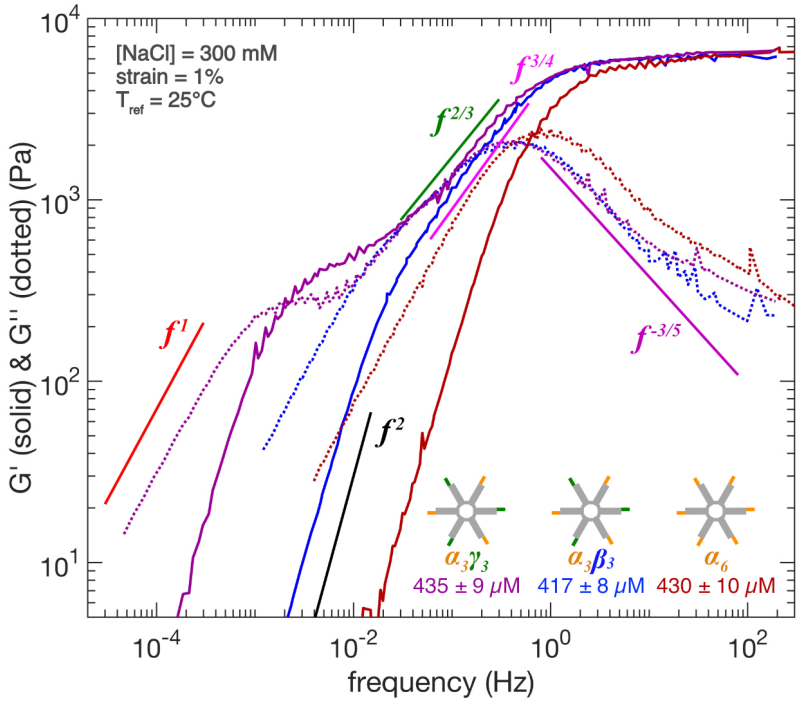

Figure 5.4: Plot of the linear storage, G', and loss, G'', moduli versus frequency of concentrated solutions of α_6 (dark red), $\alpha_3\beta_3$ (blue), and $\alpha_3\gamma_3$ (purple) at an added salt of 300 mM NaCl and reference temperature of 25°C.

Similar to other heterotypic NSs, the $\alpha_4\gamma_2$ and $\alpha_2\gamma_4$ networks were fluid-like at low frequencies. Interestingly, we found the characteristic frequency of liquid response, $f_{liq} = 1/\tau_{liq}$, increased when the γ valence ratio increased. This can be quantitatively seen in the terminal crossover of $G' = G''$ in $\alpha_2\gamma_4$ occurring at a frequency well into the liquid-like regime of $\alpha_4\gamma_2$ NS solutions (Fig. 5.5). At frequencies above $1/\tau_{liq}$, (i) the $\alpha_2\gamma_4$ NS transitioned between two clear elastic plateaus, with the first elastic plateau and τ_{liq} being equal to those of a γ_4 NS solution (Fig. C.2) and (ii) the $\alpha_4\gamma_2$ showed power-law rheology with $G' \sim f^1$ and $G'' \sim f^{3/4}$ persisting over almost 2 decades of frequencies. Lastly, the high-frequency rheology of both $\alpha_2\gamma_4$ and $\alpha_4\gamma_2$ NSs exhibited similar properties. In particular, they both had $G'_p \approx 6500$ Pa and $G'' \sim f^{-3/5}$ at $f > f_c(\alpha_6)$, which is also seen in the $\alpha_3\beta_3$, $\alpha_3\gamma_3$, and α_6 NS solutions.

Finally, we tested how G' and G'' of heterotypic NS solutions are affected by changing

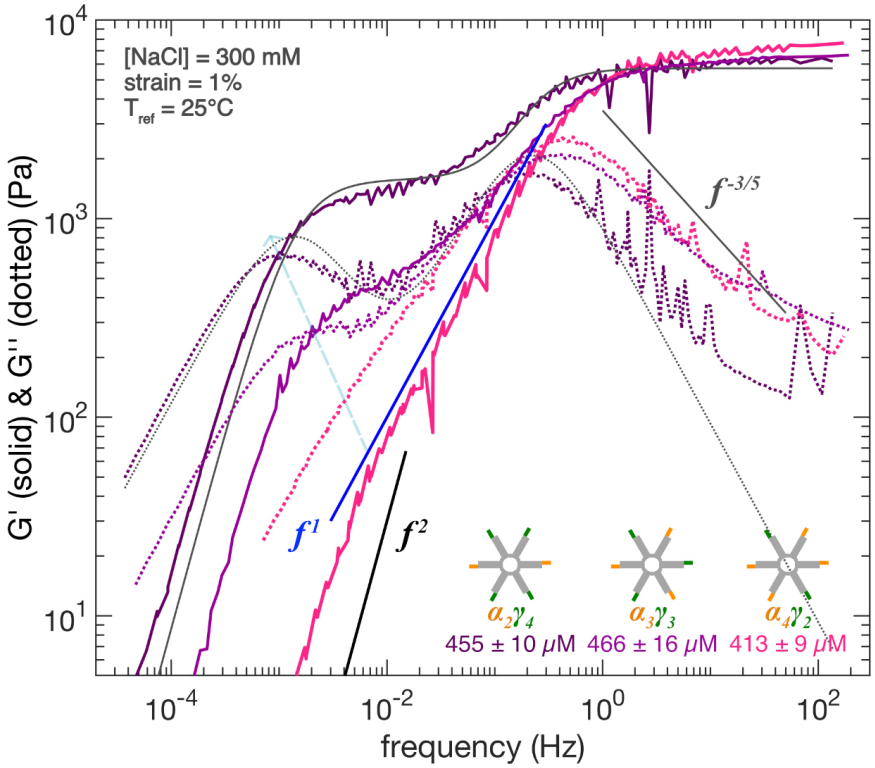

Figure 5.5: Plot of the storage, G', versus frequency of concentrated solutions of $\alpha_2\gamma_4$ (dark purple), $\alpha_3\gamma_3$ (magenta), and $\alpha_4\gamma_2$ (pink) NSs at an added salt of 300 mM NaCl. The solid and dotted light grey lines are non-linear least square fits of a two-mode Maxwell material to $\alpha_2\gamma_4$ G' and G'', respectively. The minimization process took into account both G' and G'' when finding the parameters for the fitted function (e.g., the 4-parameters of the fit were found by minimizing both model functions and data sets simultaneously). The light blue arrow is a guide for the eye showing the decrease in f_{liq} as the valence in the γ-bond network increases.

the total valence from 6 to 5; e.g., $\alpha_4\gamma_2$ to $\alpha_3\gamma_2$ NSs (Fig. 5.6A). Upon going from $\alpha_4\gamma_2$ NSs to $\alpha_3\gamma_2$ NSs, the moduli lowered in magnitude ($G'_p(\alpha_3\gamma_2) \approx 3000$ Pa), the power-law region compressed in frequency space, and the two characteristic frequencies demarcating fluid and elastic regimes shifted to higher frequencies. The liquid- and solid-like characteristic frequencies increased $\approx$ 6x and 1.3x, respectively (see Fig. C.3 for 6-fold change in liquid-like relaxation time). The incommensurate increases in the two frequencies (likely) resulted in changing the G' power-law rheology from $G' \sim f^1$ to $G' \sim f^{11/10}$ and limiting $G'' \sim f^{3/4}$ to a very small frequency regime. Despite the power-

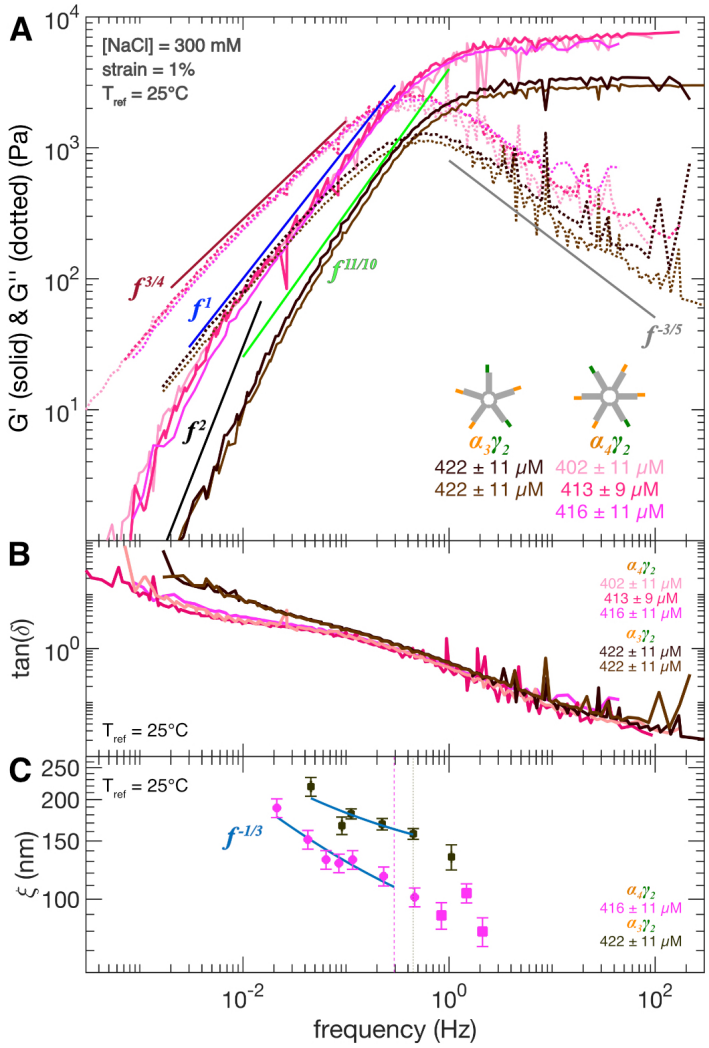

Figure 5.6: Plot of **(A)** G' and G'', **(B)** $\tan(\delta)$, and **(C)** the elastic correlation length ξ versus frequency of concentrated solutions of $\alpha_3\gamma_2$ (brown hues) and $\alpha_4\gamma_2$ (pink hues) NSs at an added salt of 300 mM NaCl. In **B**, there is a plateau in $\tan(\delta)$ that roughly corresponds to the region of non-Maxwell power-law scalings observed in **A**. In **C**, the frequencies of the data points reported were multiplied by the TTS shift factors used to make the $G'(f)$ and $G''(f)$ master curves at $T_{\text{ref}} = 25°\text{C}$. The dashed line in **C** denotes the rough location of $G' = G''$ in **A**. The blue line in **C** is a non-linear fit of $\xi = bf^{-1/3} + \xi_o$ to the respective data set.

law exponents behaving slightly differently in the intermediate regime, we still observed $G'' \sim f^{-3/5}$ in the elastic regime of $\alpha_3\gamma_2$.

5.4.2 Strain sweeps

We measured the strain behavior of the storage modulus, G', of concentrated solutions of homotypic NSs in their elastic response regime (Fig. 5.7 and Fig. C.4). For all solutions, the homotypic NSs were linear up to roughly 10-20% strain. After the linear regime, $\alpha_3 x_3$, $\alpha_4 x_2$, and $x_3\gamma_3$ entered a period of strain hardening until yielding at $\approx 200\%$ and 80% strain for valence 3 and valence 4 networks, respectively. Whereas, for the α_6 NSs, the solution immediately yielded after 10-20% strain.

Next, we measured the strain behavior of G' in concentrated solutions of heterotypic NSs during conditions when they exhibited non-Maxwell power-law rheology and were elastic-like (Fig. 5.7B-D and Fig. C.4). For all conditions (e.g. temperatures and frequencies), the linear regime of heterotypic NSs lasted until roughly 10-20% strain, similar to the homotypic ones. After the linear regime, heterotypic NS solutions either exhibited strain hardening or immediately yielded. In particular, when doing strain sweeps at temperatures and frequencies when most of the α bonds have relaxed, strain stiffening occurred and mimicked that of homotypic ones with valence similar to the strong-bond network valence. On the other hand, at temperatures and frequencies when both the α- and γ-bonds are stable, the 6 arm heterotypic NS solutions broke immediately after its linear regime, much like homotypic α_6 NSs.

5.5 Discussion

5.5.1 Single NS-NS bond dissociation determines simple liquid flow

Our oscillatory rheology experiments here measure characteristic time-scales of liquid response for both homotypic, τ_c, and heterotypic NSs, τ_{liq} (see caption of Fig. C.3 for

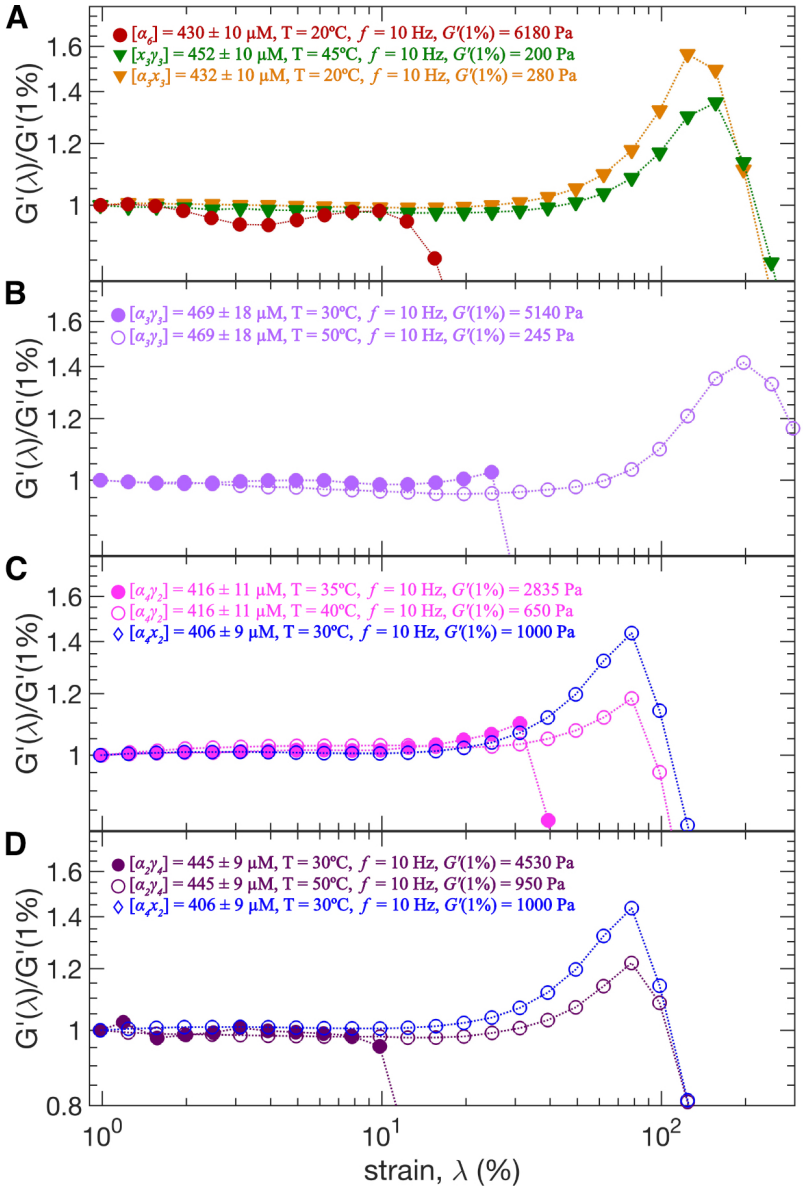

Figure 5.7: Normalized storage modulus versus strain for **(A)** $\alpha_3 x_3$ (orange), $x_3\gamma_3$ (green), α_6 (red), **(B)** $\alpha_3\gamma_3$ (light purple), **(C)** $\alpha_4\gamma_2$ (pink), $\alpha_4 x_2$, and **(D)** $\alpha_2\gamma_4$ (dark purple), and $\alpha_4 x_2$ (blue). The NS concentration, temperature, frequency, and storage modulus at 1% strain, $G'(1\%)$, are listed in the legends of each plot.

$\tau_{liq}(\alpha_3\beta_3)$ and $\tau_{liq}(\alpha_4\gamma_2)$ estimate). We generally find τ_{liq} of a heterotypic NS, with a strong-bond valence of z_γ, to be similar in magnitude to τ_c of a strong-bond homotypic NS of valence z_γ; e.g., $\tau_{liq}(\alpha_3\gamma_3) \approx \tau_c(x_3\gamma_3) \approx \tau_c(\gamma_3)$ (Fig. 5.1 & C.2). This suggests that (i) the dissociation of strong NS-NS bonds (e.g., β or γ-bonds) in the heterotypic

NSs, and not the weak one, determines the liquid-like time-scale and (*ii*) blunted or dissociated NS arms are rheologically inert.

To find more evidence supporting the interpretation that the strong NS-NS bonds sets τ_{liq} in heterotypic NS solutions, we compare plots of τ_{liq} and τ_c of the corresponding control, homotypic NS versus temperature (Fig. 5.2 & C.3). We find both τ_{liq} of heterotypic and τ_c of the associated control homotypic NS to be Arrhenius-like with temperature, T, with similar activation energies for fluid flow, E_a, roughly equal to the estimated enthalpy of a single strong NS-NS bond (see Fig. 5.2 & Table C.1). This lends strong support to the notion that the thermal stability of a single strong NS-NS bond in heterotypic NS networks set the energy barrier for simple fluid flow.

It is interesting, though, that the energy barrier for fluid flow is similar to that of a single NS-NS bond. This means a NS does not need to fully dissociate from the network in order for the solution to flow. Instead, fluid flow is likely explained though bond rearrangements in the network [35]. In this picture, a transient network, in its initial instantaneously bonded network state, relaxes to a transitional flowing state when two bound NS arms dissociate their sticky-ends and, then, those two unbound NS arms eventually find new binding partners (Fig. 5.2, inset).

The aforementioned picture of a single NS-NS bonds controlling network relaxation means the entropy difference between initial and final states also determines the stability of the bound state. Indeed, the predicted $|\Delta S_{NS-NS}|$ increases monotonically over $\alpha \rightarrow \beta \rightarrow \gamma$ (Table C.1), consistent with the increase in magnitude of τ over those sticky-end types. We specifically find that τ increases about 10-fold between $\alpha \rightarrow \beta$ and $\beta \rightarrow \gamma$, despite only slight sequence changes and, hence, small increases between $|\Delta S|$ of each sticky-end (e.g., $|\Delta S_\beta| \approx 1.11|\Delta S_\alpha|$ and $|\Delta S_\gamma| \approx 1.07|\Delta S_\beta|$). We note that even though $\Delta S_\beta \approx 1.1\Delta S_\alpha < 0$, because $\tau \sim \exp(-\Delta S_{NS-NS}/R)$ where $R \equiv$ molar gas constant, the change in τ is predicted to be roughly of order $(\exp(1.1\Delta S_\alpha/R)/\exp(\Delta_\alpha/R)) \approx 10^4$.

Although an overestimate in the increase we observe, the exponential dependence of τ on ΔS_{NS-NS} illustrates how large increases in τ can occur through slight perturbations to the sticky-end sequence.

Further evidence supporting the notion that the entropic barrier to forming a single NS-NS bond sets τ can be seen in τ_{liq} increasing with γ-bond valence, despite E_a being roughly constant (Fig. C.5). In particular, τ_{liq} has a linear dependence on the valence of the gamma-bond, z_γ, on a heterotypic NS (Fig. C.5). We note τ_c also increased linearly with z_α on the homotypic α-bond NSs of Chapter 3 (Fig. C.5, inset). The observed linear relationship between τ and z can be qualitatively understood within the entropy framework mentioned in the previous paragraph. In particular, since the entropic barrier for relaxation is related to NS arm rearrangement, then a free/unbound arm will have its number of configurations limited by the number of other *bound* arms emanating from the same NS.[1] The number of configurations for the free arm is then related to the solid angle over which it can subtend, $\approx 4\pi/z$. This leads to $\Delta S_z \sim \ln(4\pi/z) \sim -\ln(z)$ implying $\tau \sim \exp(-\Delta S_z) \sim z$, consistent with the observations seen in Figure C.5. This also further demonstrates that the strong sticky-end valence on a heterotypic NS largely determines the magnitude of τ_{liq}.

The last piece of evidence supporting single sticky-end control over τ is that we also found a linear relationship between added salt and $\tau_c(\alpha_3 x_3)$, $\tau_c(x_3\gamma_3)$, and $\tau_{liq}(\alpha_3\gamma_3)$ (Fig. C.6). This is in fact quite consistent with experiments done by SantaLucia showing the salt effect on DNA binding entropy is $\Delta S_b \sim -\ln([\text{salt}])$ [59]. Arrhenius dependence of the NS-NS binding time-scale again tells us $\tau \sim \exp(\Delta G_{NS-NS}/(RT)) \sim[\text{salt}]$.

Putting together all of the relations we've found for the relaxation time, we find the following for NS networks: $\tau \sim z\cdot[\text{salt}]\cdot\exp(\Delta G_{NS-NS}/(RT))$.

[1]Recall the similarity in $\tau_{liq}(\alpha_3\gamma_3) \approx \tau_c(x_3\gamma_3)$ and $\tau_{liq}(\alpha_3\beta_3) \approx \tau_c(\beta_3)$ suggests the blunted/non-sticky arms are rheologically inert. This means the blunted/non-sticky arms do not significantly add to the entropic barrier for network flow.

5.5.2 Intermediate power-law rheology determined by strong-bond valence

The solutions made from heterotypic NSs exhibit viscoelastic responses quite different from that of homotypic NSs. The homotypic NS solutions only have one mode of relaxation, which results in a direct transition from low-frequency fluid into a high-frequency elastic solid (e.g., a Maxwell material). Whereas, the heterotypic NSs transition through many modes of relaxation between simple fluid and elastic solid. Over those time-scales, the solution then displays power-law rheology.

Four of the heterotypic NS types showed power-law rheology indicative of multi-modal stress-relaxation between the weak- and strong-bond lifetimes [1,3,25,86,119–121]. Here, we interpret the many modes result from the weak-bonds continuously constraining the strong-bond network and, thus, reducing the elastic correlation length, ξ, in the strong-bond network. In Chapter 4, we showed that the available relaxation modes of the strong-bond network within ξ are directly related to the viscosity supplied by the weak-bonds. In particular, we make the assumption that the weak-bonded network is a uniform, background viscous fluid resisting the diffusion-limited relaxations of the strong-bonded network. Given the intrinsically coupled nature of the weak- and strong-bonds on a single NS, we also make the assumption that the (weak-bonded) viscous solvent is coupled to the volume set by ξ (e.g., the Zimm-limit). In this Zimm-limit, we find the power-law relation for $\xi(f)$ (equation 4.1).

We sought evidence for the frequency-dependence of the elastic correlation length, ξ, from strain sweep measurements (Fig. 5.7 & C.4). Specifically, we measured the yield strain, λ_y, and yield storage modulus, G'_y, across all accessible temperatures and frequencies to calculate the yield stress ($\sigma_y = G'_y\lambda_y$) and, from σ_y, across all accessible

temperatures and frequencies we get

$$\sigma_y = F_c/\xi^2 \implies \xi(f) = \sqrt{\frac{F_c}{G'_y(f)\lambda_y(f)}}, \tag{5.3}$$

where F_c is the "critical force" required to break the strong NS-NS bond (estimated to be ≈ 10 pN based on the γ-overhang sequence [104]).[2] In $\alpha_3\gamma_3$ and $\alpha_3\beta_3$ NS solutions, the effective frequency range of power-law rheology was too narrow (70 - 350 mHz) and the measurement precision too low ($\sim 20\%$) to meaningfully constrain the scaling of $\xi(f)$ (Fig. C.8). In $\alpha_3\gamma_2$ and $\alpha_4\gamma_2$ NS solutions, however, the power-law rheology extended over a decade of frequency and was in good agreement with Eq. 4.1 (Fig. 5.6C), validating the assumption that the accessible relaxation modes of the strong-bond network are Zimm-like.

From the scaling of ξ in the Zimm-limit, the scaling exponent scaling G' with f is found to be directly related to d_{min} (see Chapter 4 for derivation). We use the relation to make predictions for d_{min} in the networks displaying power-law rheology between the weak- and strong-bond lifetimes using equation 4.3. We observe that the strong-bond valence of the network is the dominant modulator of the power-law exponent and, thus, of d_{min}. For instance, the expected structure of a valence-two NS is a freely-jointed chain with $d_{min} = 2$, leading to $G' \sim f^1$. This is in great agreement with the observed $G'_{\alpha_3\gamma_2} \sim f^{11/10}$ and $G'_{\alpha_4\gamma_2} \sim f^1$ where the strong-bonded network is of valence-two. Similarly, prior work on homotypic 3-armed NS networks indicate $d_{\min} = 1.2 \pm 0.1$. Our model thus predicts such networks have $G' \sim f^{0.73\pm0.03}$, consistent with both $G'_{\alpha_3\beta_3} \sim f^{3/4}$ and $G'(\alpha_3\gamma_3) \sim f^{2/3}$ where the strong-bonded network valence is three. Further, we

[2]It is worth pointing out that the assumption of yielding occurring after breaking one NS-NS bond is predicated from our previous discussion regarding how dissociation of a single NS-NS bond results in fluid flow. Further, recall in chapter 4 we mentioned that F_c is expected to have a $\log(f)$-dependence. However, a strong $\log(f)$-dependence results in an increase in ξ, which is not consistent with the observed data. Thus, the $\log(f)$-dependence here is weak and can be ignored.

emphasize once more that a significant change to the power-law exponent and, hence, $d_{\min}$ between heterotypic NS networks was induced through only a slight change to the strong-bond valence of the NS.

In $\alpha_3\gamma_3$ NSs, it is interesting that the power-law scaling $G' \sim G'' \sim f^{2/3}$ persists as salt changes in solution (Fig. 5.3) This robustness in the observed 2/3 power-law against salt changes suggests that the exponent is real and reflects an underlying multi-modal stress-relaxation of a dominant elastic chain. The multi-mode relaxation is indeed further supported by finding that $\alpha_3\gamma_3$ NSs are not well described by a two-mode Maxwell viscoelastic spectra (Fig. C.6).

We note there is another way to measure the power-law exponent q scaling G' and G'' with frequency for $\alpha_3\gamma_3$ NS through the tangent of the phase shift between G' and G'', $\tan(\delta)$. In particular, in the case when both $G' \sim G'' \sim f^q$, with $0 < q < 1$, over the *same frequency region*, then the Kramers-Kronig relation says $\tan(\delta) = \tan(q\pi/2)$ over the power-law regime [113]. However, in all $\alpha_3\gamma_3$ NSs solutions and for all salt conditions, $\tan(\delta)$ never approached $\tan(\pi/3) \approx 1.7$ (Fig. C.6), presumably due to the small overlapping region of power-law scaling. We find that a generalized numerical Kramers-Kronig approximation for $\tan(\delta)$ [122] does agree well with the $\alpha_3\gamma_3$ data across all frequencies (Fig. C.7).

5.5.3 Two-mode Maxwell rheology recovery

In contrast to the other heterotypic NS networks, we find the $\alpha_2\gamma_4$ goes through only two modes of relaxation when transitioning from low-frequency liquid to high-frequency solid (Fig. 5.5). In particular, we observe that the first and second elastic plateau are consistent with measurements of the underlying valence 4 and 6 networks (Fig. C.2). We indeed further find that $G'(f)$ and $G''(f)$ is fit quite well by a sum of two Maxwell modes

(Fig. 5.5), with the fitted $\tau_{c,i}$ and $G'_{p,i}$ consistent with the homotypic valence 4 and 6 networks. Thus, here, we interpret the α-bonds do not impart a large enough viscosity capable of affecting the relaxation modes in the valence 4 γ-bond network. Thus, power-law rheology in heterotypic NS solutions can be turned off when the strong-bond network is sufficiently more stable and rigid compared to the weak-bonded one.

5.5.4 High-frequency G' and strain sweeps of 5 and 6 arm NSs consistent with isostaticity

The high-frequency storage modulus of all homotypic and heterotypic NSs plateau to a constant value, indicative of an elastic solid at those frequencies. In particular, we observed that all valence 6 NS networks, each with roughly the same NS concentration, plateau to roughly the same value, $G'_p \approx 6500$ Pa (Fig. C.2). Further, for similarly concentrated valence 3 homotypic and valence 5 heterotypic NS, we respectively found $G'_p(\alpha_3 x_3) \approx G'_p(x_3\gamma_3) \approx$ 200-300 Pa and $G'_p(\alpha_3\gamma_2) \approx 3000$ Pa (Fig. C.2). Thus, we find the plateau modulus grows in magnitude roughly 10-fold or 20-fold when changing valence from 3 to 5 or 6, respectively. In chapter 3, we observed similar magnitude changes between similarly concentrated valence 3, 5, and 6 homotypic NS networks, which was attributed to approaching an isostatic threshold [27]. Therefore, the isostatic point in heterotypic networks also occurs somewhere between a valence of 5 and 6.

The strain sweep behavior of the valence 5 and 6 networks measured here also further supports the isostatic interpretation (Fig. C.4). In particular, we found that at shearing frequencies in the elastic regime, the strain sweeps on 5 and 6 arm heterotypic NSs are essentially identical to the α_6 NSs, which exhibit no strain hardening and immediately yield after their linear regime. Recall that, in Chapter 3, we attributed this diminished strain behavior indicated a reduction in available configurations of the un-stretched net-

work state due to the onset of isostaticity. Thus, here, we also interpret that all valence 6 NS networks are above or at the isostatic point, whereas the valence 5 network is just below the threshold.

5.5.5 High-frequency stress-relaxation in G'' is independent of valence and sticky-end strength

Interestingly, regardless of salt or binding motif, all NSs displayed $G'' \sim f^{-3/5}$ for roughly one or more decades of frequency during the plateau response before reaching a minimum (Fig. 5.2−5.5 and C.2). The similarity of the loss modulus with frequency showing $G'' \sim f^{-3/5}$ in all NS solutions is intriguing given that the NSs have different valences and binding sequences. The scaling relation, however, does suggest there are multiple, similar relaxation modes at high frequencies available in all NS networks, as a simple Maxwell material shows $G'' \sim f^{-1}$ during the plateau regime [1]. For instance, similar departures from $G'' \sim f^{-1}$ have been observed in entangled polymer networks during the plateau regime [123–126], which arises from uncorrelated, subdiffusive Rouse-like monomer displacements on a reptating chain [127].

In NS networks, the high-frequency elastic response results from an instantaneously bonded stress-bearing network [27] and not entanglements of long NS chains. Indeed, when performing dynamic light scattering experiments on 3 and 4 arm NS networks at time scales similar to the elastic plateau regime ($\lesssim$ 0.1-1s, or $f >$ 1-10 Hz), slow topological relaxation modes from bond rearrangement have been observed [13,32]. Interestingly, the scaling exponent for the slow relaxation modes with wave-vector, $0 < q < 0.3$, suggest the rearrangement motion is sub-diffusive. It is not clear how the exponent q observed in DLS measurements relates to the observed $G'' \sim f^{-3/5}$. That said, all NS networks having $G'' \sim f^{-3/5}$ suggest: (i) there are uncorrelated, sub-diffusive monomer displacements

due to topological rearrangements leading to this power-law exponent (*ii*) this uncorrelated relaxation event is independent of NS valence and binding strength. Further, our data does show, that valence and binding strength largely determines the viscosity of the network and, thus, the pre-factor for the scaling $G'' \sim f^{-3/5}$.

5.6 Conclusion

In this chapter, we continued leveraging the programmability of DNA nanostars to investigate the microscopic parameters controlling equilibrium gel viscoelasticity. In particular, we observed that:

(1) the time-scale for simple liquid-flow is determined by the free energy of a single NS-NS bond formation, valence of the NS bond (determining the terminal response), and added salt in solution

(2) for all salt conditions, $G' \sim G'' \sim f^{2/3}$ persisted during the non-Maxwell power-law regime in $\alpha_3\gamma_3$ NSs networks

(3) changing the strong γ-bond on $\alpha_3\gamma_3$ to one slightly weaker (*i.e.,* β) slightly changed stress-relaxation from $G'_{\alpha_3\gamma_3} \sim f^{2/3}$ to $G'_{\alpha_3\beta_3} \sim f^{3/4}$

(4) changing overall NS valence from 6 to 5, but retaining a strong-bond valence of two, only marginally affected stress-relaxation from $G'_{\alpha_4\gamma_2} \sim f^{1}$ to $G'_{\alpha_3\gamma_2} \sim f^{11/10}$

(5) two-mode Maxwell rheology in a 6 arm heterotypic NSs can be recovered when the weak bonds do impart enough viscosity to appreciably affect relaxation of the strong-bonded network

(6) $G'' \sim f^{-3/5}$ in the rubbery plateau regime holds for all NS types and salt conditions and indicates a sub-diffusive origin of stress-relaxation at high-frequencies.

We found that the power-law exponent scaling G'' with frequency of observations (2)-(4) are all consistent with predictions from the model derived in Chapter 4, giving further validation to its predictive power. We also want to emphasize that points (1) and (3)-(5) further demonstrate how small sequence changes in the NS oligos can lead to drastically different bulk viscoelastic responses. We conclude that the insights gained here in how to modulate the stress-relaxation properties in equilibrium NS gels can be applied to other equilibrium gels made from NS-like particles.

Chapter 6

Summary and Future Outlook

6.1 Summary

The core work of this thesis demonstrated the effect of particle valence on the phase behavior and viscoelasticity of equilibrium gels. We achieved this by making equilibrium gels self-assembled from DNA nanostars, cross-linking nano-structures with well-defined binding interactions and valence. The precise control over NS valence allowed us to probe the changes to the resulting rheology and phase behavior. To gain insight into how those properties were affected by valence, we compared the responses of the various gels to each other and, also, to general mechanistic models (both existing and a new one established in Chapter 4).

In chapter 2 of this thesis, we tested the effects of NS valence on their resulting temperature-concentration phase diagram using a new emulsion-based imaging technique we developed. In particular, we took advantage of the spherical geometry of the NS condensates and emulsion droplets to accurately measure the volume fraction of the condensate, ϕ_{den}, using precision fluorescent microscopy. By using a microscope lens with a large depth of field, W, we demonstrated that, for emulsion droplets smaller than W, the entire volume is captured in the image. This, in turn, implied the intensity profiles of each phase inside the emulsified droplet were projected entirely into the $2d$ image.

We accordingly fit the projected intensity at every pixel in the image to make highly precise measurements of the condensate and emulsion droplet radii. The intensity was found to be well-fit by a piece-wise function describing the sum of two uniformly bright, nested spheres A.3. Thus, the resulting condensate volume fraction $\phi_{\text{den}} = (r_{\text{den}}/r_{\text{dil}})^3$ was precisely measured from the two fitted radii.[1] The error on ϕ_{den}, for a particular NS concentration, was further reduced by measuring the volume fraction of many emulsified NS condensates found in the same single wide-field image and who were all procured from the same mother stock solution. For all NSs, after measuring the ϕ_{den} of many condensates, we found that ϕ_{den} grows linearly with NS concentration, [NS], characteristic of the underlying equilibrium, binary phase separation process. By applying the lever rule (Eq. 2.1) to ϕ_{den} versus [NS], we then extracted the dense and dilute phase concentrations. We did this lever rule measurement routine for many different temperatures, in combination with videos measuring the condensate melting temperature, to map out the resulting temperature-concentration phase diagram of NS solutions. We propose this method can be generally used to measure the phase diagrams of many other types of systems undergoing liquid-liquid phase separation.

For all NS valences, the phase diagrams of homotypic NS solutions had a similar shape, namely there existed an upper critical solution temperature, T_c, below which a coexistence regime emerged. In particular, for all solutions, the width of the regime increased rapidly for $|T - T_c| \lesssim 10°\text{C}$ and then stabilized at temperatures below that. However, between solutions of different valences, the area of coexistence did change as the NS valence increased, particularly with an increased ϕ_{den} and a larger T_c. The increased condensate density and T_c is qualitatively consistent with the increase in bonds required to make a fully bonded condensate as NS valence increases. We were able to

[1] Recall the dilute phase pervaded the remaining volume in the emulsion droplet. We therefore labeled the emulsion droplet radii as r_{dil}.

further quantitatively understand the valence behavior of T_c by comparing it to mean-field model estimates for the melting temperature of a single NS-NS bond [59] and critical temperature calculations found using a 1st order thermodynamic perturbation theory incorporating particle valence (*i.e.,* SAFT/Wertheim theory) [36, 62–64]. Comparison of data to those theories demonstrated that, when NS valence is below four, the connectivity of the NS largely determines T_c. But, beyond a valence of four, the thermal stability of the NS-NS bond limits T_c. We propose that the insight learned here, namely the valence and binding strength effects on T_c, can be extended to other systems undergoing equilibrium liquid-liquid phase separation facilitated by weak, limited-valence interactions.

In chapter 3, we used oscillatory shear rheology to probe how NS valence changes the rheological properties of concentrated homotypic NS equilibrium gels. We generally found all homotypic NS equilibrium gels, independent of valence, to have a Maxwell-like frequency-dependent viscoelastic spectra. That is, the solution flowed like a liquid below a characteristic relaxation frequency, f_c, and elastically beyond f_c. However, the relaxation time, $\tau_c = 1/f_c$, and network elasticity, G'_p, did increase as a function of valence. In particular, at the same NS concentration, τ_c and G'_p respectively increased 10-fold and 25-fold when the valence increased from 3 to 6. We also found that the same valence increase removed the strain hardening behavior from the network and caused the network to immediately yield after its linear regime, indicative of increased constraints on network chains. The observed increase in network constraints and large increase in τ_c and G'_p between 3 and 6 arm NSs demonstrated that the NS network junctions approached an isostatic point. At the isostatic point, the number of connections made at a network junction matches the number of degrees of freedom of the junction, locking the junctions into place [15, 16, 92, 128]. The locking of junctions, in turn, increases network rigidity much more than the contribution from the entropic elasticity connecting junctions [15,16,92,128] and, also, suppresses the configurational entropy of the network [128]. The

rheology data presented in Chapter 3 suggests the isostatic point in equilibrium NS gels occurs somewhere between a valence of 5 and 6. We note, however, that in equilibrium NS gels, the thermal fluctuations between the junctions induce strain on the network that masks the increases due to isostaticity [128]. The thermal fluctuations of the NS junctions result in an entropic elasticity between the NS-NS connections, which was seen in the similarity of the measured chain spring constant to the spring constant calculated for a freely jointed chain with segment length equal to a NS arm. We therefore conclude that, in equilibrium NS gels, the viscoelastic response is controlled by a combination of entropic elasticity between NS-NS connections and NS valence.

In Chapter 4 and 5, we saw that a heterotypic NS, a NS with both a strong and weak sticky-end, resulted in equilibrium gels that display non-Maxwell power-law rheology rheology between its two bond lifetimes. Using the principles we learned in Chapter 3, we posited that the non-Maxwell rheology in such networks resulted from a dynamic decrease in network valence as the weak-bonds dissociate, thus driving constraint releases in the stress-bearing network. The constraint releases, in turn, allowed the size of strain fluctuations, ξ, in the network to grow, which relax at a characteristic frequency set by the current state of network valence and viscosity resisting fluctuations. For heterotypic NS solutions, we found ξ scaled with frequency of shearing according to $\sim f^{-1/3}$, consistent with our mean-field model predictions for Zimm-like stress-relaxation (developed in Chapter 4). Using the relation for $\xi(f)$, our model then derived an expression for the scaling exponent relating G' to f (Eq. 4.3), showing that $d_{\min}$ in the strong-bonded network determines the power-law exponent. We demonstrated that values of $d_{\min}$ consistent with previous NS measurements and expected NS design predicted scaling relations for G' with f in great agreement with our measurements and found that scaling relations for G' with f are largely altered by the valence of the strong-bonded network. The agreement between our measurements and our model predictions gives strong support to the

predictive power of equation 4.1 and 4.3. We accordingly demonstrated the generality of our model by showing it successfully recovered the non-Maxwell power-law rheology observed in critically isostatic $2d$ triangular-lattice networks [17, 97]. The broad applicability of our model strongly suggests the mean-field model presented in Chapter 4 can be generally applied to equilibrium gels when the hydrodynamic interactions in solution dominate the viscoelastic response. We conclude that, during such stress-relaxation in equilibrium gels, the structural exponents $d_{\min}$ and d_{fr} of the stress-bearing clusters can be deduced from the power-law exponents scaling ξ and G' with frequency.

6.2 Future outlook

6.2.1 Open questions

In addition to the many insights gained regarding how DNA nanostar (NS) valence and binding strength affects phase behavior and viscoelasticity, there are still open questions. Some of them can be likely be answered with future experimentation. Other questions might be more challenging to answer with current experimental techniques and theoretical understanding. This section will address some of these questions.

Lever rule measurements

Constant ϕ_{den} in lever rule - For all temperatures over which we measured condensate volume fraction ϕ_{den} versus NS concentration [NS], we found there was a characteristic NS concentration $[\mathrm{NS}]_{lp}$ at which the volume fraction stayed constant, $\phi_{den,lp} \approx 5\%$ (Fig. A.5). The physical process leading a temperature-independent $\phi_{den,lp}$ is not quite clear.

The origin of $[\mathrm{NS}]_{lp}$ can be partially understood if we compare the value to other relevant concentrations in the phase separation process. First, $[\mathrm{NS}]_{lp} \approx$ 5-25 μM is much

lower than the critical concentration of phase separation. In particular, based off the value of T_c, the critical concentration is somewhere between $[\text{NS}]_c$ = 80-150 μM, which is greater than $[\text{NS}]_{lp}$.

The phase diagrams do suggest that there is a temperature, T_{lp}, at which $[\text{NS}]_{lp}$ becomes the gas phase concentration and, therefore, $\phi_{den,lp}(T, [\text{NS}]_{lp}) \to 0$. In particular, tracking $\phi_{den,lp}(T) \to 0$ as a function of $|T - T_{lp}|$ may elucidate if there is a critical scaling process controlling $\phi_{den,lp}$ and may help understand the origin of the limiting value at low-T. For viscoelastic fluids, like NSs, the order parameter is particle density and, by relation, volume fraction [14, 129]. In general, during temperature-dependent phase separation, the order parameter(s) of the system, and their related values, will scale with $|T - T_{lp}|$ according to a critical exponent [129]. A very small, fractional exponent, p, for $\phi_{den,lp}(T) \sim |T - T_{lp}|^p$ can give rise to a limiting value of $\phi_{den,lp}(T)$ at temperatures far below T_c. For instance, an exponent of $p = 1/20$ leads to a change in density undetectable by our volume fraction measurements when $|T - T_{lp}| > 5°\text{C}$. In fact, the lowest resolvable volume fraction with the emulsion-imaging method is roughly 2%, leaving only a very small dynamic range (2-5%) accessible for exploration. A method that can resolve volume fractions lower than 2% is thus needed to accurately track $\phi_{den,lp}(T) \to 0$.

If a method to measure lower volume fractions is established, it would be straightforward to prep several NS solutions between $[\text{NS}]_{lp}$ and $[\text{NS}]_c$ for lever-rule measurements to find $\phi_{den,lp}(T) \sim |T - T_{lp}|^p$. It would indeed be interesting to see if the value for p is universal for all NS valences and salt concentrations.

Alter strand stoichiometry - Malformed NSs/weakly-interacting strands are expected to change the relation of ϕ_{den} with total [DNA]. In particular, it ϕ_{den} versus [DNA] will become quadratic [130]. This would be relatively straightforward and worthwhile to test, namely by preparing a NS solution where one strand of the NS is added at a significantly lower amount than the other strands (e.g., purposefully making malformed NSs). Verify-

ing this will determine how accurately ϕ_{den} versus [DNA] can identify the percentage of malformed DNA structures in solution. Such percentages are typically currently found after performing gel electrophoresis, HPLC, or some other separation/chromatography method on annealed DNA solutions.

Viscoelasticity

A large portion of this dissertation involved discussion of NS equilibrium gel rheology. There are still, however, a vast number of open questions uncovered from our rheology.

Valence > 6 NS - A question that is often asked about NS equilibrium gels is whether the plateau modulus G_p' is expected to keep exponentially increasing beyond a NS valence of 6. Simulations demonstrate that beyond the isostatic threshold, there is no longer an exponential increase in network stiffness and that G_p' of hyperstatic networks are similar in magnitude [16, 128]. This is expected to be the case in NS networks, too; that is, a valence 7 NS network is expected to have a similar G_p' as a valence 6 NS. Only two new oligo strands are needed to make a valence 7 NS based off the valence 6 NS sequences, which can be done relatively easily.

G_p' and ξ scaling with [NS] - In the valence 3 homotypic NS networks of chapter 3, we observed power-law behaviors of G_p' and ξ on [NS]. This is in contrast to theory [1, 111, 129] and prior experiment [108] which observe such behavior only after correcting for a critical particle concentration, c_{cr}, e.g., $|c - c_{cr}|$, and also generally find that scaling relations hold when $|c - c_{cr}| \lesssim c_{cr}$ (c is the particle concentration). However, recent simulation work by Pyo *et. al* [131] recently demonstrated that critical scaling relations for surface tension of phase separated condensates can extend far from the critical point provided the ratio of interface width to a critical length scale was optimally set. There may be a similar ratio for NS solutions that ensures critical scaling relations for the cluster-size ξ and, thus, G_p' can extend far from the critical point (e.g., $c \gg c_{cr} \implies$

$|c - c_{cr}| \approx c$). Determining the functional form of this ratio, using a method similar to Pyo *et. al* [131], is worth investigation.

Related to the power-law behavior of G'_p and ξ with non-normalized NS concentration are the structural exponents we deduce from the relations. In particular, for 3 arm NS networks, we found $\xi \sim [\text{NS}]^{0.8\pm0.1}$ and $G'_p \cdot \xi \equiv K_\xi \sim \xi^{1.2\pm0.1}$, implying a 3d percolated structure with mass fractal dimension $d_f = 2.5$ and cluster elasticity dominated by a shortest/minimum-length stress bearing-path with fractal dimension $d_{\text{min}} = 1.2$. Direct structural measurements of d_f and d_{min} for the 3 arm NS solutions are needed to confirm these predictions. Static light scattering measurements are attractive methods that can directly measure the structural exponents of the NS clusters [1]. It is worth noting that our rheology measurements estimate NS clusters to be roughly 100-300 nm in size, making for q-values between 0.002-0.006 Å^{-1}. There are small-angle x-ray scattering setups that can get to such q-values [132]. Thus, provided the NS cluster doesn't restructure (e.g., flow) over the time-scale required to get a decent scattering signal, the mass fractal dimension of NS clusters can likely be measured. Scattering measurements are, however, agnostic to the stress-bearing chains formed in solution and, thus, cannot identify the dominant one in solution. oxDNA simulations of 3 arm NS clusters can likely identify the shortest connected path of bonds within the cluster and, thus, provide estimates for their d_{min}.

Salt behavior - An interesting observation we saw in chapter 6 was that the viscoelastic behavior of a NS equilibrium gel, of either valence 3 or 6, did not appreciably change with salt (Fig. 5.2, Fig. C.2, & C.4 top row). This is intriguing given that increasing salt in DNA solutions further screens the negative charges coming from the phosphates on the DNA backbone [74]. The estimated charge screening length at 25°C, the Debye length λ_D, goes from 1.4 nm down to 0.6 nm over the range of added salt concentrations used (50-300 mM NaCl). These estimates for λ_D are a slight overestimate as there

are also ions that come with dsDNA which contribute to the overall ionic strength in solution [133]. In particular, assuming every phosphate on the DNA bases dissociates exactly one cation [13,133], then the smallest achievable salt concentration will be limited by the phosphate concentration. For instance, for a 400 μM solution of six arm NS, with six 49 nt-long strands composing the NS, there is $\approx$ 118 mM worth of phosphates and, thus, $\approx$ 118 mM cations added to solution. The cations thus increase the ionic strength in solution by 59 mM. Adding this amount to the ionic strength of the added salt concentration (50-300 mM NaCl), we arrive at λ_D(109 mM monovalent) = 0.9 nm and λ_D(359 mM monovalent) = 0.5 nm.[2] These lengths are a bit smaller than the length of the two ssDNA nucleotides separating the arms at the junction, roughly 1.1-1.4 nm in length [134, 135]. This suggests that the arms are not strongly repelled from each other near the junction. A more detailed salt concentration study, particularly at extremely low-salts, should be done to determine if there is a salt condition at which NS arms become strongly repelled and, thus, change the overall gel viscoelasticity.

General

Why are 5 arm NSs so weird? - In both our phase diagram and viscoelasticity measurements, we found that the 5 arm NS took on properties similar to a 4 arm NS. In particular, we found that they both had similar condensate densities, values for plateau modulus, and exponents scaling G'_p with [NS]. The only difference between the 4 and 5 arm NS was found in their strain stiffening behavior, which indicated the 5 arm NSs were more constrained.

At this moment, the physical reasoning for the similarities between 4 and 5 arm NSs is still unknown. A possible hypothesis is that a 5 arm NS is geometrically "frustrated", as there is no an equivalent platonic crystal structure where particles have 5 connections

[2]Valence in this context references to the number of electronic charges on the ion.

in the lattice.[3] This frustration could force some structural change unique to 5 arm NSs bound in the condensed state (e.g., a 'magic number' effect). oxDNA simulations on clusters of 5 arm NSs could help identify is such a structural change exists and if that affects the density of bonds within the condensate. Further, from simulations, the exponent scaling G'_p with [NS] can be estimated from the exponents scaling: (1) the cluster size, ξ, with [NS] (e.g., measure $\xi \sim [\text{NS}]^r$), and (2) the number of NSs in the shortest path in the cluster, $N_{\min}$, with ξ (e.g., measure $N_{\min} \sim \xi^{d_{\min}}$). In particular, since $K_\xi \sim 1/N_{\min} \sim \xi^{-d_{\min}}$ and $G'_p \sim K_\xi/\xi$, then $G'_p \sim [\text{NS}]^{rd_{\min}}$.

6.2.2 Emerging trends

Composite soft materials - A rather difficult next step emerging in the field is engineering a composite soft material (i.e., mixtures of different types of squishy and/or hard colloids) with well-defined bulk properties that can be controlled through the underlying particle interactions [7, 58, 136–138]. In this case, how does the rheology and phase diagram change when there are more than two types of particles in solution? What about the other properties, like optical? Answering these questions are crucial to better engineering designer materials for industrially- and biologically-relevant applications [6, 7, 136, 139–142].

Photo-switchable NS gel using azobenzene modified sticky-ends - Switching between two mechanical states via light is attractive for many biomedical and bioengineering applications [137, 143, 144], particularly because light offers non-invasive and precise spatiotemporal control of material states. In this spirit, work has been done trying to reproducibly switch DNA between being bound and un-bound by shining light on it. Recent work has shown that azobenzene-modified dsDNA sequences can be destabilized

[3] There is an equivalent platonic crystal lattice for particles of valence 4 and 6, the tetrahedral and FCC lattice. Further, four valence 3 NSs can be assembled into a tetrahedral arrangement [13].

by shining UV-light on them [145]. In particular, shining UV-light on azobenzene makes it transition to its cis-state, which causes the dsDNA to dissociate. After a period of time or after shining blue light, the azobenzene will revert back to a trans-state and allow the DNA bonds to reform. Modifying the NS sticky-end sequences will enable the NSs to switch between a fully dissociated state (after shining light) to a fully bound state.

Tracking the viscoelastic spectra of the network as it percolates into a fully-bonded network is a very interesting project worth pursuing. In particular, at the critical percolation point, the hydrodynamic interactions affect the stress-relaxation of the NS network over intermediate to high frequencies [31]. As we saw in Chapter 4, the relevant hydrodynamic interaction limit in a percolating homotypic NS network is the Rouse-limit (e.g., the percolating network is freely-draining). Thus, a photo-switchable NS gel will likely have rouse-like stress-relaxation when it is percolating, giving more experimental evidence capable of testing the scaling model developed in Chapter 4.

Appendix A

Appendix for Chapter 2

A.1 NS, Hairpin, and emulsion preparation

HPLC purified DNA oligomers were purchased in a dehydrated state from IDT, and hydrated with MilliQ water to form stocks with concentrations of $500 - 800$ μM. All DNA sequences used in this experiment are listed in Table A.1. The sequences used for NS-forming oligomers in chapter 2 and 3 were templates for the designs in Table A.1. The sequence of the hairpin-forming oligomer was designed to lack any hybridization with NS sticky ends, and to have a folding (melting) temperature similar to that of the NS arms ($\approx 80°$C).

To assemble an z-armed NS, z constituent oligomers were mixed in a buffer of 40 mM Tris, 11 mM HCl, 1mM EDTA containing either 50, 150, or 300 mM NaCl. In this mixture, 5% of one of the strands was labeled with Cy3 (see Table A.1). For $z = 6$ assemblies, achieving the desired stock concentration required complete dehydration, followed by re-hydration in buffer with 150 mM NaCl. These NS mixtures were then thermally annealed following the protocol detailed in Ref. [27]. Separately, the hairpin oligomer was diluted with the relevant buffer and salt, and annealed it using the same procedure. Final measurement solutions were then made by mixing annealed NS and annealed hairpin, with a hairpin concentration of typically 5 μM; notably, controls indicated that varying

[hairpin] from 0.5 μM to 20 μM had no effect on the volume fraction of the dense NS phase (see Appendix, Fig. A.3). NS concentration was found from these NS+hairpin mixtures by diluting to a 1% solution with added water, melting, measuring the UV absorbance (A260), subtracting the A260 of the hairpin (as measured separately from the hairpin stock), and then estimating the NS oligomer concentration using sequence-dependent estimates of the extinction coefficients [146].

Water-in-oil emulsions were made at $T = 65°$C by delivering 2-3 μL of the NS+hairpin solutions into 40 μL of a mixture of 5% wt/wt fluorinated-surfactant dissolved in a fluorinated oil (008 FluoroSurfactant in HFE7500 oil, RAN Biotechnologies). The solution was held at 60-65°C for 1-2 minutes to disallow phase separation, then emulsified by vortexing for 2-3 seconds at an intensity of roughly an eighth of the maximum on a Benchmark Benchmixer vortexer. This resulted in droplets of the desired diameter ($25 - 120$ μm).

A.2 Imaging protocol

Multi-channel flow cells were created by cutting two vinyl sheets (Cricut Window Cling) with a personal die cutting machine (Cricut Joy). One sheet contained an array of small holes for catching air bubbles, and the second contained an array of channels. The bubble-catching sheet was placed on an ethanol-cleaned glass slide, and pressed and heated to create adhesion. The channel sheet was aligned to the first sheet, adhered through heat and pressure, and finally a cleaned 22x50 mm coverslip was similarly adhered to complete the flow cell.

Images were acquired using a 4x 0.13 NA objective (Olympus UPlan FL) on an inverted, wide-field, fluorescent microscope (Olympus IX70), illuminated with a mercury arc lamp that was attenuated with a 1.0 ND filter. A subset of images were taken with two different 4x 0.1 NA objectives (Olympus Plan N or Nikon Plan Achromat). Fluorescence

imaging was achieved using a 540 ± 30 nm bandpass excitation filter (540AF30 Omega), a 570 nm long-pass dichroic (570DRLP Omega) and a 585 ± 40 nm bandpass filter (HQ585/40 Chroma). Images were captured with a CCD camera (Hamamatsu Orca-R2 C10600) and saved to a computer using the camera's imaging software (HCImage Live).

Temperature was controlled by placing on top of the flow cell a brass heat block through which water was circulated using an external water bath (Neslab refrigerated circulating bath RTE-8). The flow-cell slide and heat block were insulated by a home-made styrofoam casing when imaging. Temperature was recorded using a type-K digital thermometer (Supco SL500TC) outfitted with a thermocouple probe (1.6 mm bead diameter) that was taped between the heat block and flow-cell slide.

Emulsified NS solutions of different [NS] were loaded into distinct channels of the flow cell, heated to dissolve any condensate, then allowed to equilibrate and settle over hours.[1] We note that if NS condensates are melted and quickly quenched below T_c, we found that bubbles of dilute phase are trapped within the NS condensates (Fig. A.8). We accordingly slowly cooled the emulsions below T_c and waited at least 3 hours at room temperature before imaging. The flow cell was then placed on the stage, in contact with the brass block, which was set to the high end of the desired temperature range. The system was allowed to equilibrate for 5-10 minutes, then imaged. Data at subsequent temperatures was acquired by repeating the sequence of temperature change/equilibrate/image.

A.3 Use of ND filter

When using our microscope without an ND filter, I found that condensates melted after illuminating light on them for roughly 5 minutes. This "photo-induced melting" occurred at most temperatures below phase separation and it was accelerated when the

[1] I sealed the flow cell using UV nail polish.

temperature was closer to the critical temperature. The photo-induced melting was also reproducible and, after one melting cycle, did not significantly change the condensate volume fraction.

A.4 Imaging analysis

Images of the emulsified NS+hairpin solutions were first manually processed using FIJI to remove any artifacts (e.g. droplet clusters or visible contaminants), then imported into a custom analysis code written in Mathematica. In that code, the function *ComponentMeasurements* was used to automatically find droplets of the desired size ($25-120$ μm diameter) that were sufficiently separated from other droplets. The relevant droplet images were then cropped and fit to the double-sphere function (see Appendix,, Appendix A.6 Eq. A.1-3) using the *NonlinearModelFit* function. The fitting parameters were used to calculate ϕ_{den}.

A.5 NS-SAFT calculations

The free energy of each NS system were calculated as defined by the NS-SAFT theory detailed in Reference [36] (equations (1-2) and (6-9) in their paper). From the calculated free energy, the critical temperature was found by numerically solving equation 10 in Reference [36] using the *FindRoot* function in Mathematica.

A.6 The Double-Sphere Intensity Function

Consider a sphere of radius R that has its center located at $(x_c, y_c, 0)$, and contains a uniform concentration of fluorophores. Imaging such a sphere vertically projects all

the fluorescent intensity into the (x, y) plane; thus, the intensity profile will follow the thickness profile of the sphere. Particularly, the intensity at point (x, y) will be $I_o(x, y) = 2b\sqrt{R^2 - (x - x_c)^2 - (y - y_c)^2}$, where b is the constant intensity per unit height of the droplet.

When fitting the projected intensity of nested spheres (Fig. A.1A), we utilized a piece-wise fit consisting of two separate $I_o(x, y)$ that are dependent on the respective sphere radii, one for the (brighter) condensate and another for the (dimmer) emulsion droplet. We also include an additive offset term accounting for the background intensity of the image. In particular, we fit the double sphere projection with the following set of equations. For positions outside the emulsion droplet:

$$I(x, y) = a \tag{A.1}$$

where a is the background intensity.

For (x, y) positions within the dilute sphere (but outside the dense sphere):

$$I(x, y) = a + 2b\sqrt{R_{dil}^2 - (x - x_{c,dil})^2 - (y - y_{c,dil})^2} \tag{A.2}$$

where b is the dilute-phase labeling intensity.

And for (x, y) positions laterally within both spheres:

$$I(x, y) = a+2b\sqrt{R_{dil}^2 - (x - x_{c,dil})^2 - (y - y_{c,dil})^2}+2c\sqrt{R_{den}^2 - (x - x_{c,den})^2 - (y - y_{c,den})^2} \tag{A.3}$$

where c is the difference between the dense- and dilute-phase labeling intensities

To extract condensate volume fractions from emulsion images, we fit a piecewise function containing these equations to the 2-d intensity profiles from the measured image.

A.7 Center-to-center NS distance

Generating estimates of the DNA density of $z = 4$ and $z = 6$ NSs in specific (hypothetical) crystal geometries requires an estimate of the maximal center-to-center distance of neighboring NSs in the crystal. We estimate this using the structure of the DNA arms that connect those neighbors. A bound pair of NS arms contains 46 basepairs, bp, of duplex DNA (corresponding to the two 20 bp DNA arms, along with 6 bp from binding of the sticky ends), along with 4 bases of single-stranded DNA (corresponding to the single-base gaps on either side of the sticky end, and attributing 1 unpaired base from each junction). The crystallographic rise per basepair of duplex DNA is 0.34 nm [147]. The maximal inter-phosphate distance for single-stranded DNA is larger, with some disagreement in the literature regarding the exact value; a commonly quoted value is around 0.7 nm [134, 135]. Accordingly, we estimate the maximal center to center distance as $46 \times 0.34 + 4 \times 0.7 = 18.44$ nm. We note this estimate is imperfect; the actual maximal center-to-center distance will be sensitive to structural issues that are unknown (notably, the arrangement of unpaired bases at the junction, and the tendency of any unpaired base to stack onto an adjacent duplex). Further, we note our estimate is larger than a previous estimate of the same value [13], since that prior estimate attributed the duplex DNA rise-per-base to both paired and unpaired bases.

A.8 Bubble rising upwards in viscous media

The time it takes for a spherical bubble to rise upwards a height, h, in a viscous media, of viscosity η, can be found through solving the following equation of motion:

$$\rho_{bub} V_{bub} g \; + \; (6\pi r_{bub} \eta) \cdot dh/dt = \rho_{liq} V_{bub} g \tag{A.4}$$

where ρ_{liq} is the buoyant density of the viscous media and r_{bub}, V_{bub}, and ρ_{bub} denote the bubble radius, volume, and buoyant density, respectively. The first and second term on the LHS is the force due to gravity pulling down the bubble and the Stoke's drag resisting upward motion, respectively. The term on the RHS is the buoyant force making the droplet rise upward. Solving for h in terms of t in Eq. $A.4$ yields:

$$\implies t(z) = \frac{(6\pi r_{bub}\eta_{liq}) \cdot z}{gV_{bub}(\rho_{liq} - \rho_{bub})} \tag{A.5}$$

z	Strand	Sequence (5'→3')
All	1	CTACTATGGCGGGTGATAAAAACGGGAAGAGCATGCCCATCCACGATCG
All	1 Cy3-tag	CTACTATGGCGGGTGATAAAA/Cy3/ACGGGAAGAGCATGCCCATCCACGATCG
All	2	GGATGGGCATGCTCTTCCCGAACTCAACTGCCTGGTGATACGACGATCG
3	3	CGTATCACCAGGCAGTTGAGAATTTATCACCCGCCATAGTAGACGATCG
4	3	CGTATCACCAGGCAGTTGAGAACATGCGAGGGTCCAATACCGACGATCG
4	4	CGGTATTGGACCCTCGCATGAATTTATCACCCGCCATAGTAGACGATCG
5	4	CGGTATTGGACCCTCGCATGAACCATGCTGGACTCAACTGACACGATCG
5	5	GTCAGTTGAGTCCAGCATGGAATTTATCACCCGCCATAGTAGACGATCG
6	5	GTCAGTTGAGTCCAGCATGGAACGCATCAGTTGCGGCGCCGCACGATCG
6	6	GCGGCGCCGCAACTGATGCGAATTTATCACCCGCCATAGTAGACGATCG
N/A	Hairpin	CTACTATGGCGGGTGATAAATT/Cy3/TTTTTATCACCCGCCATAGTAG

Table A.1: Sequences of ssDNA strands used to self-assemble the z-arm NSs and fluorescent hairpin.

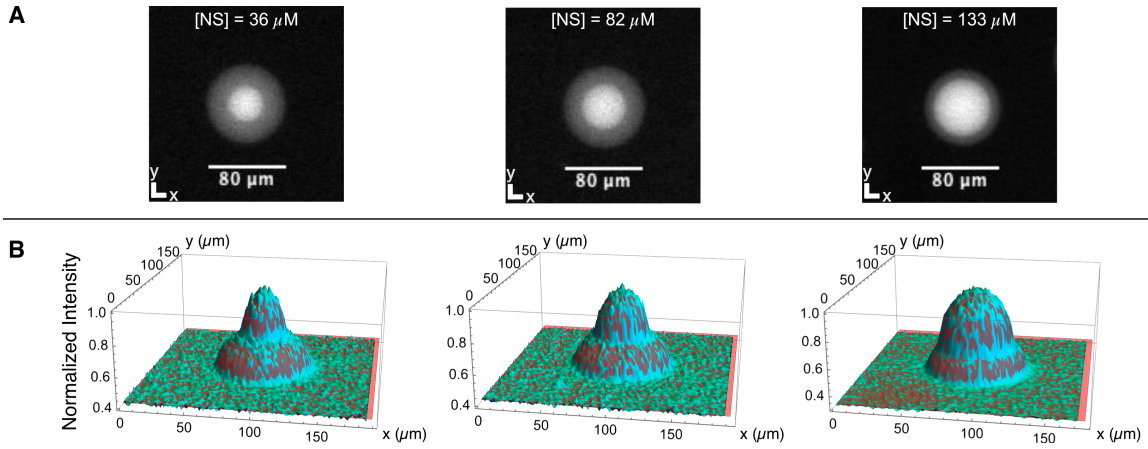

Figure A.1: **(A)** Images of emulsified 4 arm NS solutions that have undergone LLPS at an added salt of 150 mM NaCl and at $T = 33.1 \pm 0.5°C$. The total concentration of NS, [NS], inside the emulsion droplet is labeled on each image. Each image shown is cropped from a larger field of view. In practice, we analyze many droplets (10-100 droplets) in a single field of view taken using a lens with a 4x magnification and 0.13 numerical aperture (and a subset with 0.1 numerical aperture) (See Fig. A.2). Images shown are identical to those in main text Fig 2.1B. **(B)** 3-d plots of the image intensity profile (cyan) of the respective droplets in row **A** and the corresponding surface fits to the intensity profiles (red). The intensities of droplets are normalized by the brightest pixel intensity in their associated photo. In all images shown, there is a notable blue ring at the boundaries between the two droplets, and between the larger droplet and the background; this ring corresponds to diffraction-blurring of the image that is not included in the fit.

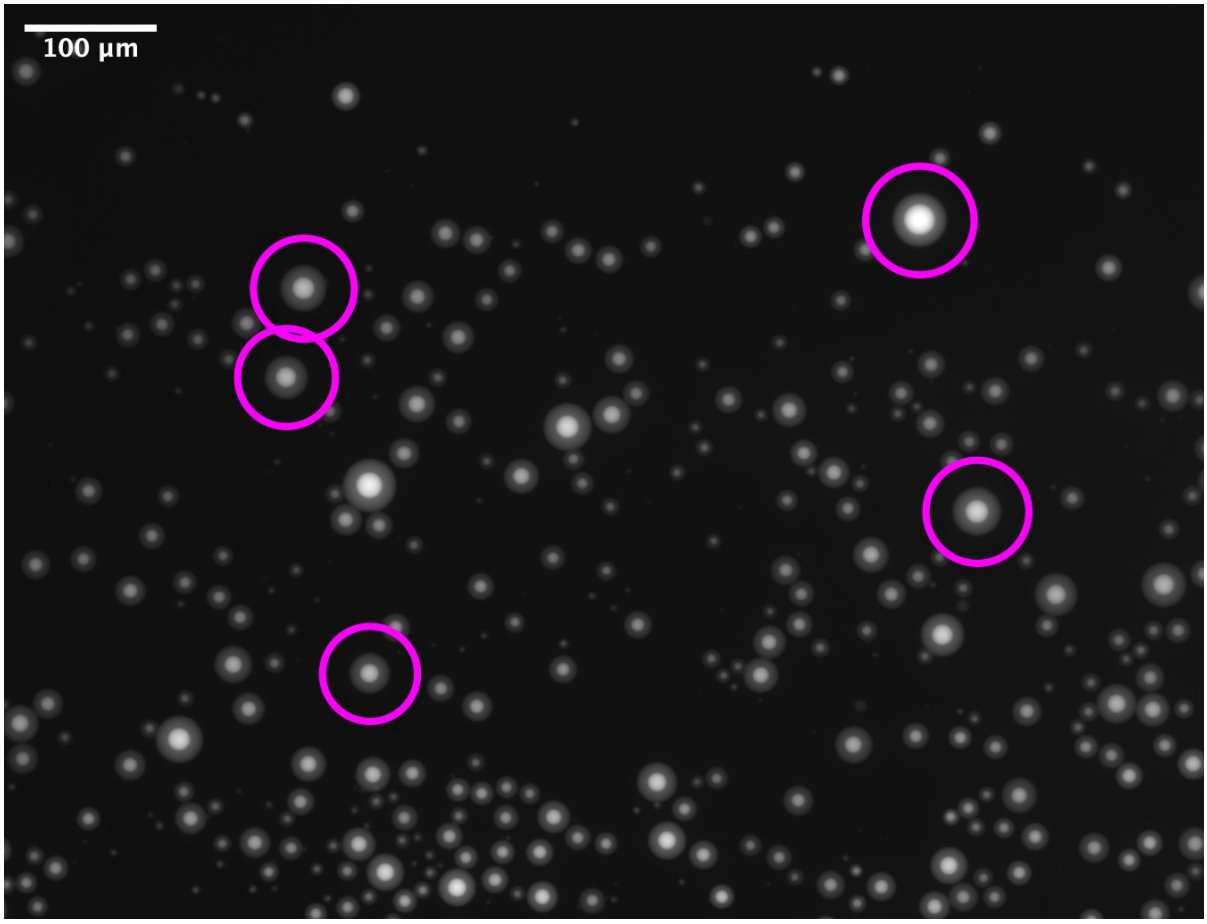

Figure A.2: A representative full-field-of-view image taken with a 4x, 0.13 NA lens containing $\sim$ 100 droplets. The sample is an emulsified 3 arm NS solution at [NS] $= 37.3 \pm 1.2$ μM, [NaCl]= 150 mM, and $T = 22.0 \pm 0.1°C$. Of all droplets observed, only a handful met the stringent criteria used to select droplets for further analysis; those droplets are circled in purple-pink. As discussed in the main text, those criteria were based on droplet size and isolation from other droplets.

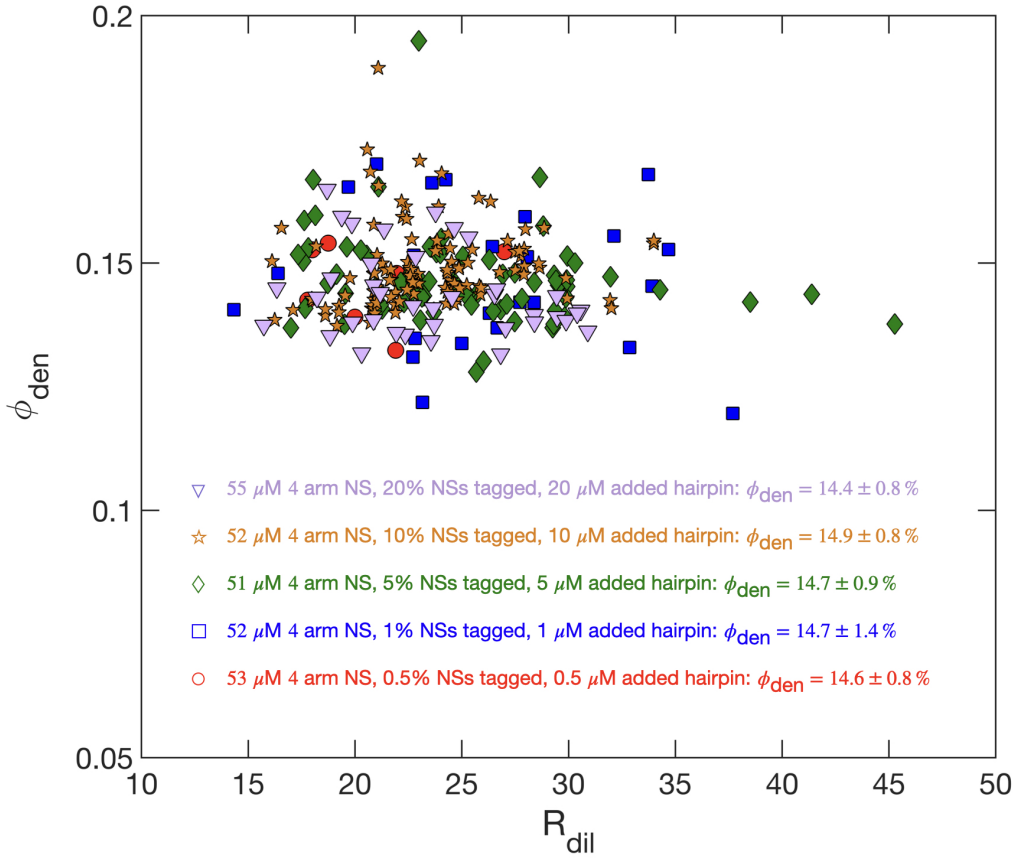

Figure A.3: Measured volume fractions of 4 arm NS condensates with five different added hairpin concentrations (0.5 to 20 μM) and Cy3-tagged NS percentages (0.5% to 20%; varied to maintain similar contrast between dense and dilute phases across all hairpin concentrations). All samples had [NS]= 50 μM, 150 mM NaCl, and room temperature ($\approx$ 21-22$^{\circ}C$). For all added hairpin concentrations, we found that there was no discernible difference between the measured volume fractions; experiments reported in the main text used an added [hairpin] = 5 μM and had 5% of NSs tagged with Cy3.

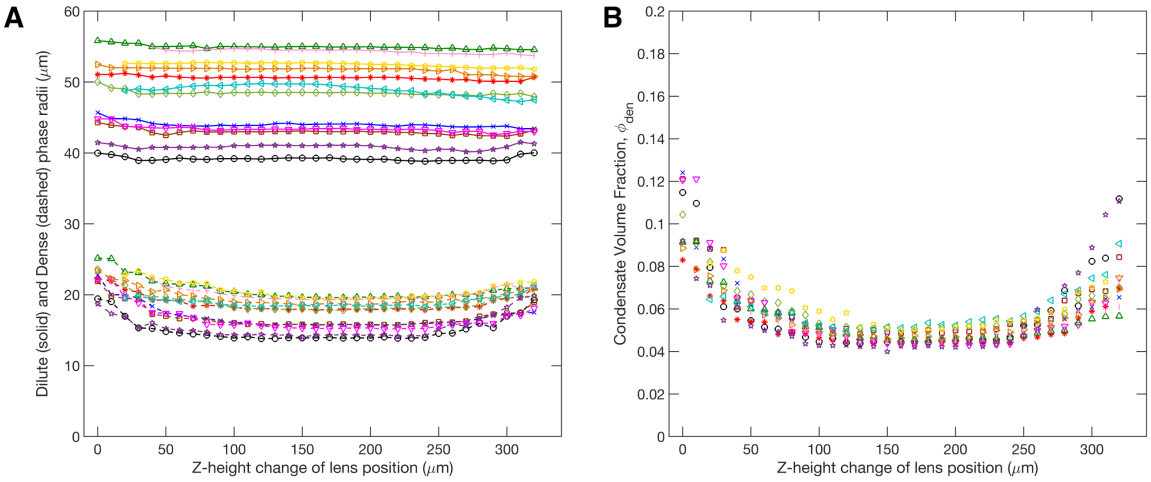

Figure A.4: **(A)** Plot of fitted radii output of several NS emulsion droplets as a function of the z-height position (i.e. focal position) of a 4x, 0.1 NA lens. The data points connected by dashed and solid lines denote the best-fit dense and dilute phase radii, respectively. Solid and dashed line data with the same color indicate fitted radii output from a single emulsion droplet. **(B)** Plot of the corresponding condensate volume fractions from the data shown in panel (A). Notably, there is a $\approx$ 150 μm distance over which the volume fraction is constant, indicating the insensitivity of the measurement to focal position over that range. Further, the collapse of all data to the same volume fraction demonstrates the insensitivity of the method to the absolute radius of the emulsion droplet.

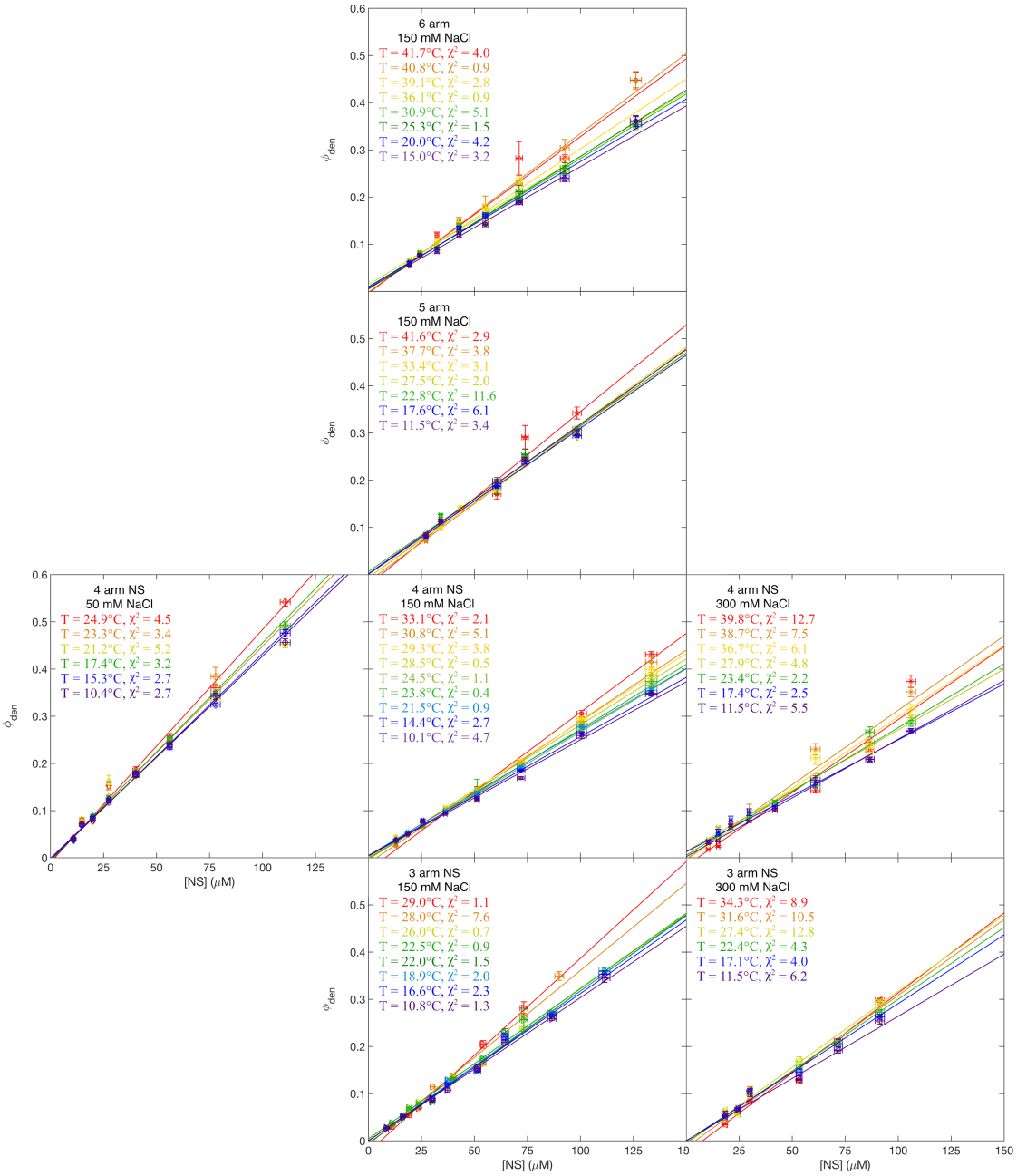

Figure A.5: Plots of condensate volume fraction, ϕ_{den}, vs. total NS concentration, [NS], over a variety of temperatures (as labeled), for all salt and valence conditions explored (as labeled). There are typically 10-30 droplets for a single volume fraction point, with some points having as little as two and some up to 50. Each solid line denotes a weighted linear least squares fit to data of the corresponding temperature. The weights of the fit were given by the errors in both the [NS] and ϕ_{den} axes; the errors are calculated as noted in the caption of main-text Fig. 2.2. The reduced chi square values of each fit are in the legends of each plot.

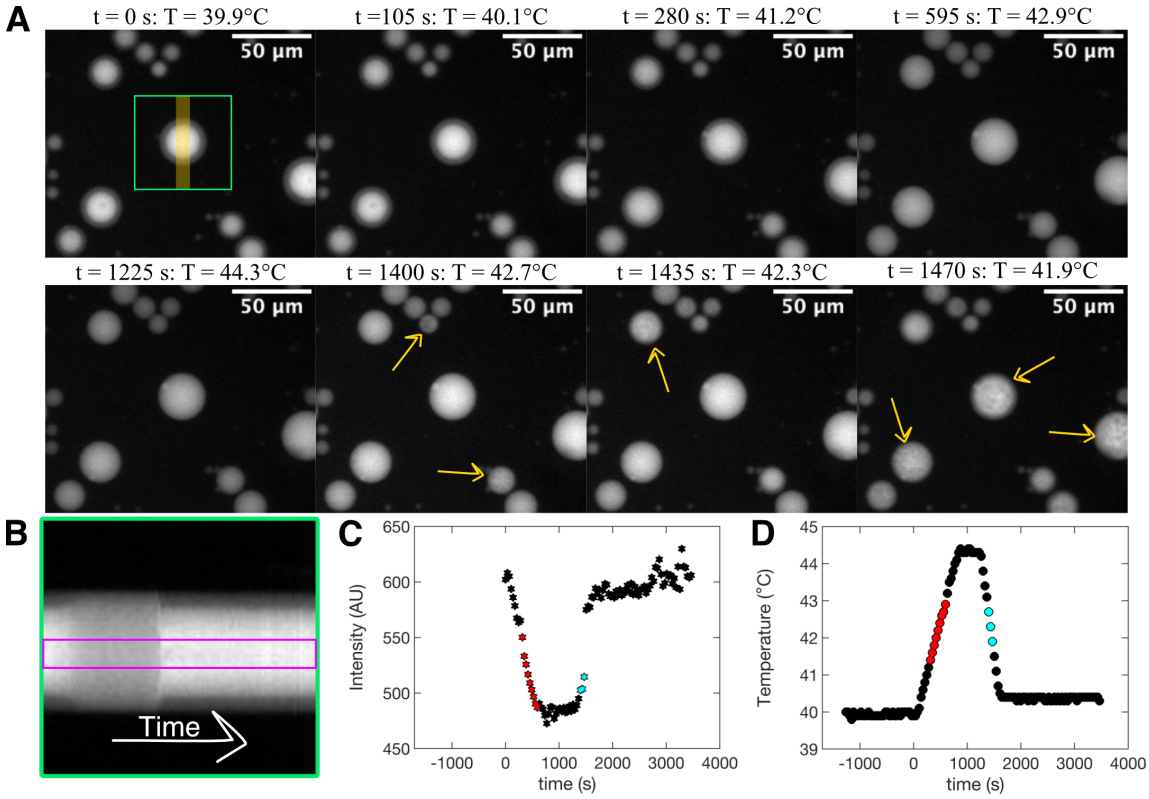

Figure A.6: Demonstration of protocol for measuring melting temperature. **(A)** Image sequence of (top row) condensate dissolution as temperature was increased and (bottom row) formation as temperature was decreased. The sample was a $z = 5$ NS at [NS] $= 128 \pm 3$ μM with [NaCl] $= 150$ mM NaCl. The arrows in the bottom row point out droplets with significant intensity fluctuations (likely corresponding to spinodal decomposition); the range of images over which this is observed is taken to correspond to the temperature range of condensate formation. **(B)** Kymograph of intensity vs time for the droplet boxed in panel A, and generated using the "Multi Kymograph" analysis tool in Fiji [148]. Each vertical column of pixels here is an average of the intensity along the horizontal axis of the yellow bar shown in (A); successive vertical columns show successive time points. **(C)** Plot of condensate intensity as a function of time from the image in (B). The intensity plotted was found by spatially averaging the intensity along the vertical axis of the magenta box in (B) (e.g. along droplet center). In general, we estimate that condensate dissolution occurs during the time (red data markers) when the intensity magnitude is half-way between its value at $t = 0$ s and its minimum (when melted). We note that when the condensate reformed and reached equilibrium, the intensity (at long times) was similar in magnitude to that at $t = 0$ s. **(D)** A plot of the recorded sample temperature as a function of time. The temperatures taken to be the condensate dissolution temperature, T_{diss}, and formation temperature, T_{form}, are highlighted in red and blue, respectively. We used those ranges to calculate a weighted average and uncertainty (or unweighted when hysteresis) in a melting temperature estimate.

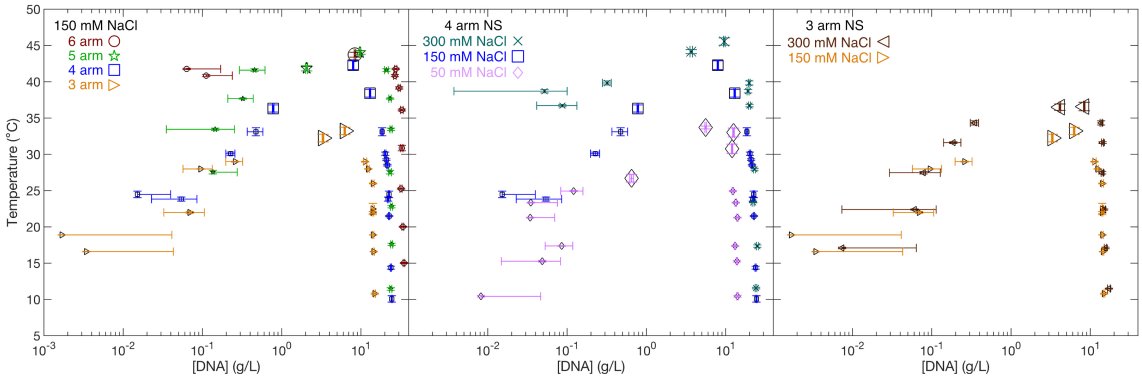

Figure A.7: Temperature vs. log ([DNA]) phase diagram of **(Left)** NSs of various z, all at [NaCl] = 150 mM, and **(Middle)** 4-arm and **(Right)** 3-arm NS at different added NaCl conditions; data shown is identical to that in main text Fig. 2.3 Smaller symbols are data found from lever-rule fits (as in Fig. A.5), while larger symbols denote melting temperature estimates found from kymographs (as described in Fig. A.6). At low temperatures for most NS conditions, we occasionally measure negative values of $[\mathrm{NS}]_{dil}$; such values are not indicated on the semi-log plot here.

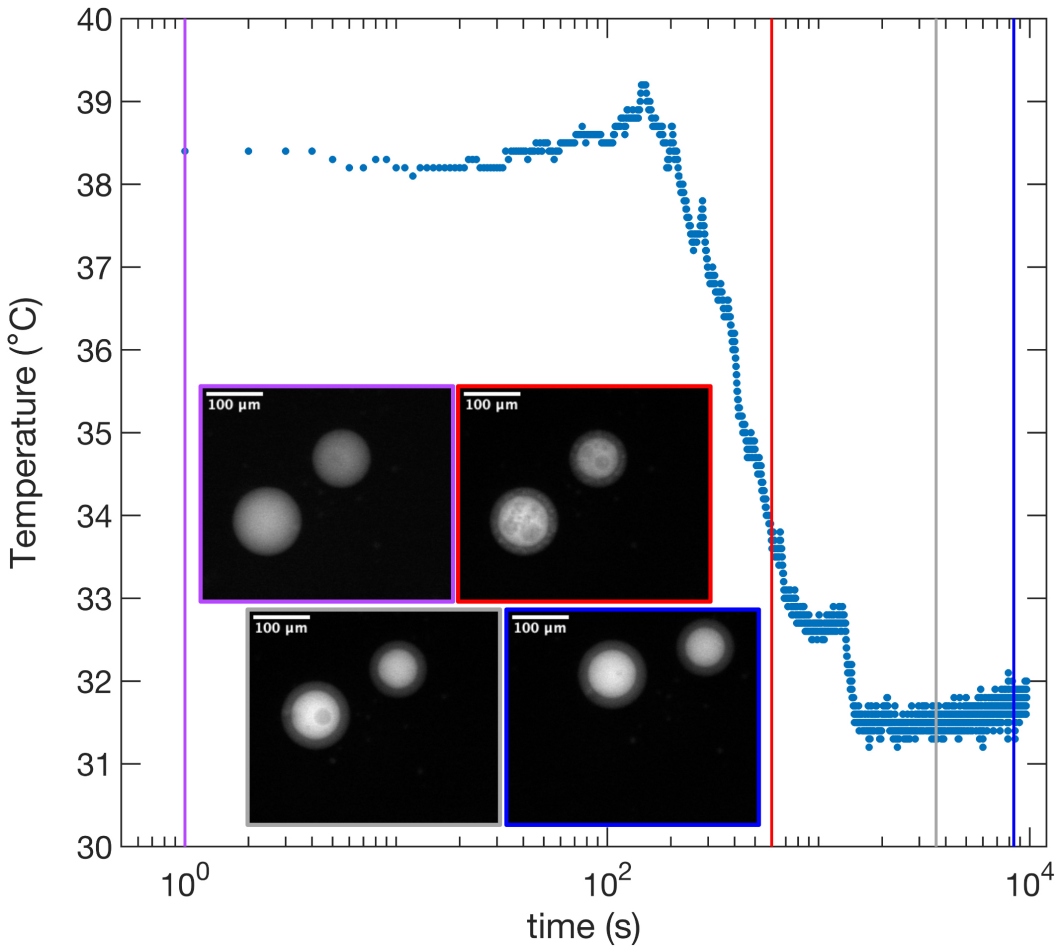

Figure A.8: Temperature vs. time profile when quickly quenching a 4 arm NS below its critical temperature. *Inset:* We found that a quick quench would trap "bubbles" of dilute phase and/or buffer inside the viscous condensate phase. In the inset photos, we track a bubble of dilute phase of $\approx$ 30 μm in diameter that took roughly 2 hrs $\approx$ 7200 s to equilibrate out of the condensate of $\approx$ 90 μm in diameter. We note this time is consistent with the estimated time for a 30 µm diameter water droplet to rise up 90 µm inside a viscous DNA solution with viscosity equal to that of the condensate ($\eta \approx 40$ Pa s at $T \approx 30$°C for 4 arm NS condensates and ρ_{liq} =1.7 kg/L is the buoyant density of DNA). See Section A.8, Eq. A.5 for the exact equation used to estimate the equilibration time for this bubble rising process. After we confirmed the condensates were free of bubbles, we began acquiring images for lever rule volume fraction analysis.

Appendix B

Appendix for Chapter 3

B.1 DNAns design and oligos

Each z-armed DNAns in chapter 3 is formed from z oligos, 49 nucleotides (nt) in length (see Table A.1 and B.1). Each arm consists of a 20 bp dsDNA segment terminating in a 7 nt ssDNA segment with sequence 5'-ACGATCG-3'. The self-complementary sub-sequence 5'-CGATCG-3', commonly referred to as a sticky-end, mediates binding between any two DNAns arms. Unpaired adenines at the vertex and preceding the sticky-end increase the internal conformational freedom of the DNAns and the conformational freedom of the DNAns-DNAns bond, respectively [31, 81, 83].

All oligos were purchased purified with standard desalting from Integrated DNA Technologies (www.idtdna.com). Nucleotide sequences for the $z = 3$ and $z = 4$ DNAns designs were taken from Biffi, *et. al* [13]. Additional sequences for $z = 5$ and $z = 6$ DNAns were designed using NUPACK [84] with the goal of having DNAns formation be stable at $T = 65°\text{C}$ and bind one another around $T = 35°\text{C}$.

B.2 DNAns solution preparation

DNAns solutions were prepared from ssDNA oligo stocks by mixing equal amounts of each of the z oligos. After mixing, the solutions were completely dehydrated in a vaccuum concentrator (Savant, Speedvac) with a filter over the sample tube opening to prevent dust from entering the sample. The sample was then re-hydrated to the desired DNAns concentration in a buffer solution of 150 mM NaCl, 40 mM Tris, 40 mM Acetate, and 1 mM EDTA (pH 8.0). To dissolve the DNA completely, samples were placed in an aluminum heat block at 60°C and mixed vigorously for 15-30 seconds every 15 minutes until no visible dehydrated DNA remained. Finally, the solutions were annealed by heating to 90°C for 20 min in the heat block, turning off the power, and allowing the sample to cool to room temperature in the block over ≈5 hours. During the entire annealing procedure, a Styrofoam box covered the heat block to insulate the samples from the surrounding environment. Once annealed, DNAns solutions were stored in a refrigerator (4-6°C) and used within 10 days.

B.3 DNAns concentration

Concentration was determined from A260 of solutions that were diluted 100-fold and 10,000-fold in deionized water. Concentration measurements were made one day after annealing and again immediately after recovery from the rheometer.

The range of DNAns concentrations explored was limited at the high-end to < 800 μM by solubility, and at the low-end to $> X$ μM by phase separation [13, 34, 61, 81, 83]. Phase separation was inferred from the onset of erratic variations in rheological data observed at $X < \{190, 280, 280, 350\}$ μM for $z = \{3, 4, 5, 6\}$, respectively.

B.4 Rheology measurements

Oscillatory shear measurements were performed in a parallel plate geometry using a stress-controlled, direct-strain rheometer (AR-G2 Rheometer; TA Instruments). Parallel plates were chosen to minimize sample volume (80 μL). The bottom plate was a stationary, temperature-controlled stage ($\pm$0.020°C). The top plate was a circular, steel plate of radius $r = 10$ mm, that rotated freely via a magnetic bearing.

To load the rheometer, solutions were heated to 60°C - a temperature at which DNAns are stable but do not bind one another, making the solution easy to manipulate. Solution was delivered onto the bottom plate of the rheometer, which was at room temperature, and sandwiched between both plates until the desired gap size, $g = 200$ μm, was achieved.

Before any rheological measurements were performed, the solution was quickly annealed a final time while loaded in between the rheometer plates: it was quickly heated at $|dT/dt| \leq 15$°C/min to 60°C, held there for 5 minutes, and then quickly cooled ($|dT/dt| \leq 15$°C/min) to the first measurement temperature. A layer of low viscosity mineral oil (Fisher Scientific CAS 8012-95-1; Saybolt Viscosity = 162) was placed over the exposed sample to prevent solvent evaporation during the experiment.

Two types of oscillatory shear-flow measurements were performed: frequency sweeps and strain sweeps. During the frequency sweep, the storage modulus (G') and loss modulus (G'') were measured as a function of oscillation frequency (0.63 rad/s $< \omega <$ 63 rad/s) at a single strain ($\gamma = 5\%$). During the strain sweep, torsional stress, σ, was measured as a function of strain $\gamma = (r\Delta\theta/g)$, where $\Delta\theta$ is the angular displacement of the steel plate, at a single frequency. We measured σ over the range $1\% < \gamma < 200\%$ at $\omega \geq 63$ rad/s and $T = 20$°C (Appendix, section S2 & S3).

B.5 DNAns-specific information

This section includes information regarding the DNA sequences used for each DNA Nanostars (DNAns) design, DNA concentration measurements, binding probability calculations, and hysteresis of structure formation:

B.5.1 DNA sequences

Each of the z single-stranded (ss) DNA segments required to make $z = 3, 4, 5$, and 6 DNAns are 49 nucleotides long. In each sequence, 40 of the nucleotides are designed to form portions of an arm, 6 constitute the sticky-end, and 3 are unbound (Table B.1).

B.5.2 Binding probability and mean valence calculations

We can get a sense of the magntiude of the change in connectivity from calculating the binding probability, p_b, between two DNAns arms. p_b was calculated in a mean-field approximation that ignores connectivity using the DNA thermodynamics package NUPACK [84]. For our overhang sequence 5′-ACGTACG-3′, and an oligo concentration of z·[DNAns], we find that $p_b > 0.84$ at $T = 35°C$, the highest temperature explored, and grows slowly to $p_b \approx 1$ at $T = 5°C$ (see Fig. B.1). This leads to a predicted mean-valence, $\langle z \rangle \approx p_b z \approx 0.98z$ at $T_{\text{ref}} = 20°C$. The use of such a model to calculate p_b for the DNA nanostar system was quantitatively validated by Rovigatti *et. al.* [61] in comparison to DNAns simulations that incorporate connectivity.

B.5.3 Concentration measurements

We used a droplet spectrophotometer (Nanodrop 2000c; Fisher Scientific) to measure the absorption at 260 nm (A260) and derive the DNAns concentration, [DNAns], of z-

armed DNAns solutions (Fig. B.2 and Fig. B.3). The A260 of an z-armed DNAns solution is related to its [DNAns] by

$$[\text{DNAns}] = \text{A260}/(\Sigma_i \epsilon_i) \tag{B.1}$$

where ϵ_i is the extinction coefficient of the i^{th} ss DNA segment composing the z-armed DNAns (see B.1 for the extinction coefficients). Note that equation B.1 assumes all DNAns in solution have completely denatured into their single stranded components.

The DNAns concentrations of solutions prepared for the rheometer were so large that their A260 could not be measured directly. The A260 of solutions diluted 100-fold, $\text{A260}_{1\%}$, in pure water was measurable, but we questioned whether this dilution was sufficient to completely denature the DNAns and permit the use of equation B.1. To check, we compared the A260 of a 100-fold dilution of the most concentrated sample of a given valence, $\text{A260}^*_{1\%}$, to the A260 of a 10,000-fold dilution made in pure water from that same 100-fold dilution, $\text{A260}^*_{0.01\%}$. In all cases, $100{\cdot}\text{A260}^*_{0.01\%} \geq \text{A260}^*_{1\%}$, consistent with incomplete denaturation at 100-fold dilution (Table B.2).

The proportion of single-stranded DNA present in the 100-fold diluted solutions, α, can be calculated based on the extinction coefficients of single-stranded (ss) and double-stranded (ds) DNA [149]

$$\epsilon_{\text{ss}} = [37\,\mu\text{g}/(\text{mL}\cdot\text{cm})]^{-1} \qquad \text{and} \qquad \epsilon_{\text{ds}} = [50\,\mu\text{g}/(\text{mL}\cdot\text{cm})]^{-1}$$

given that the absorbance of the 1% solution is due to both ss and ds DNA

$$\text{A260}^*_{1\%} = \alpha\,\frac{c}{37} + (1-\alpha)\,\frac{c}{50} \tag{B.2}$$

and assuming the absorbance of the 0.01% solution is due to only ss DNA

$$\mathrm{A260}^*_{0.01\%} = 0.01\ \frac{c}{37}\,, \tag{B.3}$$

where c is the total mass concentration of DNA present in the 1% solution. Dividing equation B.2 by B.3, we can derive an expression for α:

$$\alpha = \left(\frac{\mathrm{A260}^*_{1\%}}{\mathrm{A260}^*_{0.01\%}} - 74\right)/26 \tag{B.4}$$

We found α ranged from $\approx$ 30% for the most concentrated 3-arm nanostar solutions, to $\approx$ 96% for the most concentrated 6-arm nanostar solutions (Table B.2). We note that we assumed α was concentration independent and only measured the α of the most concentrated solution at a given z in order to interpret the $\mathrm{A260}_{1\%}$ of all (less concentrated) solutions of a given z-armed nanostar and, thus, avoid an excessive amount of multi-step dilutions.

Since α tracks the correct portion of ss and ds DNA present at the 1% dilutions, we used it to correct the measured [DNAns] from the respective $\mathrm{A260}_{1\%}$ measurement because using equation B.1 assumes the 1% solution contains only ss DNA (*i.e.*, equation B.1 assumes $\mathrm{A260}_{1\%} = c/37$). The correction is found by dividing the ideal A260 for ss DNA solutions, $\mathrm{A260}_{\mathrm{ss}} = c/37$, by equation B.1:

$$\text{correction} = \mathrm{A260}_{\mathrm{ss}}/\mathrm{A260}^*_{1\%} = 1/(0.24 \cdot \alpha + 0.76) \tag{B.5}$$

For the lowest and highest measured α, the correction to the concentration was $\approx$ 23% and $\approx$ 1%, respectively (Table B.2). We note that the error introduced to the [DNAns] by assuming a concentration-independent α has little to no effect ($<<$ 1% error) on the scaling exponents measured from the $G'_p([\mathrm{DNAns}])$ data because the relative ratio of

concentrations are kept the same when using a concentration-independent correction.

B.6 Frequency sweep technical information

This section includes information regarding time-temperature superposition (i.e., master curve construction) and network relaxation time:

B.6.1 Hysteresis measurements

We tested for hysteresis of structure formation by repeatedly measuring the storage, G', and loss, G'', modulus as a function of temperature at $\gamma = 5\%$, $\omega = 10$ rad/s, and at two different rates of temperature change, $|dT/dt| = 1.5$ and 15°C/min. G' and G'' were independent of the rate of cooling and heating for rates $|dT/dt| \leq 15$°C/min for all z and [DNAns] (Fig. B.4). The rate at which temperature changed between the different temperature measurements of $G'(\omega, T)$ and $G''(\omega, T)$ contributing to the master curve was $|dT/dt| \leq 15$°C/min. Thus, all DNAns networks studied here form reversibly and are always in equilibrium.

B.6.2 Time-temperature superposition

Time-temperature superposition (TTS) constructs a material's viscoelastic response over a wide range of frequencies by superimposing frequency sweeps made at different temperatures onto one another. The resulting superimposed curve is known as the "master curve". We used the TTS protocol provided in the rheometer's proprietary software (TRIOS v.4.0.1, TA Instruments) to construct master curves at a reference temperature of $T_{\text{ref}} = 20°C$, allowing for both vertical and horizontal shifts of the raw frequency sweeps. An example of the TTS process is illustrated in Figure B.5. Figures B.6A and

B.6B show all vertical and horizontal shift factors from the TTS procedure vs. temperature for all valences.

The vertical shift factor accounts for slight changes in connectivity (Fig. B.1) that result in an $\approx 40-80\%$ increase in G' (Fig. B.6B). The horizontal shift factor accounts for changes in DNAns binding dynamics and exhibits an Arrhenius temperature-dependence (see section B.6.2, Fig. B.7).

B.6.3 Relaxation times and Arrhenius dependence of relaxation times

The horizontal shift factor is the ratio between the DNAns network relaxation times at two different temperatures. For all z and [DNAns], the relaxation times show an Arrhenius temperature behavior, $\tau_c \propto \exp(E_A/RT)$ (Fig. B.7), with an activation energy, E_a, that is independent of [DNAns] and z. Averaged over all [DNAns] and valences, $\langle E_a \rangle = 210 \pm 10$ kJ/mol.

This value is consistent with the enthalpy of binding of the overhang, $|\Delta H| = 239$ kJ/mol, which was calculated using the two-state melting application on the DINAmelt web server for overhang concentrations between 600μM and 3600μM at $T = 20°$C and 150mM NaCl [150, 151]. Thus, for all z and [DNAns], the relaxation time τ_c of the network is determined by the kinetics of a single DNAns-DNAns bond.

B.6.4 Numerical estimate of solvent-drag-induced crossover frequency ('non-affine-to-affine model')

It has been shown that a Maxwellian crossover in G' and G'' can arise from solvent drag inducing a non-affine to affine transition in networks [17, 85, 98]. Following ref. [17], a crossover induced by solvent drag should occur at a frequency $f_c \approx K_c/\alpha$, where K_c is

the network chain's spring constant, and α is the drag coefficient of a node. We showed in the main text that $K_c \approx 10^{-4}$ N/m for a simple FJC model of DNAns arms; this was validated by the similarity of this value to estimated cluster spring constants. We then estimate the drag from a Stoke's picture: the drag of a sphere is $\alpha = 6\pi\eta a \approx 1.5 \times 10^{-10}$ N s/m, where $\eta \approx 1$ mPa s is the water viscosity, and the sphere radius $a \approx 8$ nm is set to the DNAns arm length. Note that this overestimates the drag, since the DNAns does not occupy all volume within the sphere, and leads to an underestimate of f_c. Regardless, the crossover frequency is then $f_c \approx 7 \times 10^5$ Hz, which, while an underestimate, exceeds the measured crossover frequencies by five orders of magnitude. This indicates that the measured crossover is not caused by solvent drag, and supports the contention that it is instead caused by the kinetics of bond breakage (Section B.6.3).

B.7 Strain sweep specific information

This section includes information regarding the strain sweep measurement, characteristic and yield strain measurements, and the uniaxial extension ratio calculation:

B.7.1 Linear and non-linear elasticity of DNAns networks

To investigate the linear and non-linear response of DNAns networks, we measured the storage, G', and loss, G'', modulus over a range of strains $1\% \leq \gamma \leq 200\%$ at a single frequency, $\omega > 62$ rad/s, and temperature, $T = 20°$C, using a discrete logarithmic sampling distribution of 10 points per decade. For all DNAns networks, G' and G'' were strain-independent for $\gamma \leq 10\%$, consistent with measuring a linear elastic response to applied deformation (Fig. B.8). After the strain-independent regime, all networks, except for the two highest concentrated $z = 6$ networks, displayed resolvable strain hardening until yielding (Fig. B.8). The hardening response of such networks are well fit by

$G' \sim \exp\left((\gamma/\gamma^*)^2\right)$, where γ^* is the characteristic strain at which stiffening occurs [89–91] (see section B.7.2).

We observed that both the torque amplitude and radial displacement (*i.e.*, strain) amplitude time-trace were continuous at yielding (Fig. B.9), consistent with rheometer plates maintaining contact to an elastic material. If the plate lost contact with the material at yielding, both traces would appear highly discontinuous and noisy. Further, when separating the plates after strain sweep measurements, both plates had NS solutions adhered to them. All of this evidence confirms there was no plate slippage during strain sweep measurements.

B.7.2 Characteristic and yield strain

The non-linear elastic response of nearly all DNAns networks followed the relation $G'(\gamma) \sim \exp\left((\gamma/\gamma^*)^2\right)$, where γ^* is the characteristic strain at which strain hardening occurs. At a given z, γ^* remained either independent of or slightly increased with [DNAns] (Fig. B.10A). On the other hand, as a function of z, γ^* decreased from $\approx 200\%$ at $z = 3$ to $\approx 110\%$ at $z = 6$ (Fig. B.10A).

Given the digital nature of the non-linearity measurement, we defined the maximum strain, γ_m, as the strain at which $G'(\gamma)$ maximized. Moreover, we defined the error in maximum strain, γ_m, as the resolution of the data sampling. Note that a logarithmic sampling decreases in resolution as strain increases. Accordingly, we report larger errors for strains of greater values. Despite the large uncertainty in our measurement of γ_m, we observed that γ_m remained roughly independent of or slightly decreased with [DNAns] (Fig. B.10B). As a function of z, γ_m decreased from $\approx 170\%$ at $z = 3$ to $\approx 20\%$ at $z = 6$ (Fig. B.10B).

B.7.3 Uniaxial extension ratio calculation

The uniaxial extension ratio, $\lambda_{\max}$, of a polymer chain in a network is related to the characteristic strain of the network by [89]:

$$\gamma^* = \lambda_{\max} - \lambda_{\max}^{-1} \tag{B.6}$$

At a given z, $\lambda_{\max}$ remained roughly independent of or slightly increased with [DNAns] (Fig. B.12). As a function of z, $\lambda_{\max}$ decreased as valence grew: for $z = 3$, 4, and 5, $\lambda_{\max} = 2.3 \pm 0.1, 1.7 \pm 0.1$, and 1.9 ± 0.2, respectively (Fig. B.12). For the lowest concentrated $z = 6$ DNAns network, $\lambda_{\max} = 1.7 \pm 0.2$.

z	Strand	Sequence (5'→3')
All	1	CTACTATGGCGGGTGATAAAAACGGGAAGAGCATGCCCATCCACGATCG
All	2	GGATGGGCATGCTCTTCCCGAACTCAACTGCCTGGTGATACGACGATCG
3	3	CGTATCACCAGGCAGTTGAGAATTTATCACCCGCCATAGTAGACGATCG
4	3	CGTATCACCAGGCAGTTGAGAACATGCGAGGGTCCAATACCGACGATCG
4	4	CGGTATTGGACCCTCGCATGAATTTATCACCCGCCATAGTAGACGATCG
5	4	CGGTATTGGACCCTCGCATGAACCATGCTGGACTCAACTGACACGATCG
5	5	GTCAGTTGAGTCCAGCATGGAATTTATCACCCGCCATAGTAGACGATCG
6	5	GTCAGTTGAGTCCAGCATGGAACGCATCAGTTGCGGCGCCGCACGATCG
6	6	GCGGCGCCGCAACTGATGCGAATTTATCACCCGCCATAGTAGACGATCG

Table B.1: Table of sequences used for each DNAns design. The sticky-end is highlighted in blue and unbound nucleotides are highlighted in red. The sequences here are the same as those used in Chapter 2.

z	$\text{A260}^*_{1\%}$	$100{\cdot}\text{A260}^*_{0.01\%}$	α	Correction to [DNAns]
3	9.4 ± 0.1	11.5 ± 0.3	$30 \pm 6\%$	1.23 ± 0.02
4	13.0 ± 0.2	14.0 ± 0.4	$72 \pm 7\%$	1.09 ± 0.02
5	7.1 ± 0.2	8.5 ± 0.5	$39 \pm 10\%$	1.19 ± 0.04
$^\times 5$	12.6 ± 0.1	13.0 ± 0.1	$89 \pm 20\%$	1.03 ± 0.05
6	15.6 ± 0.6	15.8 ± 0.3	$96 \pm 10\%$	1.01 ± 0.03

Table B.2: Table of $\text{A260}^*_{1\%}$ and $100{\cdot}\text{A260}^*_{0.01\%}$ values as a function of z, along with the calculated percentage of ssDNA present at 1%, α, and the subsequent correction to [DNAns] at 1%. $^\times$This batch of $z = 5$ samples was made several months after the first batch of $z = 5$ samples in order to reproduce mechanical measurements.

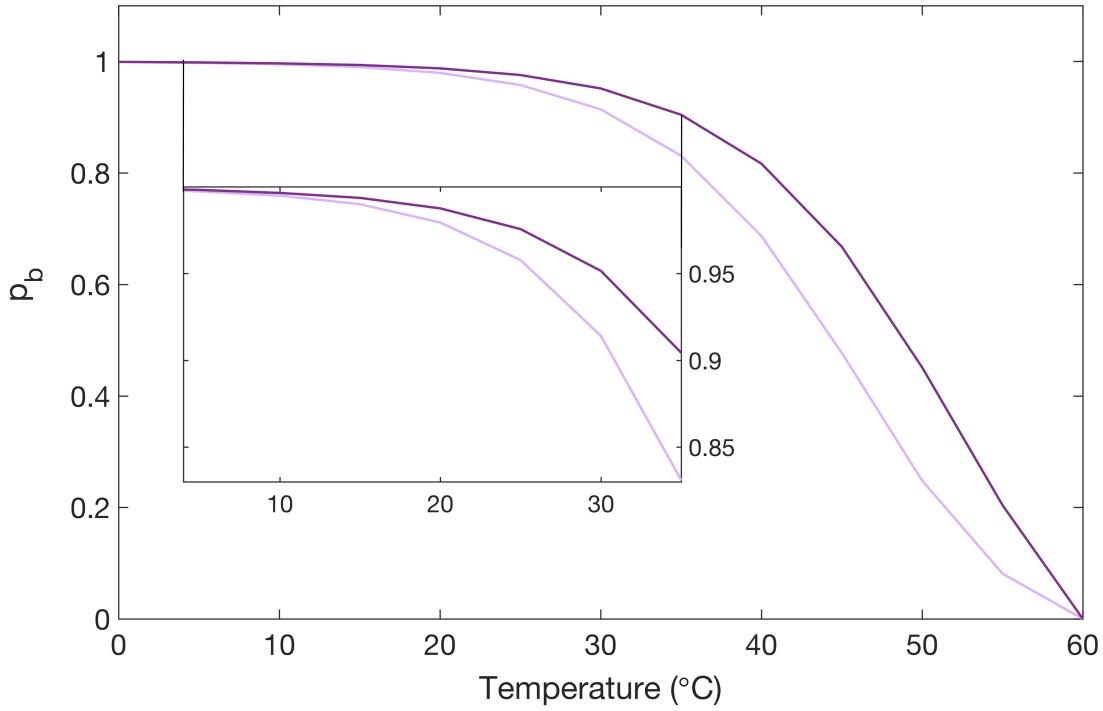

Figure B.1: Binding probability, p_b, of overhang sequence (5'-ACGATCG-3') duplex formation versus temperature at 150 mM NaCl. The light and dark purple line denote [DNAns] = 600 μM/z and [DNAns] = 3600 μM/z, respectively. We note that the p_b reported is normalized to account for the two unbound A's in the DNAns-DNAns overhand bond, which were incorporated in the NUPACK calculation to account for their steric effects on duplex formation.

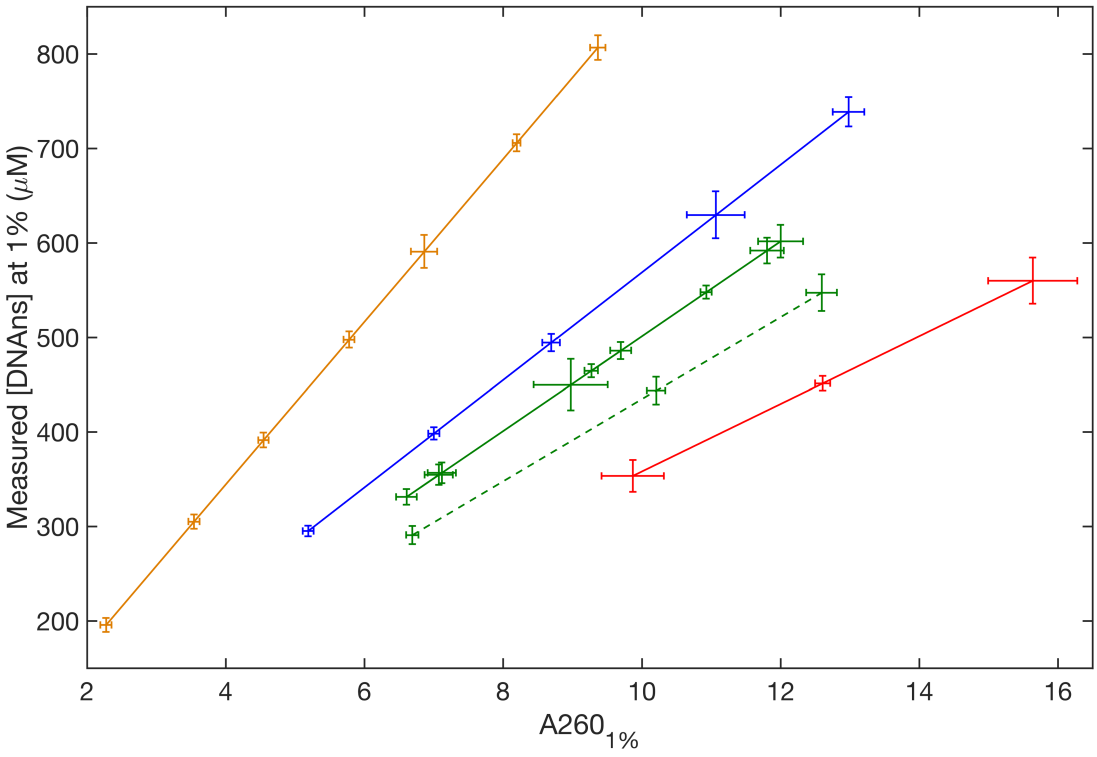

Figure B.2: Plot of measured [DNAns], with applied correction factors shown in Table B.2, as a function of the measured A260 in the 1% dilutions, $A260_{1\%}$. The orange, blue, green, and red denote $z = 3, 4, 5$, and 6, respectively. The lines are not fits, but an interpolated line connecting the data points meant as a guide for the eye. The dashed line denotes the second batch of $z = 5$ samples that was made several months after the first batch of $z = 5$ samples.

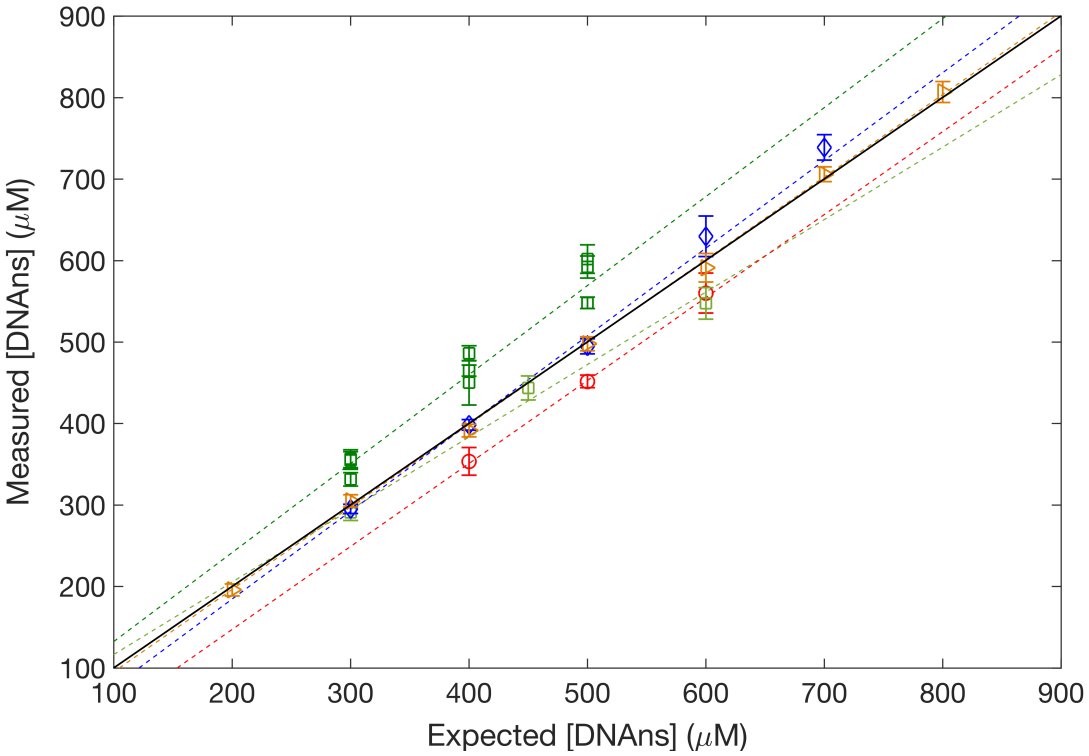

Figure B.3: Plot of measured [DNAns], with applied correction factors shown in Table B.2, as a function of expected [DNAns]. The orange, blue, green, and red denote $z = 3, 4, 5$, and 6, respectively. The $z = 5$ samples colored in the lighter shade of green were made several months after the first batch of $z = 5$ samples (dark green) in order to reproduce mechanical measurements. The dashed lines denote linear fits to the data. The solid, black line denotes the relationship Measured [DNAns] = Expected [DNAns] (*i.e.*, $f(x) = x$).

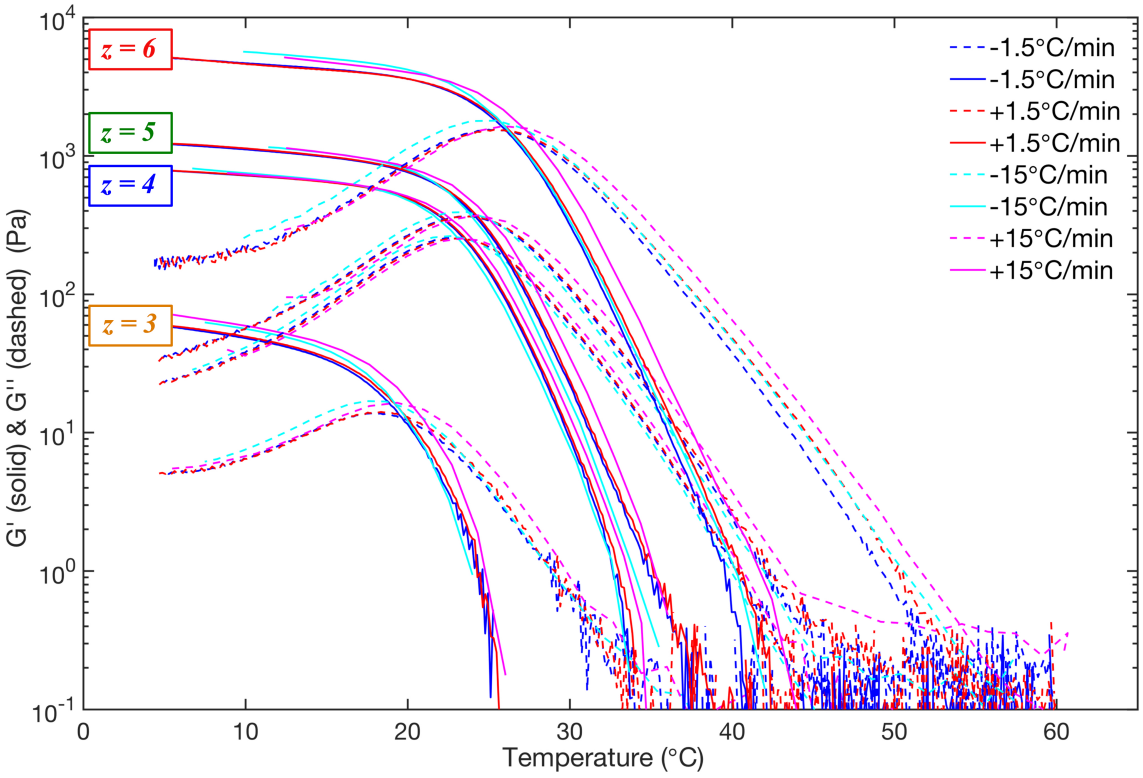

Figure B.4: Log-lin plot of G' and G'' vs. temperature at $\omega = 10$ rad/s and $\gamma = 5\%$ for different rates of cooling and heating (labeled in plot) of a (190 ± 10) μM 3-arm, (290 ± 10) μM 4-arm, (290 ± 10) μM 5-arm, and (360 ± 10) μM 6-arm DNAns solution. The overlap of the curves at different heating and cooling rates show that the viscoelastic response of the DNAns solution is independent of the rate of cooling and heating.

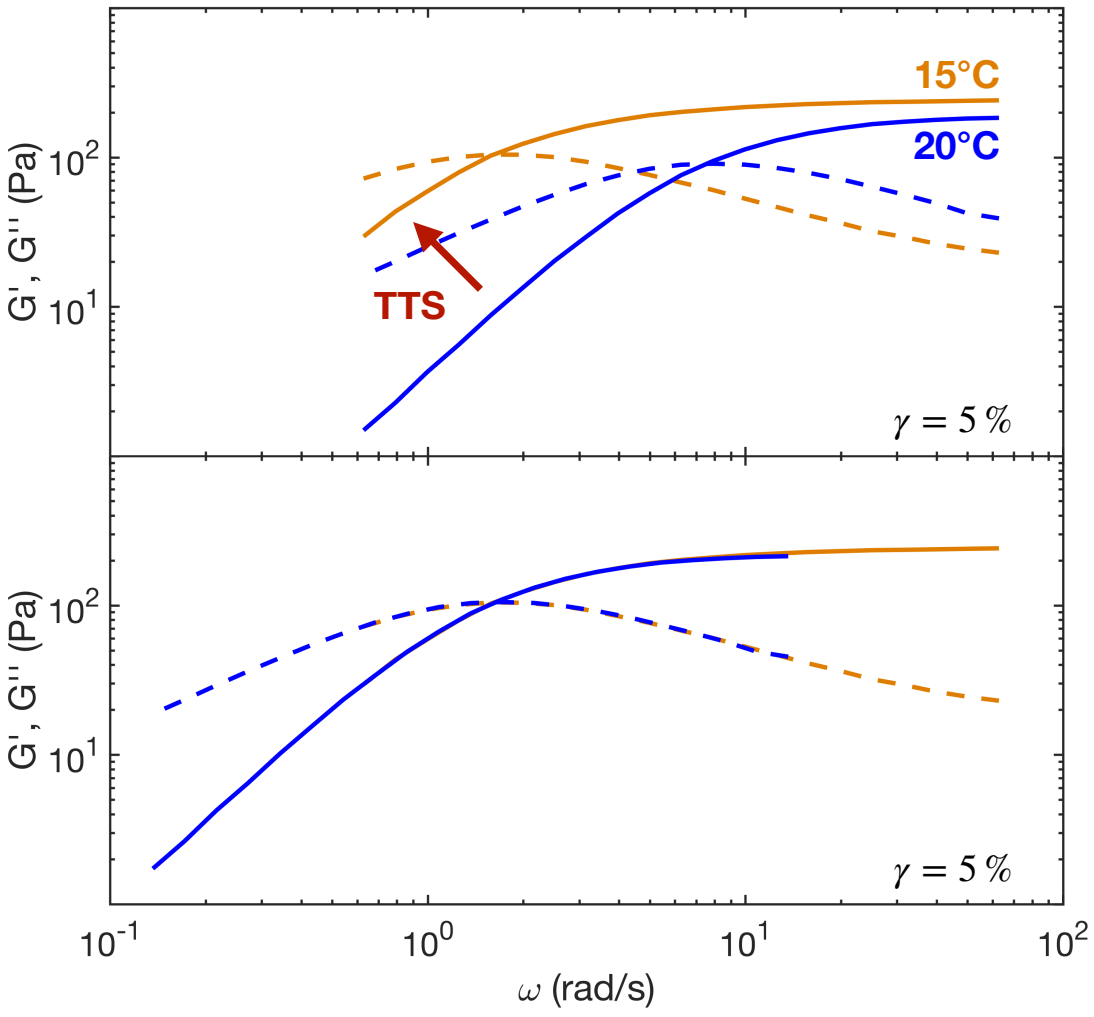

Figure B.5: The top and bottom panels are a log-log plot of $G'(\omega)$ and $G''(\omega)$ pre- and post-TTS, respectively. In this example, the reference temperature is $T_{\text{ref}} = 15°C$. As a note, the data shown is a subset of the $z = 3$ DNAns $G'(\omega)$ and $G''(\omega)$ data.

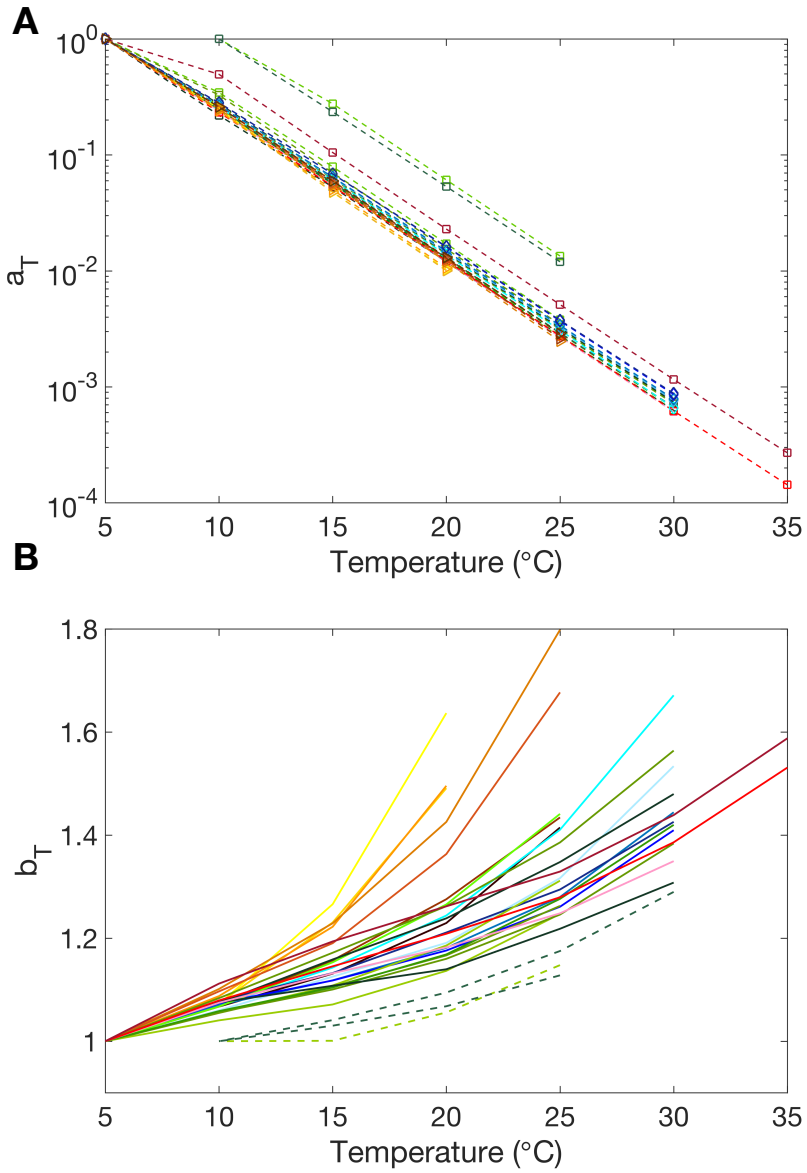

Figure B.6: Log-lin plot of the $T_{\text{ref}} = 5°\text{C}$ (A) horizontal shift factors, a_T, and (B) vertical shift factors, b_T, as a function of temperature. $z = 3, 4, 5$ and 6 are denoted by yellow triangles, blue diamonds, green squares, and red circles, respectively. The lines are guides for the eyes. The darker colored lines signify a higher [DNAns]. The dashed lines denote $z = 5$ samples that were not cooled to $T = 5°\text{C}$.

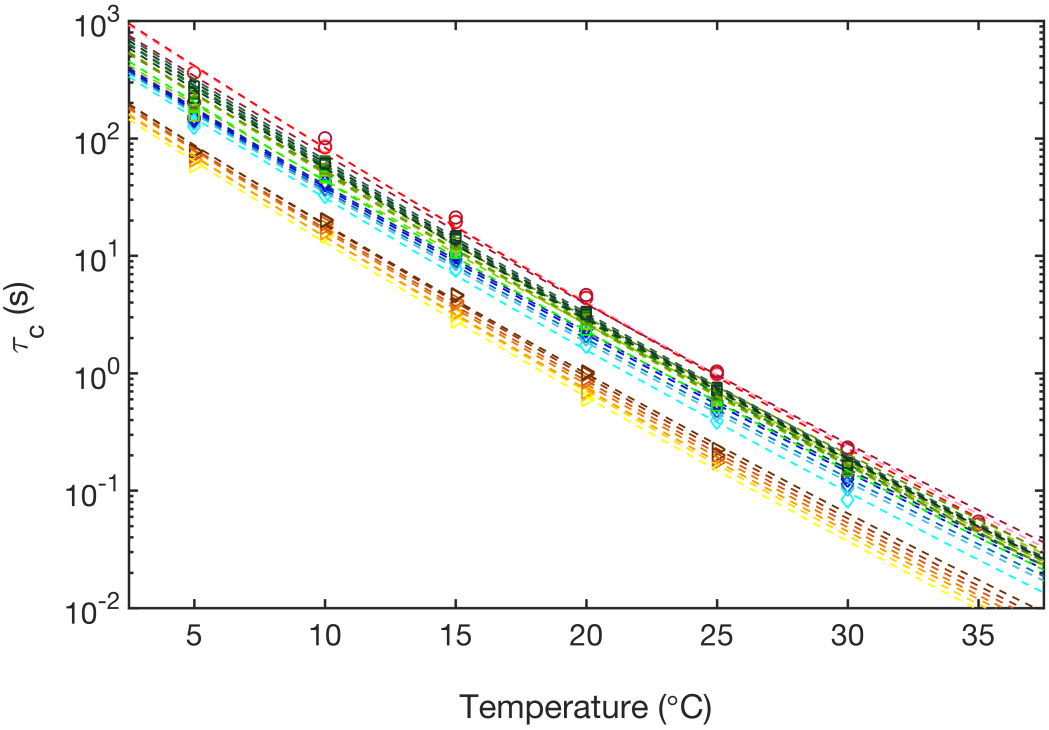

Figure B.7: Log-lin plot of the relaxation time, τ_c, as a function of temperature at $\gamma = 5\%$ for $z = 3$ (yellow triangles), 4 (blue diamonds), 5 (green squares), and 6 (red circles). Darker colors signify a higher [DNAns]. The dashed lines are the Arrhenius fits, $\tau_c \propto \exp(E_A/RT)$.

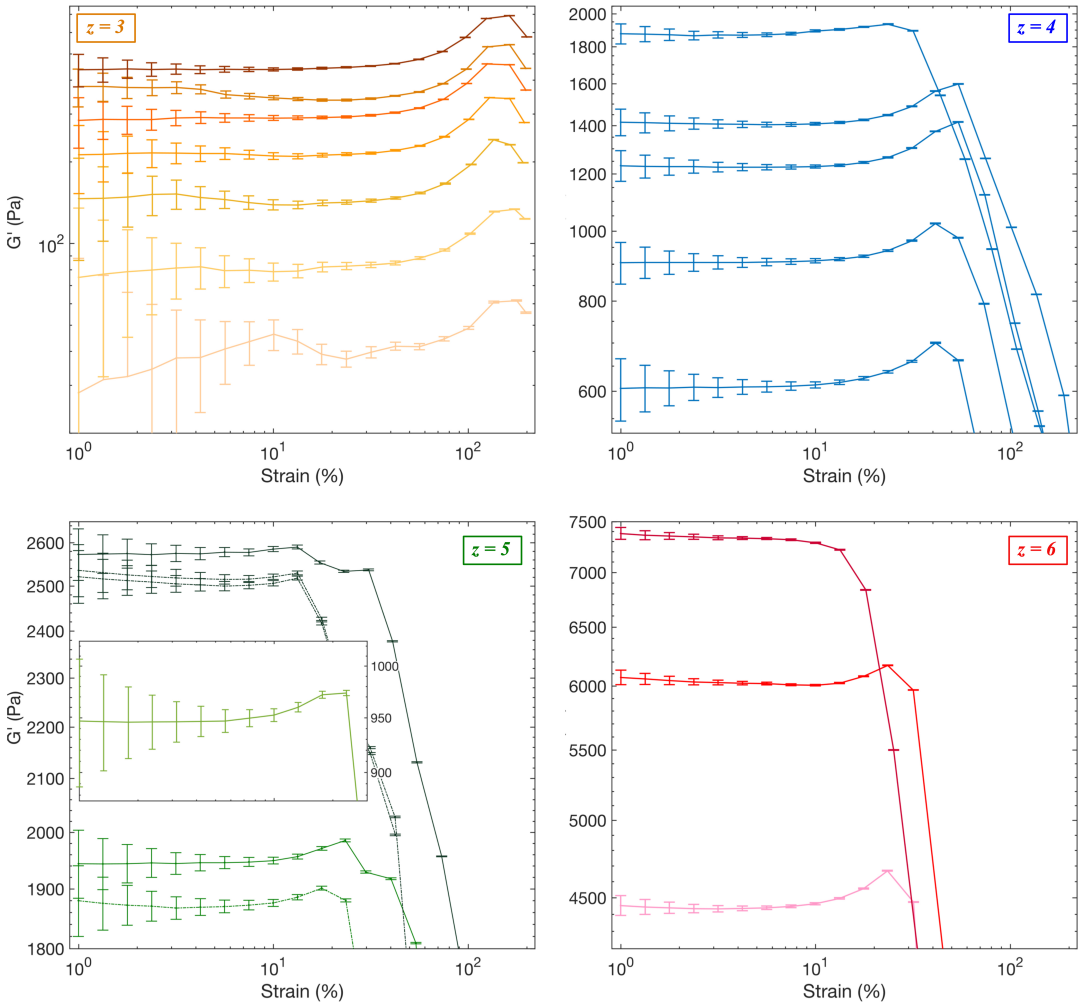

Figure B.8: Log-log plot of the storage modulus, G', as a function of strain, γ, at a temperature of $T = 20°C$ for $z = 3$ (top left panel), 4 (top right panel), 5 (bottom left panel), and 6 (bottom right panel). The curves with darker colors signify a higher [DNAns]. The solid and dash-dot lines denote data taken at a frequency of $\omega = 62.8$ rad/s and $\omega = 125.6$ rad/s, respectively. The inset of the $z = 5$ panel is the lowest concentrated $z = 5$ DNAns network, with $G' \approx 950$ Pa in the linear regime (scale on right of inset).

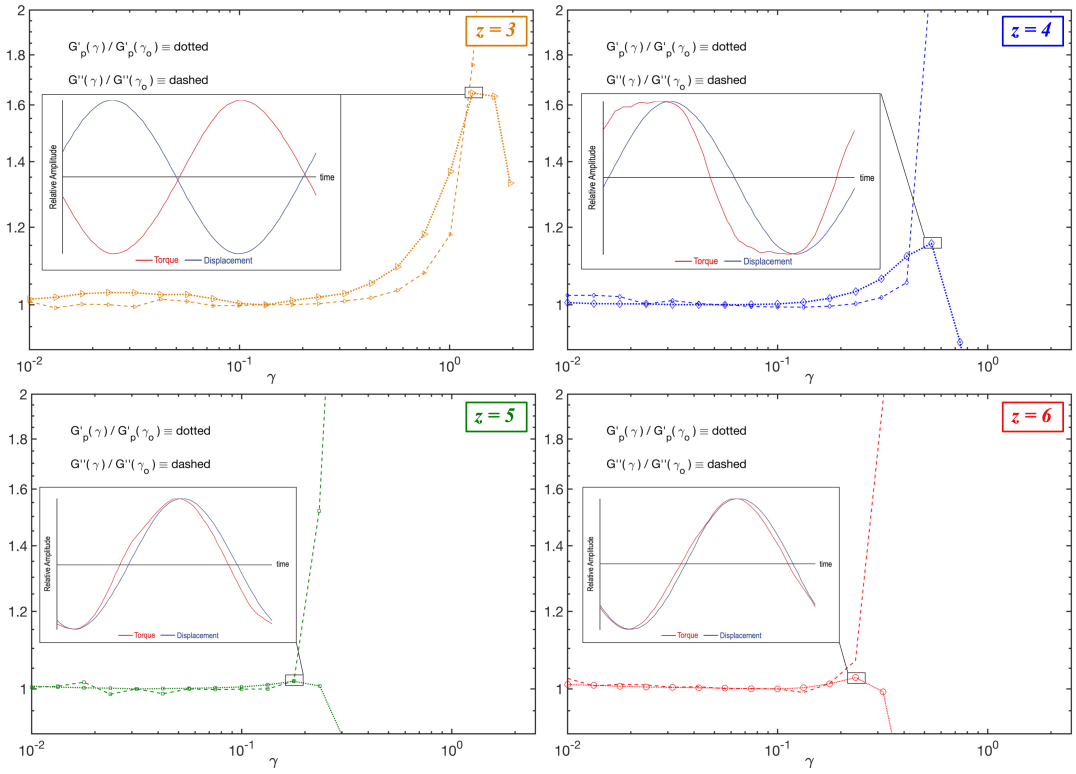

Figure B.9: Log-log plot of the normalized storage, $G'(\gamma)/G'(\gamma_o)$, and loss modulus, $G''(\gamma)/G''(\gamma_o)$ as a function of strain, γ, at a temperature of $T = 20°C$ of $z = 3$ at [DNAns] ≈ 500 μM (top left panel), $z = 4$ at [DNAns] ≈ 500 μM (top right panel), the $z = 5$ gel at [DNAns] ≈ 450 μM (bottom left panel), and $z = 6$ gel [DNAns] ≈ 450 μM (bottom right panel). The insets of each panel show the measured relative amplitude of the torque (red) and radial displacement (blue) wave-forms as a function of time at the point of yielding.

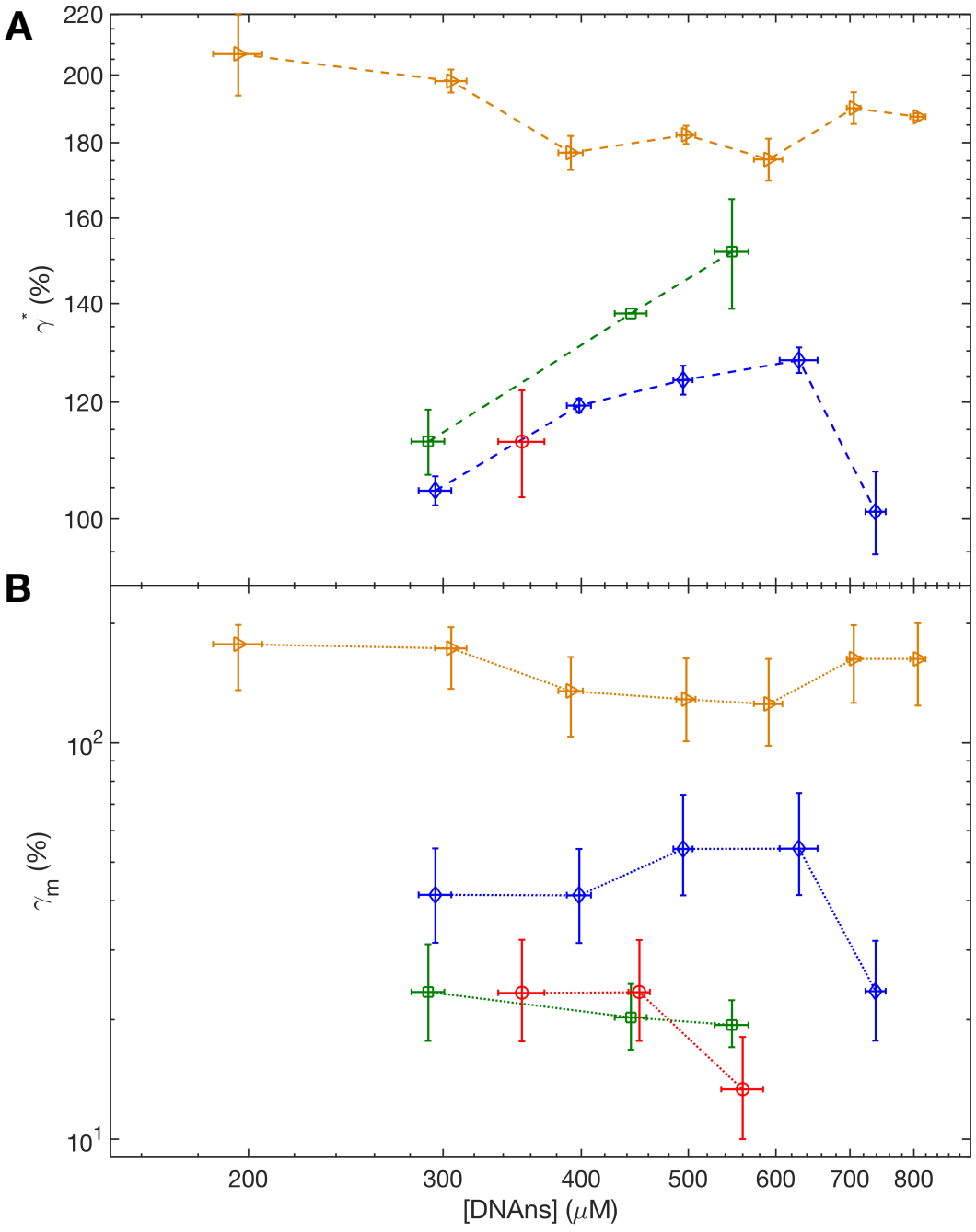

Figure B.10: **(A)** Log-log plot of γ^*, as a function of [DNAns] for z =3 (yellow triangles), 4 (blue diamonds), 5 (green squares), and 6 (red circles) at $T = 20°C$ and $\omega \geq 62.8$ rad/s. **(B)** Log-log plot of γ_m, as a function of [DNAns] for $z = 3$ (yellow triangles), 4 (blue diamonds), 5 (green squares), and 6 (red circles) at $T = 20°C$ and $\omega \geq 62.8$ rad/s. In **(A)** and **(B)**, the dashed and dotted lines are guides for the eye.

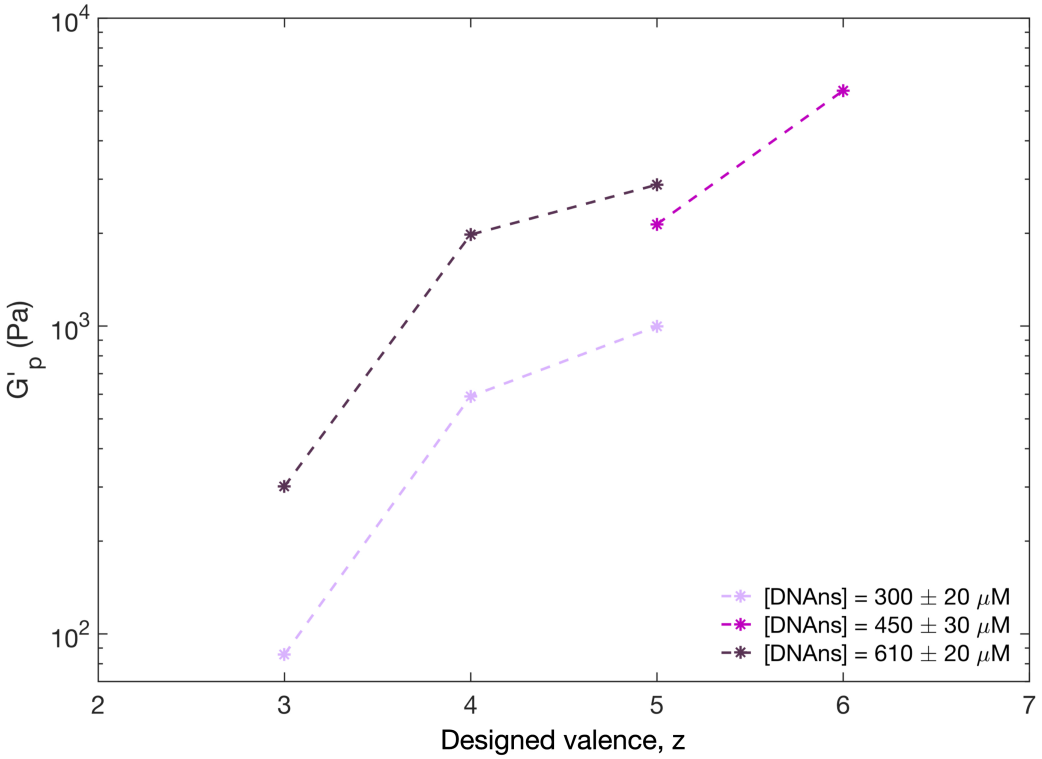

Figure B.11: Log-lin plot of the plateau modulus, G'_p, as a function of designed valence, z, at $T = 20°\text{C}$ and $\gamma = 5\%$. The DNAns concentration of each data set is given in the legend.

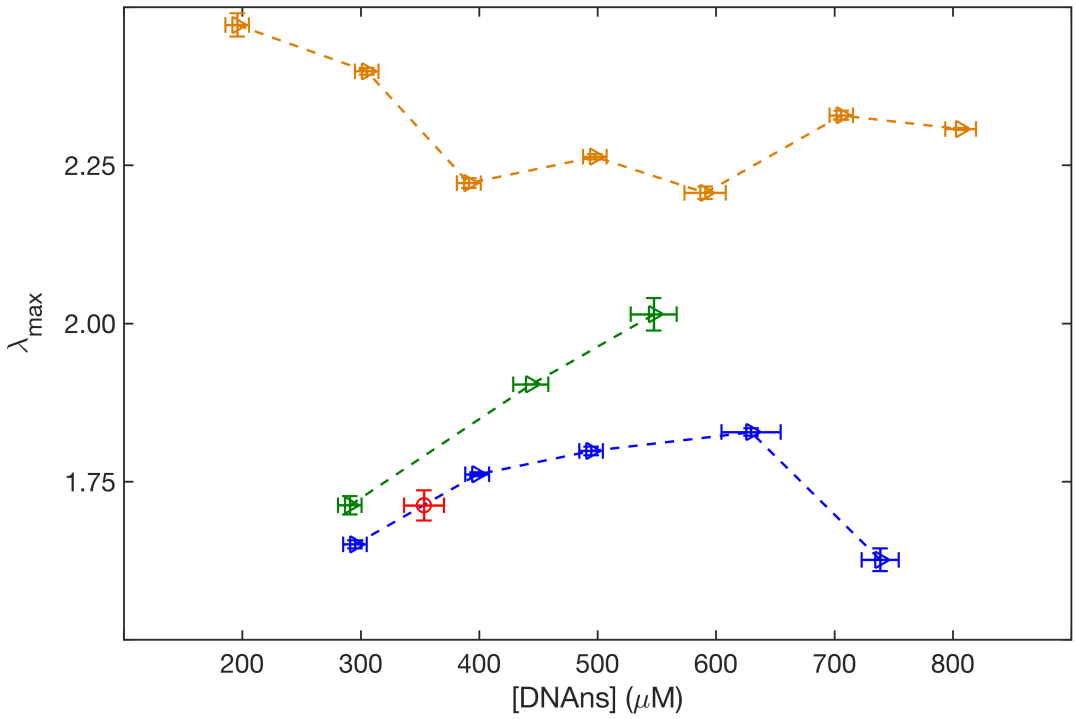

Figure B.12: Plot of λ_{max}, as a function of [DNAns] for $z = 3$ (yellow triangles), 4 (blue diamonds), 5 (green squares), and 6 (red circles) at $T = 20°C$. The dashed lines are guides for the eye.

z	[DNAns] (μM)	ϕ_{rods}	ϕ_{sphere}	G_p' (Pa)
3	195	0.009	0.30	39.5
	305	0.015	0.47	85.6
	390	0.019	0.61	127
	500	0.024	0.77	215
	590	0.029	0.92	301
	705	0.034	1.09	388
	810	0.039	1.25	492
4	295	0.019	0.46	590
	400	0.026	0.62	915
	495	0.032	0.77	1240
	630	0.041	0.98	1460
	740	0.048	1.14	1980
5	290	0.023	0.45	996
	330	0.027	0.51	1370
	355	0.029	0.55	1380
	355	0.029	0.55	1400
	445	0.036	0.69	1940
	450	0.036	0.70	2140
	465	0.037	0.72	2185
	485	0.039	0.75	2140
	550	0.044	0.85	2630
	550	0.044	0.85	2800
	590	0.048	0.91	2820
	600	0.048	0.92	2870
6	350	0.034	0.55	4620
	450	0.044	0.70	5810
	560	0.054	0.87	7450

Table B.3: Correspondence between [DNAns], DNAns volume fraction ϕ, and G_p'. ϕ is calculated in two ways: (i) ϕ_{rods} assumes the DNAns is composed of z rods, with each rod having a length given by the dsDNA arm length (8.5 nm, which includes half the sticky end) and radius (1 nm); and (ii) ϕ_{sphere} gives the volume fraction of a monodisperse system of spheres of concentration [DNAns], with the sphere radius set to the DNAns arm length (8.5 nm). ϕ_{sphere} is useful in gaining intuition on system structure through comparision to volume fractions of, *e.g.*, FCC or random-sphere packings [152, 153].

Appendix C

Appendix for Chapter 4 and 5

C.1 NS Design

All z-arm NSs used in chapter 4 and 5 (shown in Figure 5.1B) self-assemble from z complementary ssDNA oligos (see Fig. C.1). NSs self-assemble into z-armed star-like structures, with neighboring arms connected at the core by two unpaired Adenosines (A). Here, we design the tips of the NS arms to be either blunted or have a self-complementary ssDNA "sticky-end" sequence mediating NS-NS bonds (Fig. 5.1B). The three sticky-end sequences used here are: α sticky-end 5'-ACGATCG-3', β sticky-end 5'-ATGCATGCA-3', and γ sticky-end 5'-ATGCGCGCA-3'. The unpaired A preceding the core self-complementary portions of the sticky-end promote flexibility [13, 27].

Lastly, for all sticky-end types, we design the sequences assembling NSs to ensure that two bound NS arms are separated junction-to-junction by 50 nucleotides in length. In particular, we made: (i) an "α" NS arm to be a 20 base-pair (bp) dsDNA segment ending in a 7 nt-long sticky-end 5'-ACGATCG-3' (ii) a "β" (or "γ") NS arm to be a 19 bp dsDNA segment ending in a 9 nt-long sticky-end 5'-ATGCATGCA-3' (or 5'-ATGCGCGCA-3' for γ). A NS arm without a α or β/γ sticky-end was designed to be just a 19 or 20 bp dsDNA segment, respectively.

C.2 NS preparation

HPLC purified ssDNA oligos were purchased from IDTDNA in a dehydrated state. Upon receiving, oligos were hydrated to ≈ 500 μM of MilliQ water. Constituent oligos forming the various z-arm NSs, as shown in Figure 5.1A, were then mixed together in stoichiometric amounts to make ≈ 400 to 470 μM worth of NSs. To achieve such NS concentrations, the mixed oligos required completely dehydration and then re-hydration in 100 μL of a buffer-saline solution (40 mM Tris, 10.5 mM HCl, 1 mM EDTA and monovalent salt concentration of choice). The newly rehydrated NS solution was then thermally annealed by heating them to 95°C for 20 mins in an insulated, dry heat block (Make, Model) and then cooling to room temperature over ≈ 5 hours. After annealing, the samples were immediately used for concentration measurements and then stored in the fridge (4-6°C) for a few days before rheology measurements.

C.3 Concentration measurement procedure and estimates

Aliquots of constituent ssDNA oligo stocks or NS solutions were diluted 100-fold in MilliQ water for concentration measurements. To ensure NSs fully disassemble after the dilution step, we heat them to 90°C for ≈ 60 s and vortex the heated solution vigorously for ≈ 10 s. The heated NS dilutions are then placed on an empty pipette rack to cool to room temperature. All dilutions are vortexed once more prior to concentration measurements.

The concentration, c, of ssDNA stock or NS solutions were then estimated from UV spectroscopy measurements (Fisher Scientific, Nanodrop 2000c) of the corresponding diluted solution. In particular, c was calculated from the absorbance at 260 nm, A_{260},

using Beer-Lambert's Law $c = 100A_{260}/(\epsilon l)$, where the factor of 100 accounts for the dilution step, l (= 1 cm) is the optical path length, and ϵ is the extinction coefficient of the strand or NS (see Table C.1 for ϵ values). For NSs, we estimate their ϵ as the sum of its constituent ssDNA sequences.

C.4 Oscillatory Rheology

We performed oscillatory shear rheology on NS solutions in a parallel, flat-plate geometry using a strain- and temperature-controlled rheometer (TA Instruments, Ares-G2). The bottom plate was a temperature-controlled plate that applied strain, λ, to solutions. The top plate was a steel plate of radius $r = 10$ mm through which the resulting transmitted stress, σ, was monitored.

NS solutions were placed onto the bottom plate of the rheometer at room temperature by shoveling $\approx$ 80 to 90 μL of solution out of their respective tubes using a slant cut 1000 μL pipette tip. A few NS solutions (e.g., valence 3, 4, and 5 solutions) were pipetted directly onto the bottom plate after heating them to 65°C for $\approx$ 5 minutes. After the solution was loaded onto the bottom plated, it was then sandwiched until the top and bottom plates were separated by a gap size of $g \approx 0.18 - 0.22$ mm. A low-viscosity mineral oil (Fisher Scientific, 162 Saybolt Viscosity $\approx$ 0.034 Pa s) was placed over the exposed sample to prevent evaporation during measurements.

Before the NS solutions were sheared, they were quickly annealed between the two plates. Solutions were heated to a temperature above the sticky-end melting temperature (65°C for solutions with α- or β-bonds and 70°C for γ-bond solutions) for $\approx$ 5 minutes. The temperature was lowered at a rate of $|dT/dt| \sim 1$°C between set temperatures.

First, the linear response regime and yield behavior of NS solutions were investigated. In particular, the storage, G', and loss, G'', moduli were measured over a range over

strains, 1%$\leq \lambda \leq$300%, at many different temperatures and applied frequencies. The homotypic NSs with weak or strong sticky-ends typically had a set temperature of 20 or 40-50°C, respectively. The heterotypic NSs, on the other hand, had set temperatures between 20°C$\leq T \leq$ 45°C. For all NS types, the applied frequency of deformation during the strain sweep was 2.5, 5, 7.5 or 10 Hz. A few samples were measured at 0.3 and 1 Hz.

Next, oscillatory shear flow measurements of G' and G'' were performed on NS solutions in their linear response regime ($\lambda = 1, 5\%$) between shearing frequencies of 0.1 Hz $\leq f \leq$10 Hz (over 30 logarithmically spaced points). $G'(f)$ and $G''(f)$ were measured over a range of temperatures (5°C$\leq T \leq$ 55°C) in 5°C increments. Each $G'(f,T)$ and $G''(f,T)$ were then used to construct the "master curves" of the frequency-dependent stress-response at a reference temperature of T = 25°C (Fig. 4.1-4.2 & 5.1-5.5). The time-temperature superposition protocol followed is detailed in Appendix BB.6.2.

When separating the plates after rheology measurements, we found the NS samples were stuck to both the top and bottom plates. This indicated to us that NS solutions strongly adhered to both plates and, thus, there was no plate slippage during measurements.

C.5 Two-mode Maxwell viscoelastic spectra

The storage modulus and loss modulus are:

$$G' = G'_{p,1}\frac{(f/\tau_1)^2}{1+(f/\tau_1)^2} + G'_{p,2}\frac{(f/\tau_2)^2}{1+(f/\tau_2)^2} \tag{C.1}$$

$$G'' = G'_{p,1}\frac{(f/\tau_1)}{1+(f/\tau_1)^2} + G'_{p,2}\frac{(f/\tau_2)}{1+(f/\tau_2)^2} \tag{C.2}$$

NS	[NS] (μM)	[NaCl] (mM)	E_a (kJ/mol)	ΔH_{SL} (kJ/mol)	ΔS_{SL} (J/(mol K))
$\alpha_3 x_3$	460 ± 9	50	213 ± 6	-235	-704
$x_3\gamma_3$	423 ± 9	50	251 ± 11	-306	-842
$\alpha_3\gamma_3^*$	439 ± 11	50	239 ± 5	-306	-842
$\alpha_3 x_3$	440 ± 10	150	207 ± 1	-235	-686
$x_3\gamma_3$	460 ± 20	150	254 ± 8	-306	-820
$\alpha_3\gamma_3^*$	440 ± 9	150	249 ± 6	-306	-820
$\alpha_3 x_3$	432 ± 10	300	204 ± 4	-235	-674
$\alpha_4 x_2$	406 ± 9	300	210 ± 6	-235	-674
α_6^*	430 ± 7	300	225 ± 2	-235	-674
β_3	474 ± 11	300	237 ± 5	-277	-753
$\alpha_3\beta_3^*$	412 ± 6	300	247 ± 5	-277	-753
$\alpha_3\gamma_2^*$	422 ± 11	300	247 ± 4	-306	-807
$\alpha_4\gamma_2^*$	411 ± 6	300	249 ± 5	-306	-807
γ_3	534 ± 17	300	254 ± 8	-306	-807
$x_3\gamma_3$	452 ± 10	300	245 ± 7	-306	-807
$\alpha_3\gamma_3^*$	447 ± 7	300	241 ± 5	-306	-807
γ_4	468 ± 10	300	263 ± 7	-306	-807
$\alpha_2\gamma_4^*$	450 ± 7	300	250 ± 8	-306	-807

Table C.1: Measured activation energies, E_a, and estimated enthalpy, ΔH, for the sticky-ends used in this study. The various NS and salt concentration used for each sample are listed in the second and third columns, respectively. The columns with an '$*$' means the reported [NS] and E_a are averages of several NS samples. We note E_a was measured from Arrhenius fits to τ_c vs temperature (Fig. C.3). Further, the estimate for the sticky-end ΔS_{SL} and ΔH_{SL} was calculated using the nearest-neighbor DNA thermodynamic model detailed in SantaLucia [59], with two added corrections. In particular, we added a dangle correction from the unpaired "A" preceding the core binding sequences and an empirical "tail" correction [60] estimating the repulsion from the DNA arms flanking the sticky-end.

Name of strand	Sequence (5′-3′)	Extinction coefficient (L/(mole·cm))
V1α_3	CTACTATGGCGGGTGATAAAAACGGGAAGAGCATGCCCATCCACGATCG	484100
V2α_3	GGATGGGCATGCTCTTCCCGAACTCAACTGCCTGGTGATACGACGATCG	458900
S3α_3	CGTATCACCAGGCAGTTGAGAATTTATCACCCGCCATAGTAGACGATCG	480500
V1β_3	CTACTATGGCGGGTGATAAAAGGGAAGAGCATGCCCATCCATGCATGCA	484900
V2β_3	GGATGGGCATGCTCTTCCCAATCAACTGCCTGGTGATACGATGCATGCA	461800
S3β_3	CGTATCACCAGGCAGTTGAAATTATCACCCGCCATAGTAGATGCATGCA	480700
V1γ_3	CTACTATGGCGGGTGATAAAAGGGAAGAGCATGCCCATCCATGCGCGCA	480700
V2γ_3	GGATGGGCATGCTCTTCCCAATCAACTGCCTGGTGATACGATGCGCGCA	457600
S3γ_3	CGTATCACCAGGCAGTTGAAATTATCACCCGCCATAGTAGATGCGCGCA	476500
V1γ_4	CTACTATGGCGGGTGATAAAAGGGAAGAGCATGCCCATCCATGCGCGCA	480700
V2γ_4	GGATGGGCATGCTCTTCCCAATCAACTGCCTGGTGATACGATGCGCGCA	457600
V3γ_4	CGTATCACCAGGCAGTTGAAAATGCGAGGGTCCAATACCGATGCGCGCA	479800
S4γ_4	CGGTATTGGACCCTCGCATAATTATCACCCGCCATAGTAGATGCGCGCA	467000
V1$\boldsymbol{\alpha_3}\gamma_3$	CTACTATGGCGGGTGATAAAACGGGAAGAGCATGCCCATCCACGATCG	472100
V2$\alpha_3\gamma_3$	GGATGGGCATGCTCTTCCCGAATCAACTGCCTGGTGATACGATGCGCGCA	468100
V3$\boldsymbol{\alpha_3}\gamma_3$	CGTATCACCAGGCAGTTGAAACATGCGAGGGTCCAATACCGACGATCG	472000
V4$\alpha_3\gamma_3$	CGGTATTGGACCCTCGCATGAACATGCTGGACTCAACTGACATGCGCGCA	470700
V5$\boldsymbol{\alpha_3}\gamma_3$	GTCAGTTGAGTCCAGCATGAACGCATCAGTTGCGGCGCCGCACGATCG	455400
S6$\alpha_3\gamma_3$	GCGGCGCCGCAACTGATGCGAATTATCACCCGCCATAGTAGATGCGCGCA	474500
V1$\mathbf{x}_3\gamma_3$	CTACTATGGCGGGTGATAAAACGGGAAGAGCATGCCCATCC	402700
V2$\alpha_3\mathbf{x}_3$	GGATGGGCATGCTCTTCCCGAATCAACTGCCTGGTGATACG	383400
V3$\mathbf{x}_3\gamma_3$	CGTATCACCAGGCAGTTGAAACATGCGAGGGTCCAATACCG	402700
V4$\alpha_3\mathbf{x}_3$	CGGTATTGGACCCTCGCATGAACATGCTGGACTCAACTGAC	385900
V5$\mathbf{x}_3\gamma_3$	GTCAGTTGAGTCCAGCATGAACGCATCAGTTGCGGCGCCGC	386000
S6$\alpha_3\mathbf{x}_3$	GCGGCGCCGCAACTGATGCGAATTATCACCCGCCATAGTAG	389800
V1$\boldsymbol{\alpha_3}\gamma_2$	CTACTATGGCGGGTGATAAAAACGGGAAGAGCATGCCCATCCACGATCG	484100
V2$\alpha_3\boldsymbol{\gamma_2}$	GGATGGGCATGCTCTTCCCGAATCAACTGCCTGGTGATACGATGCGCGCA	468100
V3$\boldsymbol{\alpha_3}\gamma_2$	CGTATCACCAGGCAGTTGAAACATGCGAGGGTCCAATACCGACGATCG	472000
V4$\alpha_3\boldsymbol{\gamma_2}$	CGGTATTGGACCCTCGCATGAACATGCTGGACTCAACTGACATGCGCGCA	470700
V5$\boldsymbol{\alpha_3}\gamma_2$	GTCAGTTGAGTCCAGCATGAATTTATCACCCGCCATAGTAGACGATCG	469700
V1$\alpha_4\gamma_2$	CTACTATGGCGGGTGATAAAAAGGGAAGAGCATGCCCATCCATGCGCGCA	492700
V2$\boldsymbol{\alpha_4}\gamma_2$	GGATGGGCATGCTCTTCCCAACTCAACTGCCTGGTGATACGACGATCG	448400
V3$\boldsymbol{\alpha_4}\gamma_2$	CGTATCACCAGGCAGTTGAGAACATGCGAGGGTCCAATACCGACGATCG	483300
V4$\alpha_4\boldsymbol{\gamma_2}$	CGGTATTGGACCCTCGCATGAACATGCTGGACTCAACTGACATGCGCGCA	470700
V5$\boldsymbol{\alpha_4}\gamma_2$	GTCAGTTGAGTCCAGCATGAACGCATCAGTTGCGGCGCCGCACGATCG	455400
S6$\alpha_4\gamma_2$	GCGGCGCCGCAACTGATGCGAATTTATCACCCGCCATAGTAGACGATCG	467200
V1$\alpha_4\mathbf{x}_2$	CTACTATGGCGGGTGATAAAAAGGGAAGAGCATGCCCATCC	407900
V2$\boldsymbol{\alpha_4}\gamma_2$	GGATGGGCATGCTCTTCCCAACTCAACTGCCTGGTGATACGACGATCG	448400
V3$\boldsymbol{\alpha_4}\gamma_2$	CGTATCACCAGGCAGTTGAGAACATGCGAGGGTCCAATACCGACGATCG	483300
V4$\alpha_4\mathbf{x}_2$	CGGTATTGGACCCTCGCATGAACATGCTGGACTCAACTGAC	385900
V5$\boldsymbol{\alpha_4}\gamma_2$	GTCAGTTGAGTCCAGCATGAACGCATCAGTTGCGGCGCCGCACGATCG	455400
S6$\boldsymbol{\alpha_4}\gamma_2$	GCGGCGCCGCAACTGATGCGAATTTATCACCCGCCATAGTAGACGATCG	467200
V1$\alpha_2\gamma_4$	CTACTATGGCGGGTGATAAAAAGGGAAGAGCATGCCCATCCATGCGCGCA	492700
V2$\alpha_2\gamma_4$	GGATGGGCATGCTCTTCCCAATCAACTGCCTGGTGATACGATGCGCGCA	457600
V3$\boldsymbol{\alpha_4}\gamma_2$	CGTATCACCAGGCAGTTGAAACATGCGAGGGTCCAATACCGACGATCG	472000
V4$\alpha_2\gamma_4$	CGGTATTGGACCCTCGCATGAACATGCTGGACTCAACTGACATGCGCGCA	470700
V5$\alpha_2\gamma_4$	GTCAGTTGAGTCCAGCATGAACGCATCAGTTGCGGCGCCGATGCGCGCA	464600
S6$\boldsymbol{\alpha_4}\gamma_2$	CGGCGCCGCAACTGATGCGAATTTATCACCCGCCATAGTAGACGATCG	457000
V1$\boldsymbol{\alpha_3}\gamma_3$	CTACTATGGCGGGTGATAAAACGGGAAGAGCATGCCCATCCACGATCG	472100
V2$\alpha_3\boldsymbol{\beta_3}$	GGATGGGCATGCTCTTCCCGAATCAACTGCCTGGTGATACGATGCATGCA	472300
V3$\boldsymbol{\alpha_3}\gamma_3$	CGTATCACCAGGCAGTTGAAACATGCGAGGGTCCAATACCGACGATCG	472000
V4$\alpha_3\boldsymbol{\beta_3}$	CGGTATTGGACCCTCGCATGAACATGCTGGACTCAACTGACATGCATGCA	474900
V5$\boldsymbol{\alpha_3}\gamma_3$	GTCAGTTGAGTCCAGCATGAACGCATCAGTTGCGGCGCCGCACGATCG	455400
S6$\alpha_3\boldsymbol{\beta_3}$	GCGGCGCCGCAACTGATGCGAATTATCACCCGCCATAGTAGATGCATGCA	478700

Figure C.1: Sequences for the ssDNA strands used to self-assemble the "a_z" homotypic and "$a_p b_q$" heterotypic NSs. The α sticky-end sequence used here is the same sequence shown in Table A.1. Text file of sequences available upon request.

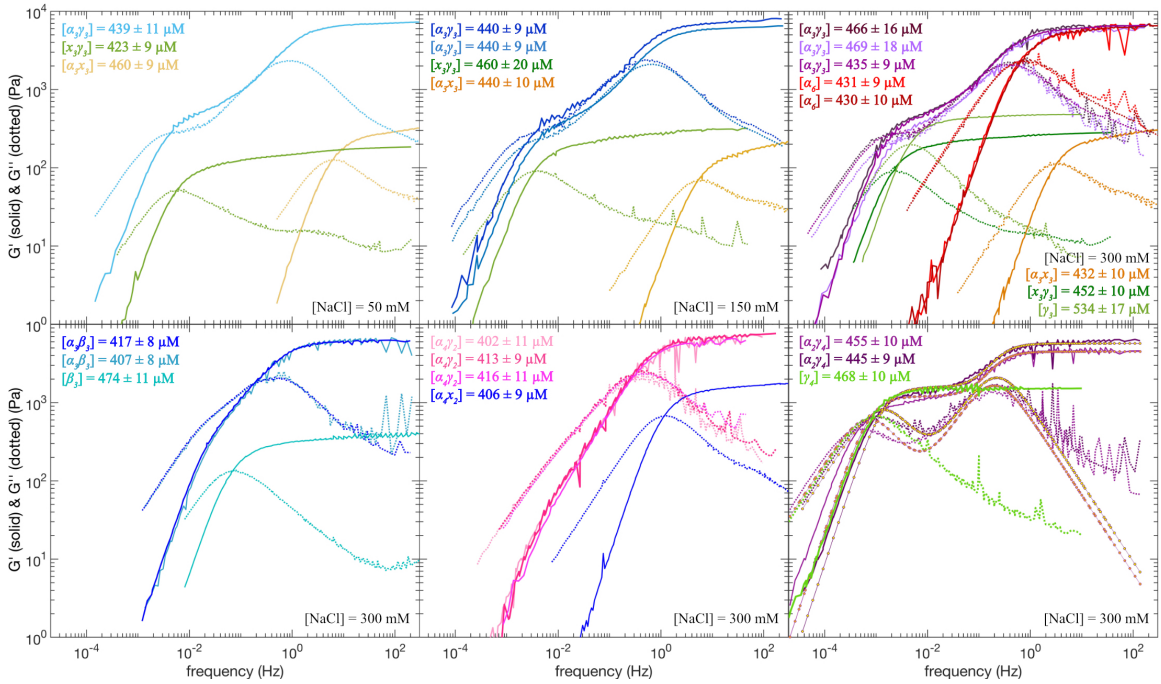

Figure C.2: Master curve plots of G' and G'' versus frequency of various NS solutions at a reference temperature of 25°C. All heterotypic NSs were measured at 1% strain, whereas the valence 3 and 4 homotypic NSs were measured at 5% strain. The concentrations of NSs used in each sample are listed in the legends of the plots.

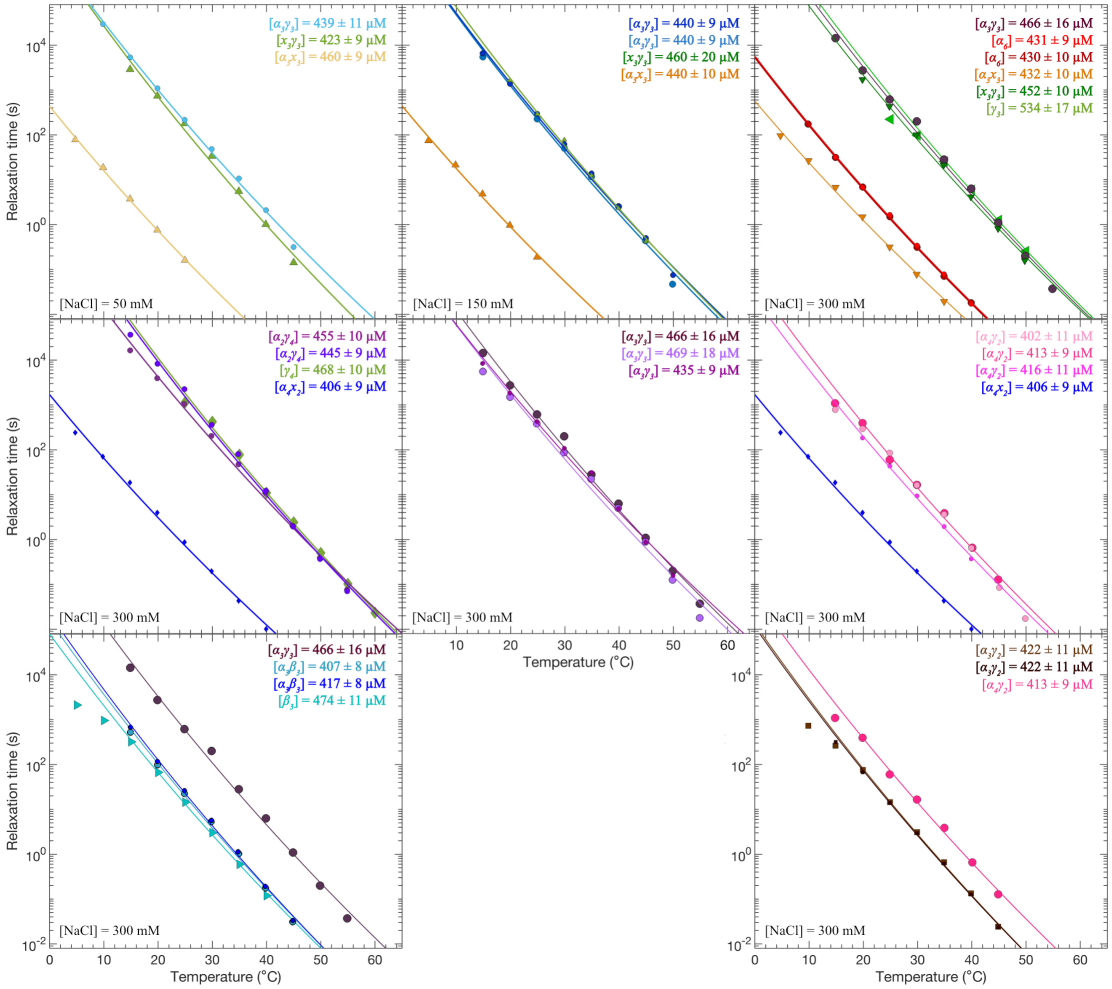

Figure C.3: Plots of relaxation time versus temperature of various NS solutions. For all master curves with a clear crossover in G' and G'' following the terminal fluid regime, we estimate the liquid-like relaxation time for those solutions from the inverse of the crossover frequency and plot those here. A few heterogeneous NS solutions, however, transitioned from a liquid-like regime to a power-law regime without a crossover in G' and G'' (e.g., $\alpha_3\beta_3, \alpha_3\gamma_2$, and $\alpha_4\gamma_2$ NSs), preventing a direct measurement of the relaxation time for simple fluid-flow, τ_{liq}. We estimated $1/\tau_{liq}$ in those networks by finding the frequency at which the terminal fits of $G' = A_1 f^2$ and $G'' = A_2 f$ become equal (*i.e.*, $f_c = A_2/A_1 = 1/\tau_{liq}$). We are reporting those estimates of τ_{liq} here. Lastly, note that solid lines denote Arrhenius fits to the relaxation time and that the concentrations of NSs and added salt used in each sample are listed in the legends of the plots.

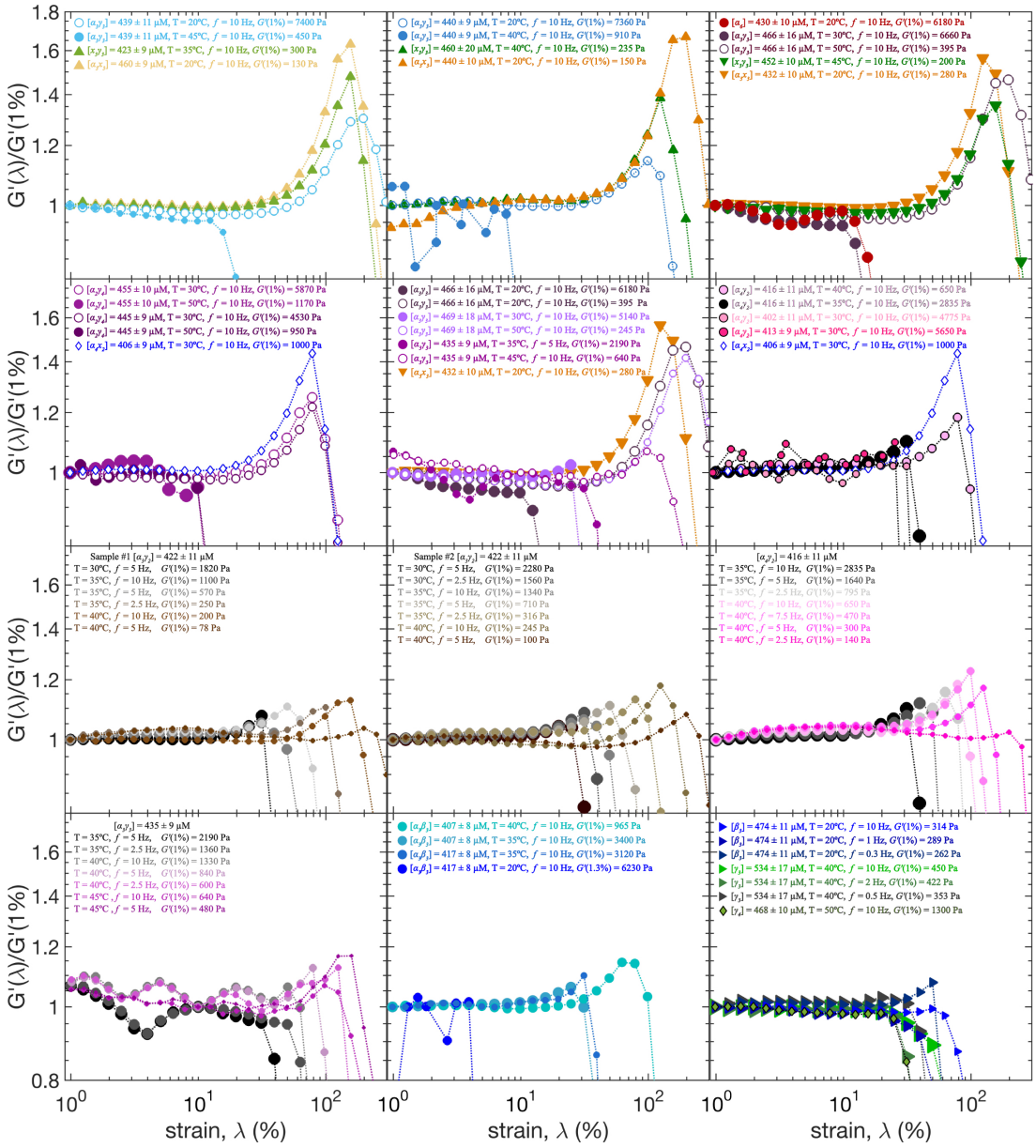

Figure C.4: Plots of normalized storage modulus versus strain of various NSs. The top row are $\alpha_3\gamma_3$, $\alpha_3 x_3$, $x_3\gamma_3$, and α_6 NSs, all made at roughly the same NS concentrations, hydrated in different salt concentrations (left - 50 mM NaCl, middle - 150 mM NaCl, right - 300 mM NaCl). The second row are the $\alpha_2\gamma_4$, $\alpha_3\gamma_3$, and $\alpha_2\gamma_4$ NSs done at shearing rates slightly above the γ-network relaxation rate, in between the relaxation rates of both networks, and far into the elastic regime. The third row and first plot of row four show changes to the strain response of the $\alpha_3\gamma_2$, $\alpha_2\gamma_4$, and $\alpha_3\gamma_3$ NSs as temperature and shearing frequency are changed. The last plots of row four are the $\alpha_3\beta_3$ NS (middle) and β_3, γ_3, γ_4 NSs (right) at conditions far into the elastic regime. All NSs solutions of rows two to four had [NaCl] = 300 mM.

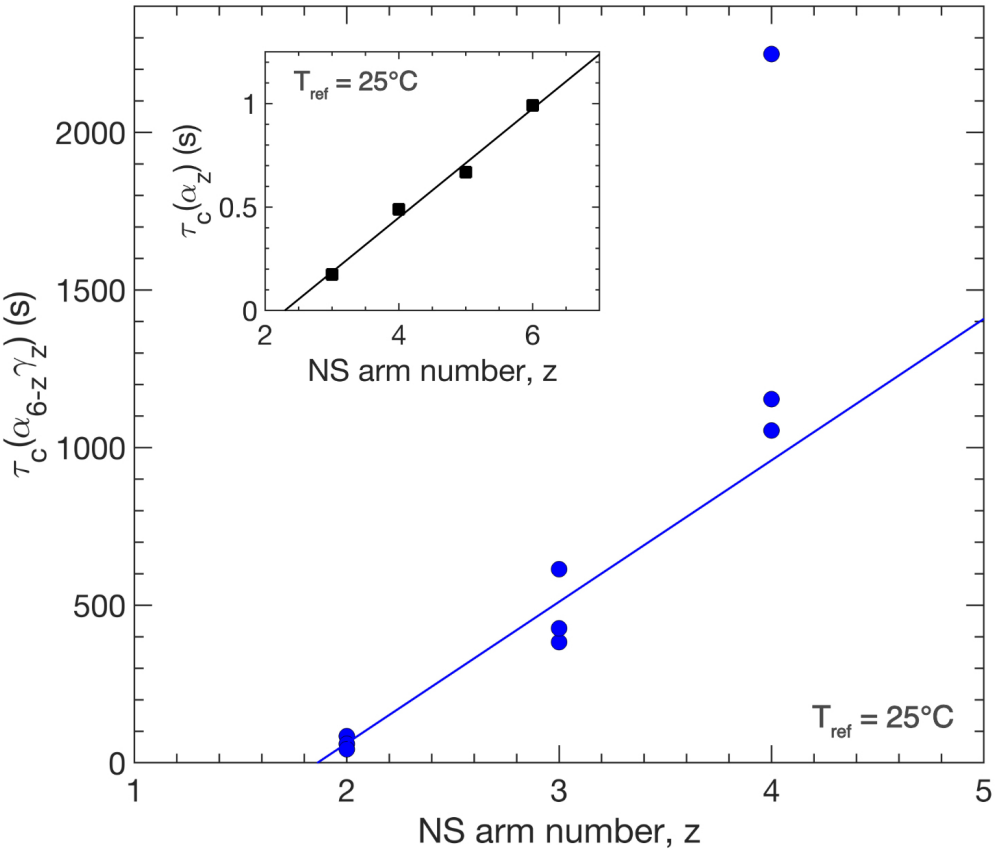

Figure C.5: Simple fluid-flow relaxation time, at $T_{\text{ref}} = 25°\text{C}$, versus designed γ-valence in the heterotypic NSs studied in Chapter 5 (e.g., $\alpha_4\gamma_2$, $\alpha_3\gamma_3$, and $\alpha_2\gamma_4$). The concentration of heterotypic NS in each sample are all roughly between 420-470 μM. The solid blue line is a least squares linear fit to the data. We note that it is reasonable for the intercept at $t = 0$ to be between $1 < z \lesssim 2$. For instance, $z = 1.5$ corresponds to a situation where there are equal amounts of $z = 1$ and $z = 2$ NSs, meaning every valence-two NS can have its ends capped by a valence-one arm/hairpin. Such a situation would lead to chains likely four NS arms in length and, thus, not long enough to entangle. On the other hand, a solution of $z = 2$ NS is free to make chains of arms arbitrarily long and, thus, capable of entangling to make elastic networks. ***Inset:*** Simple fluid-flow relaxation time, at $T_{\text{ref}} = 25°\text{C}$, versus designed α-valence of the homotypic NSs measured in chapter 4. The concentration of the homotypic NSs here were all roughly 450-500 μM. The solid black line in is a least squares linear fit to the data.

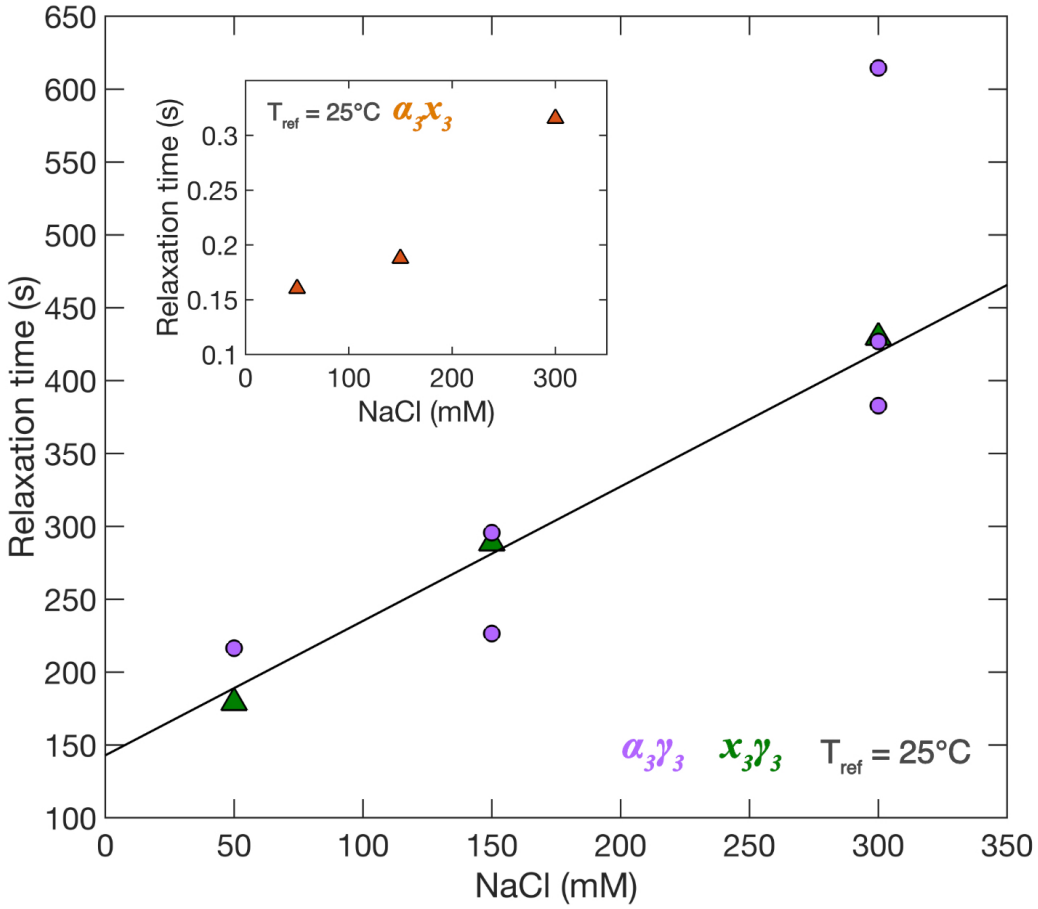

Figure C.6: Simple fluid-flow relaxation time, at $T_{\text{ref}} = 25°\text{C}$, versus added salt concentration (NaCl). The black line in the main plot is a weighted least squares linear fit to both $x_3\gamma_3$ and $\alpha_3\gamma_3$ data sets. The concentration of $x_3\gamma_3$ and $\alpha_3\gamma_3$ in the samples plotted are all roughly between 420-470 μM. *Inset* Simple fluid-flow relaxation time, at $T_{\text{ref}} = 25°\text{C}$, versus added salt for the $\alpha_3 x_3$ solution, which did not have enough data to warrant a linear fit.

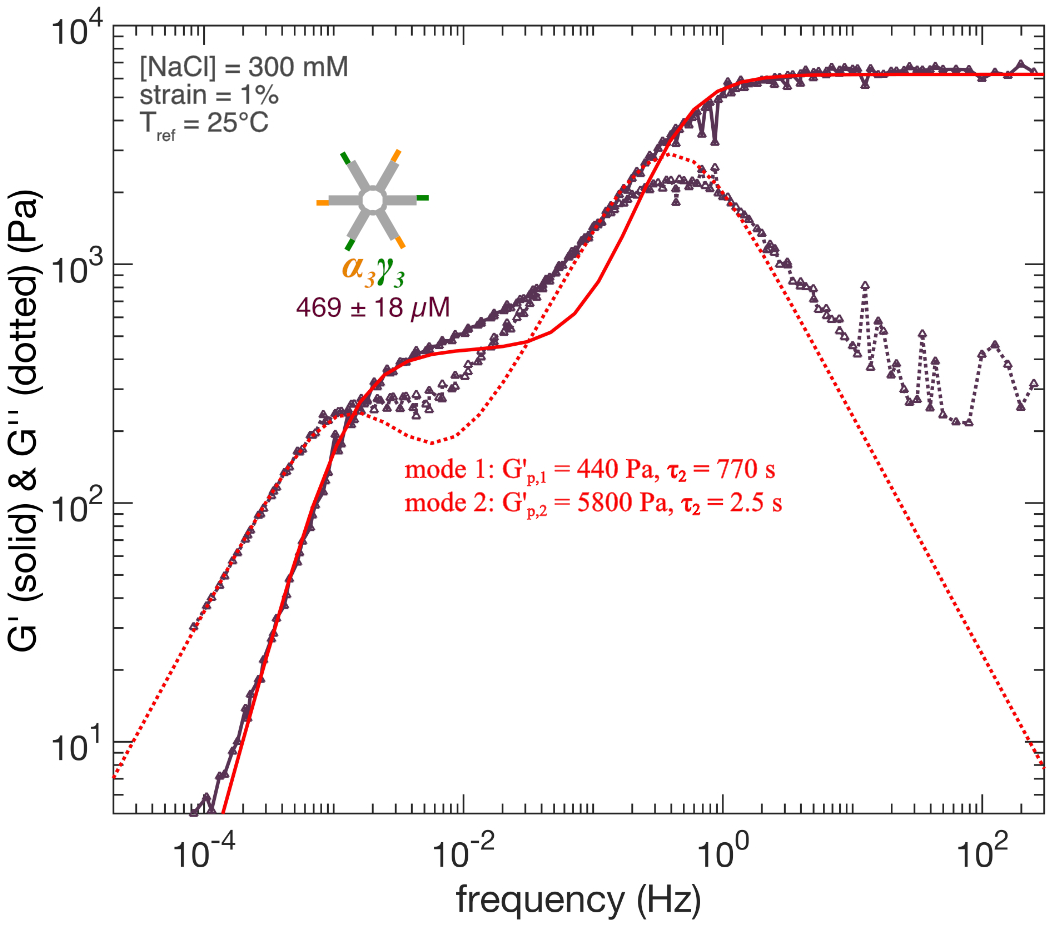

Figure C.7: Plot of G' and G'' versus frequency for an $\alpha_3\gamma_3$ NS at $T_{ref} = 25°$C. The red curve is a two-mode Maxwell viscoelastic spectra with manually chosen parameters, shown in the legend of the plot. The functional form for G' and G'' of a two-mode Maxwell spectra is shown in equation C.1 and C.2, respectively. The relaxation time parameters used are based off $\tau_{liq}(\alpha_3\gamma_3)$ and $\tau_c(\alpha_6)$. The storage modulus parameters used are roughly equal to $G'_p(\gamma_3)$ and $G'_p(\alpha_6)$.

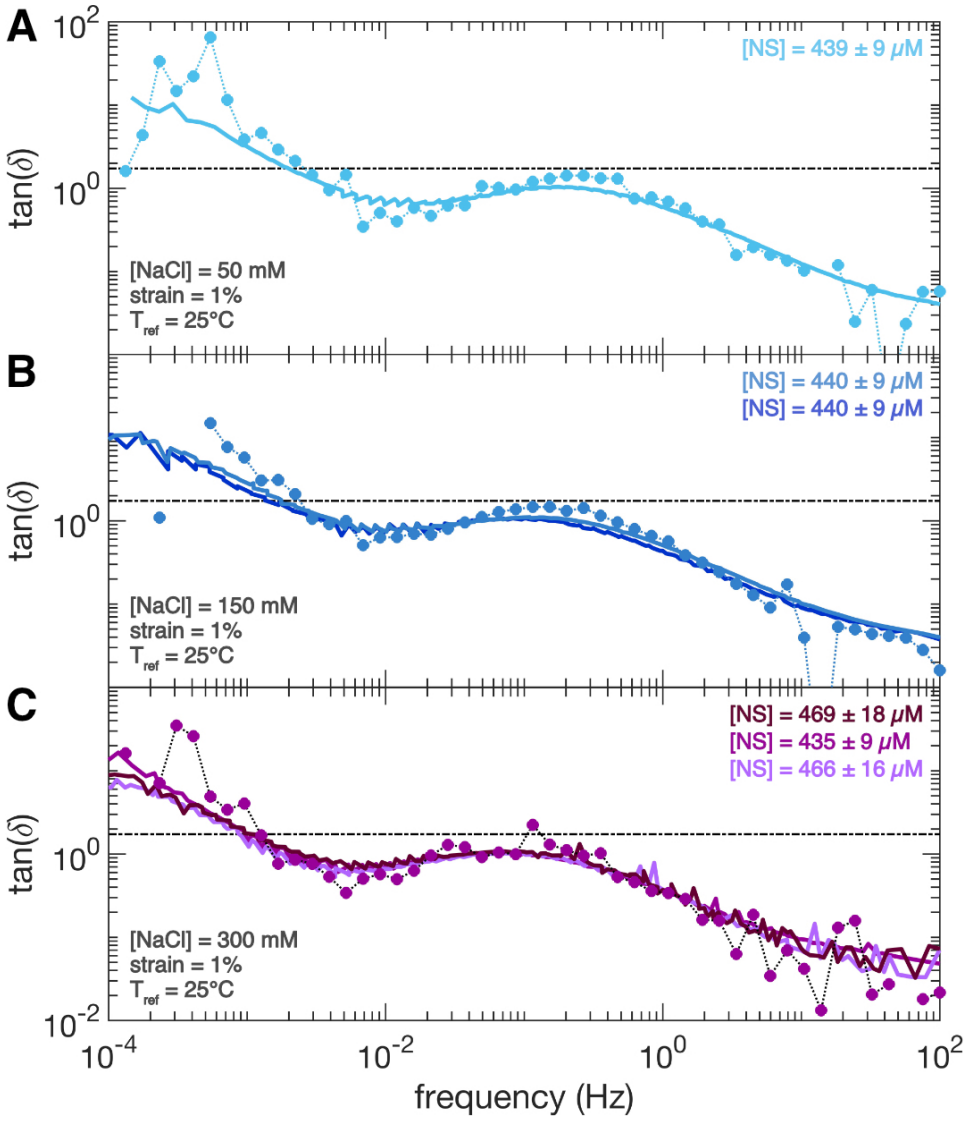

Figure C.8: Plots of $\tan(\delta)$ vs frequency for $\alpha_3\gamma_3$ NS solutions at an added salt of (**A**) 50 mM, (**B**) 150 mM, and (**C**) 300 mM NaCl. The solid lines denote raw data. The circles are the generalized Kramers-Kronig approximation for $\tan(\delta) \approx \tan((\pi/2)d\ln(G^*)/d\ln(f))$, where $(G^*)^2 = (G')^2 + (G'')^2$. G^* was calculated using the raw G' and G'' data and fit using a linear interpolation. The linear interpolation of G^* was then used to numerically calculate the derivative $d\ln(G^*)/d\ln(f)$.

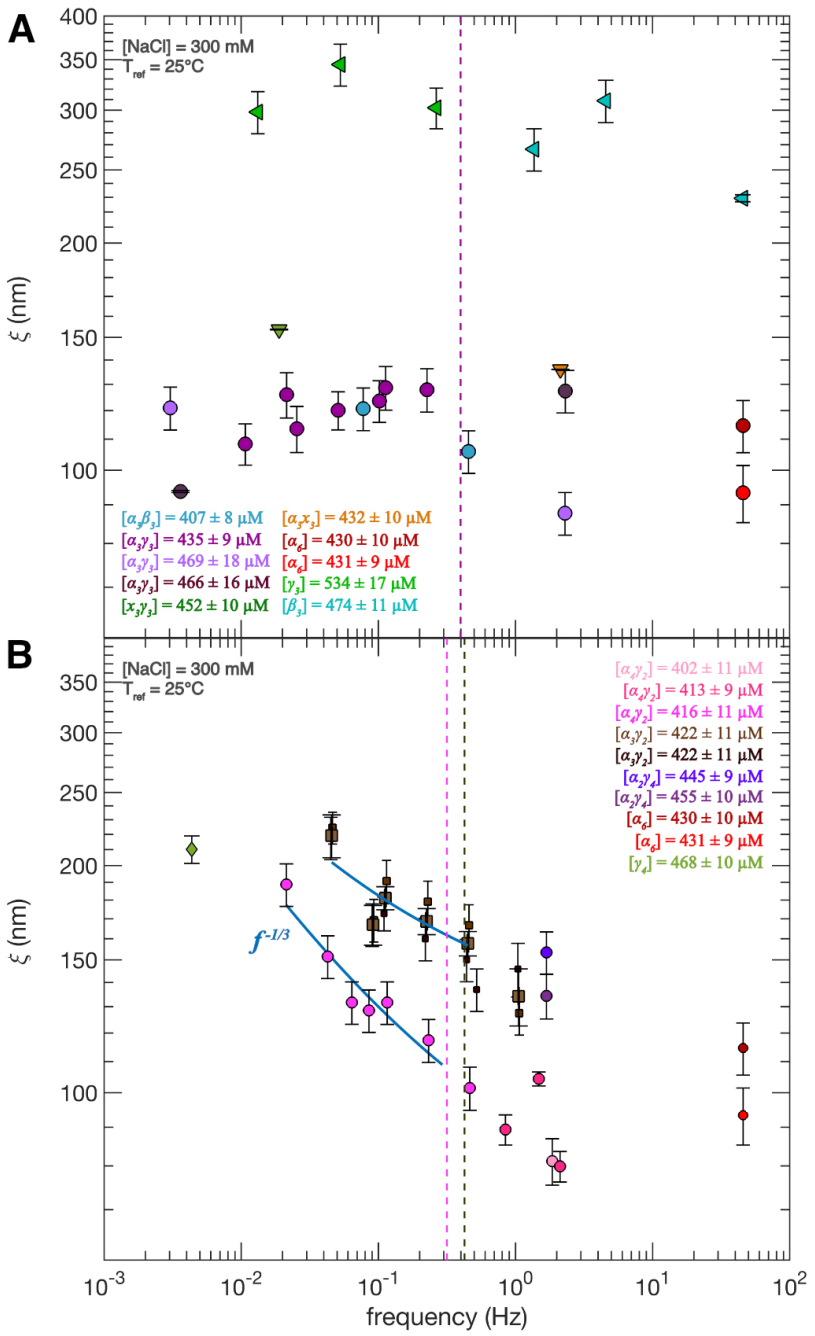

Figure C.9: Plots of ξ vs frequency for (**A**) β_3, γ_3, $\alpha_3 x_3$, $x_3\gamma_3$, $\alpha_3\beta_3$, and $\alpha_3\gamma_3$ (**B**) γ_4, $\alpha_3\gamma_2$, $\alpha_4\gamma_2$, and $\alpha_2\gamma_4$ at a reference temperature of $T_{ref} = 25°C$. Measurements of ξ vs frequency for α_6 are in both plots. The concentrations of NSs and added salt are listed in the legends of the plots. The dashed lines in both panels mark the high frequency crossover in $\alpha_3\gamma_3$, $\alpha_4\gamma_2$, and $\alpha_3\gamma_2$ NSs, respectively The solid line and large squares in **B** denotes a fit to the respective data set and an average of both $\alpha_3\gamma_2$ data sets, respectively.

Bibliography

[1] Michael Rubinstein and Ralph Colby. *Polymer Physics*. Oxford University Press, Oxford, 2007.

[2] Emanuella Zaccarelli. Colloidal gels: equilibrium and non-equilibrium routes. *J. Phys. Cond. Mat.*, 19(32):323101, 2007.

[3] Jake Song, Niels Holten-Andersen, and Gareth H. McKinley. Non-maxwellian viscoelastic stress relaxations in soft matter. *arXiv*, 2022.

[4] A.R. Bausch and K. Kroy. A bottom-up approach to cell mechanics. *Nature Physics*, 2:231–238, 2006.

[5] Federico Fanalista, Anthony Birnie, Renu Maan, Federica Burla, Kevin Charles, Grzegorz Pawlik, Siddharth Deshpande, Gijsje H. Koenderink, Marileen Dogterom, and Cees Dekker. Shape and size control of artificial cells for bottom-up biology. *ACS Nano*, 13(5):5439–5450, 2019.

[6] Rebeka Fijan, Michele Basile, Sonja Šostar Turk, Ema Žagar, Majda Žigon, and Romano Lapasin. A study of rheological and molecular weight properties of recycled polysaccharides used as thickeners in textile printing. *Carbohydrate Polymers*, 76(1):8–16, 2009.

[7] Muxian Shen, Li Li, Yimin Sun, Jun Xu, Xuhong Guo, and Robert K. Prud'homme. Rheology and adhesion of poly(acrylic acid)/laponite nanocomposite hydrogels as biocompatible adhesives. *Langmuir*, 30(6):1636–1642, 2014.

[8] Zachary M. Sherman, Kihoon Kim, Jiho Kang, Benjamin J. Roman, Hannah S. N. Crory, Diana L. Conrad, Stephanie A. Valenzuela, Emily Lin, Manuel N. Dominguez, Stephen L. Gibbs, Eric V. Anslyn, Delia J. Milliron, and Thomas M. Truskett. Plasmonic response of complex nanoparticle assemblies. *Nano Letters*, 23(7):3030–3037, 2023.

[9] Thomas M. FitzSimons, Felicia Oentoro, Tej V. Shanbhag, Eric V. Anslyn, and Adrianne M. Rosales. Preferential control of forward reaction kinetics in hydrogels crosslinked with reversible conjugate additions. *Macromolecules*, 53(10):3738–3746, 2020.

[10] Joshua Bush, Chih-Hsiang Hu, and Remi Veneziano. Mechanical properties of dna hydrogels: Towards highly programmable biomaterials. *Applied Sciences*, 11(4), 2021.

[11] Enrico Lattuada, Manuela Leo, Debora Caprara, Luisa Salvatori, Sciortino Francesco Stoppacciaro, Antonella, and Patrizia Filetici. Dna-gel, novel nanomaterial for biomedical applications and delivery of bioactive molecules. *Applied Sciences*, 11(4), 2020.

[12] Hydrogels in drug delivery: Progress and challenges. *Polymer*, 49(8):1993–2007, 2008.

[13] Silvia Biffi, Roberto Cerbino, Francesca Bomboi, Elvezia Maria Paraboschi, Rosanna Asselta, Francesco Sciortino, and Tommaso Bellini. Phase behavior and critical activated dynamics of limited-valence dna nanostars. *PNAS*, 110(38):15633–15637, 2013.

[14] Emanuela Bianchi, Julio Largo, Piero Tartaglia, Emanuella Zaccarelli, and Francesco Sciortino. Phase diagram of patchy colloids: Towards empty liquids. *Phys Rev Lett*, 97(168301):1–4, 2006.

[15] J. Clerk Maxwell. On the calculation of the equilibrium and stiffness of frames. *The London, Edinburgh, and Dublin Phil. Magazine & J. Sci.*, 27(182):294–299, 1864.

[16] Chase P Broedersz, Xiaoming Mao, Tom C Lubensky, and Frederick C MacKintosh. Criticality and isostaticity in fibre networks. *Nature Physics*, 7(12):983–988, December 2011.

[17] M. G. Yucht, M. Sheinman, and C. P. Broedersz. Dynamical behavior of disordered spring networks. *Soft Matter*, 9:7000–7006, 2013.

[18] Shravan Pradeep and Lilian C. Hsiao. Contact criterion for suspensions of smooth and rough colloids. *Soft Matter*, 16:4980–4989, 2020.

[19] Marlous Kamp, Bart de Nijs, Marjolein N. van der Linden, Isja de Feijter, Merel J. Lefferts, Antonio Aloi, Jack Griffiths, Jeremy J. Baumberg, Ilja K. Voets, and Alfons van Blaaderen. Multivalent patchy colloids for quantitative 3d self-assembly studies. *Langmuir*, 36(9):2403–2418, 2020.

[20] Michael P. Howard, Zachary M. Sherman, Adithya N Sreenivasan, Stephanie A. Valenzuela, Eric V. Anslyn, Delia J. Milliron, and Thomas M. Truskett. Effects of linker flexibility on phase behavior and structure of linked colloidal gels. *The Journal of Chemical Physics*, 154(7), 2021.

[21] Mingjiang Zhong, Rui Wang, Ken Kawamoto, Bradley D. Olsen, and Jeremiah A. Johnson. Quantifying the impact of molecular defects on polymer network elasticity. *Science*, 353(6305):1264–1268, 2016.

[22] Hiroto Ozaki and Tsuyoshi Koga. Network formation and mechanical properties of telechelic associating polymers with fixed junction multiplicity. *Macromol. Theory and Sims.*, 26(2):1600076, 2017.

[23] Paulina J Skrzeszewska, Frits A de Wolf, Marc WT Werten, Antoine PHA Moers, Martien A Cohen Stuart, and Jasper van der Gucht. Physical gels of telechelic triblock copolymers with precisely defined junction multiplicity. *Soft Matter*, 5(10):2057–2062, 2009.

[24] Fumihiko Tanaka and Katsuyoshi Nishinari. Junction multiplicity in thermoreversible gelation. *Macromol.*, 29(10):3625–3628, 1996.

[25] Chase P. Broedersz, Martin Depken, Norman Y. Yao, Martin R. Pollak, David A. Weitz, and Frederick C. MacKintosh. Cross-link-governed dynamics of biopolymer networks. *Phys. Rev. Lett.*, 105:238101, 2010.

[26] Shankar Lalitha Sridhar and Franck J. Vernerey. The chain distribution tensor: Linking nonlinear rheology and chain anisotropy in transient polymers. *Polymers*, 10(8), 2018.

[27] Nathaniel Conrad, Tynan Kennedy, Deborah K. Fygenson, and Omar A. Saleh. Increasing valence pushes dna nanostar networks to the isostatic point. *PNAS*, 116(15):7238–7243, 2019.

[28] Francesco Sciortino and Emanuela Zaccarelli. Equilibrium gels of limited valence colloids. *Current Opinion in Colloid Interface Science*, 30:90–96, 2017.

[29] Enrico Lattuada, Debora Caprara, Roberto Piazza, and Francesco Sciortino. Spatially uniform dynamics in equilibrium colloidal gels. *Science Advances*, 7(49), 2021.

[30] Byoung-jin Jeon, Dan T Nguyen, Gabrielle R Abraham, Nathaniel Conrad, Deborah K Fygenson, and Omar A Saleh. Salt-dependent properties of a coacervate-like, self-assembled dna liquid. *Soft Matter*, 14:7009–7015, 2018.

[31] Javier Fernandez-Castanon, Silvio Bianchi, Filippo Saglimbeni, Roberto Di Leonardo, and Francesco Sciortino. Microrheology of dna hydrogel gelling and melting on cooling. *Soft Matter*, 14:6431–6438, 2018.

[32] Giovanni Nava, Marina Rossi, Silvia Biffi, Francesco Sciortino, and Tommaso Bellini. Fluctuating elasticity mode in transient molecular networks. *Phys. Rev. Lett.*, 119:078002, 2017.

[33] Francesca Bomboi, Silvia Biffi, Roberto Cerbino, Thomaso Bellini, Federico Bordi, and Francesco Sciortino. Equilibrium gels of trivalent dna-nanostars: Effect of the ionic strength on the dynamics. *The European physical journal E. Soft Matter*, 38(6), 2015.

[34] Silvia Biffi, Roberto Cerbino, Giovanni Nava, Francesca Bomboi, Francesco Sciortino, and Tommaso Bellini. Equilibrium gels of low-valence dna nanostars: a colloidal model for strong glass former. *Soft Matter*, 11:3132–3138, 2015.

[35] Giovanni Nava, Marina Rossi, Silvia Biffi, Francesco Sciortino, and Tommaso Bellini. Fluctuating elasticity mode in transient molecular networks. *Phys. Rev. Lett.*, 119(7):078002–7, 2017.

[36] Emanuele Locatelli and Lorenzo Rovigatti. An accurate estimate of the free energy and phase diagram of all-dna bulk fluids. *Polymers*, 10(4):447;1–16, 2018.

[37] Taehyun Lee, Sungho Do, Jae Gyung Lee, Do-Nyun Kim, and Yongdae Shin. The flexibility-based modulation of dna nanostar phase separation. *Nanoscale*, 13(41):17638–17647, 2021.

[38] H. R. Kruyt and H. G. Bungenberg de Jong. Zur kenntnis der lyophilen kolloide. *Kolloidchemische Beihefte*, 28(1):1–54, 1928.

[39] Russell J. Stewart, James C. Weaver, Daniel E. Morse, and J. Herbert Waite. The tube cement of phragmatopoma californica: a solid foam. *Journal of Experimental Biology*, 207(26):4727–4734, 2004.

[40] J. Herbert Waite, Niels Holten Andersen, Scott Jewhurst, and Chengjun Sun. Mussel adhesion: Finding the tricks worth mimicking. *The Journal of Adhesion*, 81(3-4):297–317, 2005.

[41] Clifford P Brangwynne, Timothy J Mitchison, and Anthony A Hyman. Active liquid-like behavior of nucleoli determines their size and shape in xenopus laevis oocytes. *PNAS*, 108(11):4334–4339, 2010.

[42] Dan Bracha, Mackenzie T Walls, Ming-Tzo Wei, Lian Zhu, Martin Kurian, José Avalos, Jared E Toettcher, and Clifford P Brangwynne. Mapping local and global liquid phase behavior in living cells using photo-oligomerizable seeds. *Cell*, 175:1467–1480, 2018.

[43] Karsten Rippe. Liquid–liquid phase separation in chromatin. *Cold Spring Harbor Perspectives in Biology*, 2021.

[44] Je-Kyung Ryu, Da-Eun Hwang, and Jeong-Mo Choi. Current understanding of molecular phase separation in chromosomes. *International Journal of Molecular Sciences*, 22:10736, 2021.

[45] Rajeev A Jain. The manufacturing techniques of various drug loaded biodegradable poly(lactide-co-glycolide) (plga) devices. *Biomaterials*, 21(23):2475–2490, 2000.

[46] Christian Luebbert, Fabian Huxoll, and Gabriele Sadowski. Amorphous-amorphous phase separation in api/polymer formulations. *Molecules*, 22(296):1–17, 2017.

[47] Christian Luebbert, Edmont Stoyanov, and Gabriele Sadowski. Phase behavior of asds based on hydroxypropyl cellulose. *International Journal of Pharmaceutics: X*, 3:100070, 2021.

[48] Divya Eratte, Bo Wang, Kim Dowling, Colin J Barrow, and Benu P Adhikari. Complex coacervation with whey protein isolate and gum arabic for the microencapsulation of omega-3 rich tuna oil. *Food & Function*, 5:2743–2750, 2014.

[49] Zuobing Xiao, Wanlong Liu, Guangyong Zhu, Rujun Zhou, and Yunwei Niu. A review of the preparation and application of flavour and essential oils microcapsules based on complex coacervation technology. *Journal of the Science of Food and Agriculture*, 94:1482–1494, 2014.

[50] Simon Alberti, Amy Gladfelter, and Tanja Mittag. Considerations and challenges in studying liquid-liquid phase separation and biomolecular condensates. *Cell*, 176:419–434, 2019.

[51] Yimin Luo, Mengyang Gu, Chelsea ER Edwards, Megan T Valentine, and Matthew E Helgeson. High-throughput microscopy to determine morphology, microrheology, and phase boundaries applied to phase separating coacervates. *Soft Matter*, 18:3063–3075, 2022.

[52] Katie A Black, Dimitrios Priftis, Sarah L Perry, Jeremy Yip, William Y Byun, and Matthew Tirrell. Protein encapsulation via polypeptide complex coacervation. *ACS Macro Letters*, 3:1088–1091, 2014.

[53] Siddharth Deshpande and Cees Dekker. Studying phase separation in confinement. *Current Opinion in Colloid & Interface Science*, 52:101419, 2021.

[54] A. Hensley, W. M. Jacobs, and W. B. Rogers. Self-assembly of photonic crystals by controlling the nucleation and growth of dna-coated colloids. *Proc Natl Acad Sci U S A*, 119(1), 2022.

[55] Alessia Villois, Umberto Capasso Palmiero, Prerit Mathur, Gaia Perone, Timo Schneider, Lunna Li, Matteo Salvalaglio, Andrew deMello, Stavros Stavrakis, and Paolo Arosio. Droplet microfluidics for the label-free extraction of complete phase diagrams and kinetics of liquid–liquid phase separation in finite volumes. *Small*, 18(46):2202606, 2022.

[56] David C Johnston. *Advances in Thermodynamics of the van der Waals Fluid*. 2053-2571. Morgan & Claypool Publishers, 2014.

[57] Lorenzo Rovigatti, Frank Smallenburg, Flavio Romano, and Francesco Sciortino. Gels of dna nanostars never crystallize. *ACS Nano*, 8(4):3567–3574, 2014.

[58] Emanuele Locatelli, Philip H Handle, Christos N Likos, Francesco Sciortino, and Lorenzo Rovigatti. Condensation and demixing in solutions of dna nanostars and their mixtures. *ACS Nano*, 11:2094–2102, 2017.

[59] John SantaLucia and Donald Hicks. The thermodynamics of dna structural motifs. *Annual Review of Biophysics and Biomolecular Structure*, 33(1):415–440, 2004.

[60] Lorenzo Di Michele, Bortolo M Mognetti, Taiki Yanagishima, Patrick Varilly, Zachary Ruff, Daan Frenkel, and Erika Eiser. Effect of inert tails on the thermodynamics of dna hybridization. *Journal of the American Chemical Society*, 136(18):6538–6541, 2014.

[61] Lorenzo Rovigatti, Francesca Bomboi, and Francesco Sciortino. Accurate phase diagram of tetravalent dna nanostars. *The Journal Of Chemical Physics*, 140:154903, 2014.

[62] M.S. Wertheim. Fluids with highly directional attractive forces. i. statistical thermodynamics. *Journal of Statistical Physics*, 35:19–34, 1984.

[63] M.S. Wertheim. Fluids with highly directional attractive forces. ii. thermodynamic perturbation theory and intergral equations. *Journal of Statistical Physics*, 35:35–47, 1984.

[64] M.S. Wertheim. Fluids with highly directional attractive forces. iii. multiple attraction sites. *Journal of Statistical Physics*, 42:459–476, 1986.

[65] Walter G. Chapman, George Jackson, and Keith E. Gubbins. Phase equilibria of associating fluids. *Molecular Physics*, 65(5):1057–1079, 1988.

[66] Walter G Chapman, Keith E Gubbins, George Jackson, and Maciej Radosz. New reference equation of state for associating liquids. *Industrial & Engineering Chemistry Research*, 29(8):1709–1721, 1990.

[67] W. Zmpitas and J. Gross. Detailed pedagogical review and analysis of wertheim's thermodynamic perturbation theory. *Fluid Phase Equilibria*, 428:121–152, 2016.

[68] Simon Alberti, Shambaditya Saha, Jeffrey B. Woodruff, Titus M. Franzmann, Jie Wang, and Anthony A. Hyman. A user's guide for phase separation assays with purified proteins. *Journal of Molecular Biology*, 430(23):4806–4820, 2018.

[69] Saehyun Choi, McCauley O. Meyer, Philip C. Bevilacqua, and Christine D. Keating. Phase-specific rna accumulation and duplex thermodynamics in multiphase coacervate models for membraneless organelles. *Nature Chemistry*, 14(10):1110–1117, 2022.

[70] Yuri Hong, Khoi Phuong Dao, Taehyun Kim, Sumin Lee, Yongdae Shin, YongKeun Park, and Dong Soo Hwang. Label-free quantitative analysis of coacervates via 3d phase imaging. *Advanced Optical Materials*, 9(20):2100697, 2021.

[71] V. C. Coffman and J. Q. Wu. Counting protein molecules using quantitative fluorescence microscopy. *Trends Biochem Sci*, 37(11):499–506, 2012.

[72] Tadija Kekic and Jory Lietard. Sequence-dependence of cy3 and cy5 dyes in 3' terminally-labeled single-stranded dna. *Scientific Reports*, 12(1):14803, 2022.

[73] Patrick M. McCall, Kyoohyun Kim, Anatol W. Fritsch, J.M. Iglesias-Artola, L.M. Jawerth, Jie Wang, M. Ruer, J. Peychl, Andrey Poznyakovskiy, Jochen Guck, Simon Alberti, Anthony A. Hyman, and Jan Brugués. Quantitative phase microscopy enables precise and efficient determination of biomolecular condensate composition. *bioRxiv*, page 2020.10.25.352823, 2020.

[74] David R. Jacobson and Omar A. Saleh. Counting the ions surrounding nucleic acids. *Nucleic Acids Research*, 45(4):1596–1605, 2016.

[75] Enas M Ahmed. Hydrogel: Preparation, characterization, and applications: A review. *Journal of advanced research*, 6(2):105–121, 2015.

[76] Takuya Katashima, Ryota Kudo, Mitsuru Naito, Satoru Nagatoishi, Kanjiro Miyata, Ung-il Chung, Kouhei Tsumoto, and Takamasa Sakai. Experimental comparison of bond lifetime and viscoelastic relaxation in transient networks with well-controlled structures. *ACS Macro Letters*, 11(6):753–759, 2022.

[77] Xiaoming Mao. Mechanics of disordered fiber networks. In Ferenc Horkay, Jack F. Douglas, and Emanuela Del Gado, editors, *Gels and Other Soft Amorphous Solids*, chapter 10, pages 199–210. American Chemical Society, 2018.

[78] Nadrian C. Seeman. Nucleic acid junctions and lattices. *J. Theor. Biol.*, 99(2):237–247, 1982.

[79] Yougen Li, Yolanda D. Tseng, Sang Y. Kwon, Leo D'Espaux, J. Scott Bunch, Paul L. McEuen, and Dan Luo. Controlled assembly of dendrimer-like dna. *Nature Material*, 3(1):38–42, 2004.

[80] Jong Bum Lee, Songmin Peng, Dayong Yang, Young Hoon Roh, Hisakage Funabashi, Nokyoung Park, Edward J. Rice, Liwei Chen, Rong Long, Mingming Wu, and Dan Luo. A mechanical metamaterial made from a dna hydrogel. *Nat. Nanotech.*, 7(12):816–820, 2012.

[81] Lorenzo Rovigatti, Frank Smallenburg, Flavio Romano, and Francesco Sciortino. Gels of dna nanostars never crystallize. *ACS Nano*, 8(4):3567–3574, 2014.

[82] Francesco Sciortino and Emanuella Zaccarelli. Equilibrium gels of limited valence colloids. *Current Opinion in Colloid and Interface Science*, 30:90–96, 2017.

[83] Dan T. Ngyuen and Omar A. Saleh. Tuning phase and aging of dna hydrogels through molecular design. *Soft Matter*, Advance Article, 2017.

[84] Joseph N. Zadeh, Conrad D. Steenberg, Justin S. Bois, Brian R. Wolfe, Marshall B. Pierce, Asif R. Khan, Robert M. Dirks, and Niles A. Pierce. Nupack: analysis and design of nucleic acid systems. *Journal of Computational Chemistry*, 32(1):170–173, 2011.

[85] D. Zeb Rocklin, Lilian Hsiao, Megan Szakasits, Michael J. Solomon, and Xiaoming Mao. Elasticity of colloidal gels: structural heterogeneity, floppy modes, and rigidity. *Soft Matter*, 17:6929–6934, 2021.

[86] Brian P. Tighe. Relaxations and rheology near jamming. *Phys. Rev. Lett.*, 107:158303, 2011.

[87] Matthieu Pouzot, Taco Nicolai, Lazhar Benyahia, and Dominique Durand. Strain hardening and fracture of heat-set fractal globular protein gels. *J. Coll. Sci.*, 293(2):376–383, 2006.

[88] T. Gisler, R. C. Ball, and D. A. Weitz. Strain hardening of fractal colloidal gels. *Phys Rev Lett*, 82(5):1064–1067, 1999.

[89] Michelle E. Seitz, David Martina, Tristan Baumberger, Venkat R. Krishnan, Chung-Yuen Hui, and Kenneth R. Shull. Fracture and large strain behavior of self-assembled triblock copolymer gels. *Soft Matter*, 5(2):447–456, 2008.

[90] Kendra A. Erk, Kevin J. Henderson, and Kenneth R. Shull. Strain stiffening in sythentic and biopolymer networks. *Biomacromol.*, 11(5):1358–1363, 2010.

[91] Jack F. Douglas. Elasticity of networks with permanent and thermoreversible cross-links. *MRS Online Proceedings Library (OPL)*, 1234:1234–QQ04–01, 2009.

[92] M.F. Thorpe. Continuous deformations in random networks. *J. Non-cryst. Sol.*, 57(3):355–370, 1983.

[93] Jingchen Feng, Herbert Levine, Xiaoming Mao, and Leonard M. Sander. Alignment and nonlinear elasticity in biopolymer gels. *Phys. Rev. E*, 91(4):042710, 2015.

[94] P. R. Onck, T. Koeman, T. van Dillen, and E. van der Giessen. Alternative explanation of stiffening in cross-linked semiflexible networks. *Phys Rev Lett*, 95(17):178102, 2005.

[95] Leyou Zhang, D. Zeb Rocklin, Leonard M. Sander, and Xiaoming Mao. Fiber networks below the isostatic point: Fracture without stress concentration. *Phys. Rev. Mat*, 1(5):052602, 2017.

[96] E. M. Huisman and T. C. Lubensky. Internal stresses, normal modes, and nonaffinity in three-dimensional biopolymer networks. *Phys. Rev. Lett.*, 106:088301, Feb 2011.

[97] M. Dennison and H. Stark. Viscoelastic properties of marginal networks in a solvent. *Phys. Rev. E*, 93:022605, 2016.

[98] Leyou Zhang and Xiaoming Mao. Finite-temperature mechanical instability in disordered lattices. *Phys. Rev. E*, 93:022110, Feb 2016.

[99] M. Van den Tempel. Mechanical properties of plastic-disperse systems at very small deformations. *J. Coll. Sci.*, 16(3):284–296, 1961.

[100] M. Van den Tempel. Rheology of concentrated suspensions. *J. Coll. Sci.*, 71(1):18–20, 1978.

[101] L. G. B. Bremer and T. van Vliet. The modulus of particle networks with stretched strands. *Rheologica Acta*, 30(1):98–101, 1991.

[102] M. Mellema, J. H. J. van Opheusden, and T. van Vliet. Categorization of rheological scaling models for particle gels applied to casein gels. *Journal of Rheology*, 46(1):11–29, 2002.

[103] R. de Rooij, D. van den Ende, M. H. G. Duits, and J. Mellema. Elasticity of weakly aggregating polystyrene latex dispersions. *Phys. Rev. E*, 49(4):3038–3049, 1994.

[104] Dominik Ho, Julia L. Zimmermann, Florian A. Dehmelt, Uta Steinbach, Matthias Erdmann, Philip Severin, Katja Falter, and Hermann E. Gaub. Force-driven separation of short double-stranded dna. *Biophysical Journal*, 97(12):3158–3167, 2009.

[105] Emanuella Zaccarelli, I. Saika-Voivod, S. V. Buldyrev, A. J. Moreno, P. Tartaglia, and Francesco Sciortino. Gel to glass transition in simulation of a valence-limited colloidal system. *Journal of Chemical Physics*, 124(124908):1–14, 2006.

[106] Wei-Heng Shih, Wan Y. Shih, Seong-Il Kim, Jun Liu, and Ilhan A. Aksay. Scaling behavior of the elastic properties of colloidal gels. *Phys. Rev. A*, 42(8):4772–4779, 1990.

[107] J. P. Clerk, G. Giraud, J. M. Laugier, and J. M. Luck. The electrical conductivity of binary disordered systems, percolation clusters, fractals and related models. *Adv. Phys.*, 39(3):191–309, 1990.

[108] Liang Guo, Ralph H. Colby, Charles P. Lusignan, and Andrew M. Howe. Physical gelation of gelatin studied with rheo-optics. *Macromol.*, 36(26):10009–10020, 2003.

[109] Madeleine Djabourov, Jacques Leblond, and Pierre Papon. Gelation of aqueous gelatin solutions. ii. rheology of the sol-gel transition. *Journal de Physique*, 49(2):333–343, 1988.

[110] M. Adam, M. Delsanti, D. Durand, G. Hild, and J.P. Munch. Mechanical properties near gelation threshold, comparison with classical and 3d percolation theories. *Pure & App. Chem*, 53:1489–1494, 1981.

[111] M. Daoud. Viscoelasticity near the sol-gel transition. *Macromol.*, 33(8):3019–3022, 2000.

[112] M. Muthukumar. Dynamics of polymeric fractals. *The Journal of Chemical Physics*, 83(6):3161–3168, 1985.

[113] Francois Chambon and H. Henning Winter. Linear viscoelasticity at the gel point of a crosslinking pdms with imbalanced stoichiometry. *Journal of Rheology*, 31(8):683–697, 1987.

[114] Aaron P. R. Eberle, Ramón Castañeda-Priego, Jung M. Kim, and Norman J. Wagner. Dynamical arrest, percolation, gelation, and glass formation in model nanoparticle dispersions with thermoreversible adhesive interactions. *Langmuir*, 28(3):1866–1878, 2012.

[115] A. Zaccone, H. H. Winter, M. Siebenbürger, and M. Ballauff. Linking self-assembly, rheology, and gel transition in attractive colloids. *Journal of Rheology*, 58(5):1219–1244, 2014.

[116] Noémie Dagès, Louis V. Bouthier, Lauren Matthews, Sébastien Manneville, Thibaut Divoux, Arnaud Poulesquen, and Thomas Gibaud. Interpenetration of fractal clusters drives elasticity in colloidal gels formed upon flow cessation. *Soft Matter*, 18:6645–6659, 2022.

[117] A. Einstein. Über die von der molekularkinetischen theorie der wärme geforderte bewegung von in ruhenden flüssigkeiten suspendierten teilchen. *Annalen der Physik*, 322(8):549–560, 1905.

[118] D. J. Jacobs and M. F. Thorpe. Generic rigidity percolation in two dimensions. *Phys. Rev. E*, 53:3682–3693, 1996.

[119] Peter Sollich, Fran çois Lequeux, Pascal Hébraud, and Michael E. Cates. Rheology of soft glassy materials. *Phys. Rev. Lett.*, 78:2020–2023, 1997.

[120] Peter Sollich. Rheological constitutive equation for a model of soft glassy materials. *Phys. Rev. E*, 58:738–759, 1998.

[121] Prince E. Rouse. A theory of the linear viscoelastic properties of dilute solutions of coiling polymers. *The Journal of Chemical Physics*, 21(7):1272–1280, 1953.

[122] H. C. Booij and G. P. J. M. Thoone. Generalization of kramers-kronig transforms and some approximations of relations between viscoelastic quantities. *Rheologica Acta*, 21(1):15–24, Jan 1982.

[123] Michael Rubinstein, Eugene Helfand, and Dale S Pearson. Theory of polydispersity effects of polymer rheology: binary distribution of molecular weights. *Macromolecules*, 20(4):822–829, 1987.

[124] Michael Rubinstein and Ralph H. Colby. Self-consistent theory of polydisperse entangled polymers: Linear viscoelasticity of binary blends. *The Journal of Chemical Physics*, 89(8):5291–5306, 1988.

[125] Jacques Roovers. Linear viscoelastic properties of polybutadiene. a comparison with molecular theories. *Polymer Journal*, 18(2):153–162, Feb 1986.

[126] R. R. Rahalkar. Linear viscoelastic behavior of narrow molecular weight distribution 1,4 polybutadiene: Comparison with doi-edwards theory of reptation. *Rheologica Acta*, 29(1):88–97, Jan 1990.

[127] Masao Doi and S. F. Edwards. Dynamics of concentrated polymer systems. part 1.—brownian motion in the equilibrium state. *J. Chem. Soc., Faraday Trans. 2*, 74:1789–1801, 1978.

[128] M. Dennison, M. Sheinman, C. Storm, and F. C. MacKintosh. Fluctuation-stabilized marginal networks and anomalous entropic elasticity. *Phys. Rev. Lett.*, 111:095503, 2013.

[129] Andrea Pelissetto and Ettore Vicari. Critical phenomena and renormalization-group theory. *Physics Reports*, 368(6):549–727, 2002.

[130] Omkar Hegde, Tianhao Li, Anjali Sharma, Marco Borja, William M. Jacobs, and W. Benjamin Rogers. Competition between self-assembly and phase separation induces re-entrant condensation of dna liquids. *arXiv*, 2023.

[131] Andrew G. Pyo, Yaojun Zhang, and Ned S. Wingreen. Proximity to criticality determines surface tension of biomolecular condensates. *Work not yet published*, 2023.

[132] Jan Ilavsky, Pete R. Jemian, Andrew J. Allen, Fan Zhang, Lyle E. Levine, and Gabrielle G. Long. Ultra-small-angle X-ray scattering at the Advanced Photon Source. *Journal of Applied Crystallography*, 42(3):469–479, 2009.

[133] Victor A. Bloomfield, Donald M. Crothers, and Ignacio Tinoco Jr. *Nucleic Acids: Structures, Properties, and Functions*. University Science Books, 2000.

[134] D. R. Jacobson, D. B. McIntosh, M. J. Stevens, M. Rubinstein, and O. A. Saleh. Single-stranded nucleic acid elasticity arises from internal electrostatic tension. *Proc Natl Acad Sci U S A*, 114(20):5095–5100, 2017.

[135] Qingjia Chi, Guixue Wang, and Jiahuan Jiang. The persistence length and length per base of single-stranded dna obtained from fluorescence correlation spectroscopy measurements using mean field theory. *Physica A: Statistical Mechanics and its Applications*, 392(5):1072–1079, 2013.

[136] Jiho Kang, Zachary M. Sherman, Hannah S. N. Crory, Diana L. Conrad, Marina W. Berry, Benjamin J. Roman, Eric V. Anslyn, Thomas M. Truskett, and Delia J. Milliron. Modular mixing in plasmonic metal oxide nanocrystal gels with thermoreversible links. *The Journal of Chemical Physics*, 158(2):024903, 2023.

[137] Anouk S. Lubbe, Qing Liu, Sanne J. Smith, Jan Willem de Vries, Jos C. M. Kistemaker, Alex H. de Vries, Ignacio Faustino, Zhuojun Meng, Wiktor Szymanski, Andreas Herrmann, and Ben L. Feringa. Photoswitching of dna hybridization using a molecular motor. *Journal of the American Chemical Society*, 140(15):5069–5076, 2018.

[138] Gabrielle R.C. Abraham. *DNA Nanostars: A Model System to Investigate Biomolecular Condensation*. PhD thesis, University of California, Santa Barbara, 2023.

[139] Miki Yoshimura, Tomohisa Takaya, and Katsuyoshi Nishinari. Rheological studies on mixtures of corn starch and konjac-glucomannan. *Carbohydrate Polymers*, 35(1):71–79, 1998.

[140] Ben Fabry, Geoffrey N. Maksym, James P. Butler, Michael Glogauer, Daniel Navajas, and Jeffrey J. Fredberg. Scaling the microrheology of living cells. *Phys. Rev. Lett.*, 87:148102, 2001.

[141] Darryl R. Overby, Benjamin D. Matthews, Eben Alsberg, and Donald E. Ingber. Novel dynamic rheological behavior of individual focal adhesions measured within single cells using electromagnetic pulling cytometry. *Acta Biomaterialia*, 1(3):295–303, 2005.

[142] Qian Huang, Olga Mednova, Henrik K. Rasmussen, Nicolas J. Alvarez, Anne L. Skov, Kristoffer Almdal, and Ole Hassager. Concentrated polymer solutions are different from melts: Role of entanglement molecular weight. *Macromolecules*, 46(12):5026–5035, 2013.

[143] Kun-You Chung, Kathleen N. Halwachs, Pengtao Lu, Kaihong Sun, Hope A. Silva, Adrianne M. Rosales, and Zachariah A. Page. Rapid hydrogel formation via tandem visible light photouncaging and bioorthogonal ligation. *Cell Reports Physical Science*, 3(12):101185, 2022.

[144] Gisela Cabré, Aida Garrido-Charles, Miquel Moreno, Miquel Bosch, Montserrat Porta-de-la Riva, Michael Krieg, Marta Gascón-Moya, Núria Camarero, Ricard Gelabert, José M. Lluch, Félix Busqué, Jordi Hernando, Pau Gorostiza, and Ramon Alibés. Rationally designed azobenzene photoswitches for efficient two-photon neuronal excitation. *Nature Communications*, 10(1):907, Feb 2019.

[145] Hiroyuki Asanuma, Takanori Ito, Takayuki Yoshida, Xingguo Liang, and Makoto Komiyama. Photoregulation of the formation and dissociation of a dna duplex by using the cis–trans isomerization of azobenzene. *Angewandte Chemie International Edition*, 38(16):2393–2395, 1999.

[146] M. J. Cavaluzzi and P. N. Borer. Revised uv extinction coefficients for nucleoside-5'-monophosphates and unpaired dna and rna. *Nucleic Acids Res*, 32(1):e13, 2004.

[147] Lubert Stryer. *Biochemistry*. W.H. Freeman & Company, New York, 4th edition, 1998.

[148] Johannes Schindelin, Ignacio Arganda-Carreras, Erwin Frise, Verena Kaynig, Mark Longair, Tobias Pietzsch, Stephan Preibisch, Curtis Rueden, Stephan Saalfeld, Benjamin Schmid, Jean-Yves Tinevez, Daniel James White, Volker Hartenstein, Kevin Eliceiri, Pavel Tomancak, and Albert Cardona. Fiji: an open-source platform for biological-image analysis. *Nature Methods*, 9(7):676–682, July 2012.

[149] Alison O. Nwokeoji, Peter M. Kilby, David E. Portwood, and Mark J. Dickman. Accurate quantification of nucleic acids using hypochromicity measurements in conjunction with uv spectrophotometry. *Analytical Chemistry*, 89(13567):13567–13574, 2017.

[150] N. R. Markham and M. Zuker. Dinamelt web server for nucleic acid melting prediction. *Nucleic Acids Research*, 33(Web Server Issue):W577–W581, 2005.

[151] Nicholas R. Markham and Michael Zuker. *UNAFold In: Keith, J.M. (eds) Bioinformatics. Methods in Molecular Biology*, pages 3–31. Humana Press, Totowa, NJ, 2008.

[152] Wenwei Liu, Yuliang Jin, Sheng Chen, Hernan A. Maksec, and Shuiqing Li. Equation of state for random sphere packings with arbitrary adhesion and friction. *Soft Matter*, 13(421):421–427, 2018.

[153] Robert M. Ziff and Salvatore Torquato. Percolation of disordered jammed sphere packings. *J. Phys. A Math & Gen.*, 50(8):1–12, 2017.